

DEVELOPMENT OF CaZrO<sub>3</sub>-BASED HYDROGEN SENSORS WITH OXIDE  
REFERENCE ELECTRODES FOR MOLTEN ALUMINUM

Except where reference is made to the work of others, the work described in this dissertation is my own or was done in collaboration with my advisory committee. This dissertation does not include proprietary or classified information.

---

Vivek Krishnan

Certificate of Approval:

---

Ruel A. (Tony) Overfelt  
Professor  
Materials Engineering

---

Jeffrey W. Fergus, Chair  
Associate Professor  
Materials Engineering

---

ZhongYang (Z.-Y.) Cheng  
Assistant Professor  
Materials Engineering

---

Thomas E. Albrecht-Schmitt  
Associate Professor  
Chemistry

---

Joe F. Pittman  
Interim Dean  
Graduate School

DEVELOPMENT OF  $\text{CaZrO}_3$ -BASED HYDROGEN SENSORS WITH OXIDE  
REFERENCE ELECTRODES FOR MOLTEN ALUMINUM

Vivek Krishnan

A Dissertation

Submitted to

the Graduate Faculty of

Auburn University

in Partial Fulfillment of the

Requirements for the

Degree of

Doctor of Philosophy

Auburn, Alabama  
December 15, 2006

DEVELOPMENT OF  $\text{CaZrO}_3$ -BASED HYDROGEN SENSORS WITH OXIDE  
REFERENCE ELECTRODES FOR MOLTEN ALUMINUM

Vivek Krishnan

Permission is granted to Auburn University to make copies of this dissertation at its discretion, upon the request of individuals or institutions and at their expense.  
The author reserves all publication rights.

---

Signature of Author

---

Date of Graduation

## VITA

Vivek Krishnan, son of Mr. R.S. Krishnan and Mrs. Rajivi Krishnan, was born on September 20, 1978 in the city of Jamshedpur, India. He joined Annamalai University, India in August 1996 and graduated with a Bachelor of Engineering in Chemical Technology in May 2000. He joined the graduate program in Materials Engineering at Auburn University in January, 2001. Vivek is a student member of ACerS and MRS. He is also a member of the Materials Engineering honors society Alpha Sigma Mu (Alabama Beta chapter).

DISSERTATION ABSTRACT

DEVELOPMENT OF  $\text{CaZrO}_3$ -BASED HYDROGEN SENSORS WITH OXIDE  
REFERENCE ELECTRODES FOR MOLTEN ALUMINUM

Vivek Krishnan

Doctor of Philosophy, December 15, 2006  
(B.E., Annamalai University, India, 2000)

166 Typed Pages

Directed by Jeffrey W. Fergus

Hydrogen is a major cause of gas porosity in aluminum and is frequently removed from the melt prior to casting. The degassing process can be better controlled if the hydrogen content in the melt is known. Thus, gas sensors which can make continuous *in situ* measurements in molten aluminum are needed. Current online hydrogen sensing systems are complex designs which are prohibitively expensive. Solid electrolyte based potentiometric sensors have been developed as an attractive alternate. These sensors have traditionally used a gas phase as the reference electrode. The present design has a condensed-phase reference electrode to avoid the need for transport of the reference gas into and out of the melt. The use of an oxide rather than a hydride phase reference is expected to considerably lower device cost and improve shelf life and reliability.

The sensor element consists of a solid electrolyte tube based on 10 mol% In-doped  $\text{CaZrO}_3$ , which was synthesized using both solid oxide and oxalate co-precipitation

techniques. Precursor oxalate powders prepared using polymeric surfactants (PEG) were characterized using SEM, XRD, FTIR and particle size analysis. PEG was found to reduce particle size and also influence the process of perovskite formation. The oxalate co-precipitation technique enabled powder synthesis at reduced processing time and temperature.

Closed-one-end tubes were slip cast and densified for use as solid electrolytes. Impedance spectroscopy and D.C. resistance measurements were made at temperatures between 650 and 900°C. Undoped  $\text{CaZrO}_3$  was found to be a p-type conductor in air. In-doped  $\text{CaZrO}_3$  acted as a proton conductor in air and argon+ $\text{H}_2\text{O}$ , whereas the material was found to be a p-type conductor in pure argon. While bulk conduction was found to be homogenous with activation energies matching those from D.C. measurements, conduction across the grain boundary was found to be heterogeneous.

Potentiometric sensors using In-doped  $\text{CaZrO}_3$  as the electrolyte, and metal/metal oxides, metal/metal hydrides as the reference electrodes were fabricated. Sensors with Mg-MgO reference electrodes, on exposure to argon and aluminum environments, generated a potential matching the Nernstian voltage. Sensors with Ca- $\text{CaH}_2$  reference electrodes measured the Nernstian potential when exposed to 5% $\text{H}_2$ . Laboratory tests conducted using gas mixtures also showed sensors with Mg-MgO reference electrodes to measure changes in hydrogen concentration. Pilot plant testing of sensor prototypes was carried out in commercial aluminum alloy melts and the sensors were found to respond to hydrogen degassing. The response of these sensors to changes in the gas content of the melt correlated reasonably well with that of a commercially available system for measuring hydrogen content in molten aluminum (AlScan™).

## ACKNOWLEDGEMENTS

I would like to thank my advisor, Dr. Jeff Fergus, for his guidance and encouragement during the course of my research studies. His constant support and motivation has been instrumental in helping me accomplish my objectives.

This research project would not have been possible without continuous support from Dr. Tony Overfelt and the NASA Solidification Design Consortium. Special thanks go out to Dr. S. Bakhthiyarov, Amit Suryavanshi and Jonathon Capps for their help with aluminum casting. I also appreciate Dr. Festus Fasoyinu and all the engineers from CANMET who helped us arrange the testing of our devices at CANMET, Ottawa.

During my work here, I had the opportunity of learning skills from several people. I would like to acknowledge George Teodorescu, Zhimin Li and Rui Shao for their time and assistance. I would also like to thank my colleagues, Devendra Tambe, Mihai Irimia-Vladu, Naren Pari, Lisa Orona, Victoria Salazar, Chris Long and Todd Dorough for their help. Working with you guys has been a pleasure.

My friends have been an important source of encouragement. Although I am not able to name them all here, I would like to mention Kashyap, Raghu, Anand, Karthik, Shankar, Kavita, Ranjani and Gayatri for their support.

Finally, I would like to dedicate this work to my parents, Mr. R. S. Krishnan and Mrs. Rajivi Krishnan, and my great sister Divya.

Style Manual or journal used: Journal of the American Ceramics Society

Computer software used: Microsoft Office, ZView, Data Thief



## TABLE OF CONTENTS

LIST OF TABLES .....	xii
LIST OF FIGURES.....	xiii
1. INTRODUCTION .....	1
1.1. Motivation for research .....	1
1.2. Solid electrolyte properties .....	2
1.3. Hydrogen sensor development .....	2
2. LITERATURE REVIEW .....	4
2.1 Porosity in aluminum castings .....	4
2.1.1 Introduction .....	4
2.1.2 Hydrogen porosity in aluminum castings .....	5
2.1.3 Effect of porosity on properties .....	8
2.1.4 Hydrogen removal from liquid aluminum .....	8
2.1.5 Hydrogen determination in aluminum melts .....	11
2.2 Electrochemical sensors based on solid oxide conductors .....	18
2.2.1 Introduction .....	18
2.2.2 Use of solid electrolytes in sensors .....	20
2.2.3 Sensor classification .....	21
2.2.4 Application of electrochemical sensors in molten metal processing .....	23

2.2.5 Oxygen sensors for steel .....	24
2.3. Properties of calcium zirconate .....	26
2.3.1 Structure, properties and applications .....	26
2.3.2 CaZrO <sub>3</sub> based solid electrolyte materials .....	30
2.3.3 Proton conduction in In-doped CaZrO <sub>3</sub> .....	31
2.4 Ceramic Synthesis and Processing .....	35
2.4.1. Solid oxide synthesis .....	35
2.4.2. Wet chemical synthesis .....	36
3. OBJECTIVES .....	38
4. EXPERIMENTAL METHODS .....	39
4.1. Ceramic preparation .....	39
4.2. Powder characterization and processing .....	42
4.3. Electrical measurements .....	44
4.4. Sensor fabrication and testing .....	46
5. RESULTS AND DISCUSSION .....	52
5.1 Synthesis, processing and characterization of doped and undoped calcium zirconate .....	52
5.1.1 Solid oxide synthesis .....	52
5.1.2 Oxalate coprecipitation synthesis .....	55
5.1.2.1 Precursor synthesis and characterization .....	55
5.1.2.2 Oxalate decomposition .....	59
5.2 Electrical characterization of the solid electrolyte material .....	75
5.2.1 Solid electrolyte characterization using impedance spectroscopy .....	75

5.2.2 Conductivity of undoped CaZrO <sub>3</sub> in air .....	81
5.2.3 Conductivity of In-doped CaZrO <sub>3</sub> in air .....	85
5.2.4 Conductivity of In-doped CaZrO <sub>3</sub> in dry argon .....	91
5.2.5 Conductivity of In-doped CaZrO <sub>3</sub> in Ar+H <sub>2</sub> O .....	95
5.2.6 Electrical properties of Mg-doped CaZrO <sub>3</sub> .....	95
5.2.7 Alternate equivalent circuit model .....	98
5.2.8 Electrical characterization of In-doped CaZrO <sub>3</sub> at very low oxygen partial pressures .....	100
5.3 Sensor fabrication and testing .....	104
5.3.1. Sensor design and measurements in argon .....	104
5.3.2 Reference electrode performance in aluminum .....	108
5.3.3. Hydrogen sensing using hydride based reference electrodes .....	111
5.3.4 Hydrogen sensing using oxide based reference electrodes .....	113
5.3.5 Sensor tests in pilot plant conditions .....	115
6. CONCLUSIONS .....	120
6.1. Ca(Zr,In)O <sub>3</sub> powder synthesis .....	120
6.2. Electrical characterization of Ca(Zr,In)O <sub>3</sub> materials .....	120
6.3. Hydrogen sensor testing .....	121
7. FUTURE WORK .....	122
REFERENCES .....	128

## LIST OF TABLES

Table 1 Proton-dopant binding energies computed for In, Ga and Sc in $\text{CaZrO}_3$ .....	33
Table 2 Solutions A, B and C used in the co-precipitation synthesis of $\text{Ca}(\text{Zr},\text{In})\text{O}_3$ .....	40
Table 3 Two layer brick layer model along with values of circuit parameters extracted from relaxations observed at $870^\circ\text{C}$ .....	79
Table 4 List of activation energies reported for stoichiometric and non-stoichiometric $\text{CaZrO}_3$ according to mode of measurement and temperature range .....	85
Table 5 List of gas specifications obtained for AR 300 from Airgas .....	105
Table 6 Sensor and AlScan outputs observed in 4 different Al alloy melts at CANMET .....	117

## LIST OF FIGURES

Figure 1 Variation of hydrogen solubility with melt temperature. <sup>16</sup> .....	6
Figure 2 Stages involved in the formation of hydrogen porosity in aluminum castings. ...	7
Figure 3 Fine dispersed gas bubbles produced by rotary unit for degassing molten aluminum. <sup>24</sup> .....	10
Figure 4 Steps involved in the reduced pressure test to estimate hydrogen content.....	12
Figure 5 Standard photographic reference chart used to compare RPT samples showing estimates of porosity and sample density. ....	12
Figure 6 Schematic diagram of the Alscan probe. <sup>26</sup> .....	13
Figure 7 Schematic of a hydrogen sensor for molten aluminum. <sup>37</sup> .....	17
Figure 8 Schematic of typical designs for oxygen sensors for molten steel. <sup>55,51,56</sup> .....	26
Figure 9 Phase Diagram of the CaO-ZrO <sub>2</sub> binary system. ....	27
Figure 10 Phase diagram describing the decomposition of phases $\phi_1$ and $\phi_2$ .....	28
Figure 11 Schematic showing the ABO <sub>3</sub> type cubic perovskite structure of BaZrO <sub>3</sub> .....	29
Figure 12 Structural comparison showing distorted ZrO <sub>6</sub> octahedra in orthorhombic perovskites. <sup>63</sup> .....	30
Figure 13 Schematic detailing steps involved in the transport of hydrogen through the CaZrO <sub>3</sub> lattice. <sup>99</sup> .....	32
Figure 14 Proton-dopant interaction in CaZrO <sub>3</sub> based materials. <sup>100</sup> .....	33

Figure 15 Flowcharts of the solid oxide (left) and co-precipitation synthesis (right) processes used to synthesize the solid electrolyte material $\text{Ca}(\text{Zr},\text{In})\text{O}_3$ .....	41
Figure 16 Process steps involved in the forming of fresh electrolyte tubes using slip casting.....	44
Figure 17 Schematic of cell design used to measure impedance at very low oxygen pressures. Very low oxygen partial pressures are fixed on opposite sides of the electrolyte by using molten aluminum. ....	46
Figure 18 Schematic of the $\text{Ca}(\text{Zr},\text{In})\text{O}_3$ based potentiometric sensor designed to detect hydrogen in molten aluminum. Metal-metal oxide and metal-metal hydride mixtures used as condensed phase reference electrodes. ....	48
Figure 19 Picture of a sensor prototype constructed for pilot plant testing .....	49
Figure 20 AU sensor and AlScan making simultaneous measurements in a commercial alloy melt at CANMET, Ottawa CA. ....	50
Figure 21 Commercial rotary degasser used to reduce hydrogen content in the melt between sensor measurements. ....	51
Figure 22 XRD pattern from a pure sample of $\text{CaCO}_3$ used in the solid oxide synthesis .....	53
Figure 23 XRD pattern from a pure sample of $\text{In}_2\text{O}_3$ used in the solid oxide synthesis ...	53
Figure 24 XRD pattern from pure $\text{ZrO}_2$ used in the solid oxide synthesis .....	54
Figure 25 XRD pattern from $\text{CaZr}_{0.9}\text{In}_{0.1}\text{O}_{2.95}$ synthesized using the solid state route.....	54
Figure 26 XRD pattern typical of precursor powders obtained from co-precipitation process with and without using washing as process step.....	56

Figure 27 FTIR spectra obtained from precursor powders prepared with and without using the washing step.....	59
Figure 28 Phases formed during perovskite formation from precursor decomposition....	61
Figure 29 Disappearance of In-rich secondary phase $\text{CaIn}_2\text{O}_4$ at high temperatures .....	61
Figure 30 Disappearance of the In-rich peak in $\text{CaZr}_{0.9}\text{In}_{0.1}\text{O}_{2.95}$ shown by a decrease in peak ratios .....	62
Figure 31 Formation of In-rich $\text{CaIn}_2\text{O}_4$ phase due to increased indium content in the perovskite powder. ....	63
Figure 32 Increase in peak ratios of integrated intensities in $\text{CaZrO}_3$ powders with varying In contents. ....	64
Figure 33 Variation of cell volume (V) with increasing indium concentration in $\text{CaZrO}_3$ . ....	65
Figure 34 Mg-doped $\text{CaZrO}_3$ powders obtained from oxalate precursor decomposition. ....	66
Figure 35 Schematic of surfactant PEG preventing particle agglomeration by limiting particle-particle interactions.....	68
Figure 36 SEM image of precursor particles synthesized using PEG as a surfactant.....	69
Figure 37 SEM image of precursor particles synthesized without use of PEG. ....	69
Figure 38 Effect of PEG addition on particle size distribution of precursor powders.....	70
Figure 39 Effect of precipitate washing on particle size distribution of precursor powders. ....	70
Figure 40 Influence of PEG on particle settling. Powders prepared using PEG settled down slower than those prepared without PEG indicating smaller sizes.....	72
Figure 41 Effect of PEG addition on perovskite formation from precursor powders.....	72

Figure 42 Effect of ball-milling on perovskite formation from precursor powders. prepared without PEG.....	73
Figure 43 Effect of ball-milling on perovskite formation from precursor powders prepared using PEG.....	74
Figure 44 Pellet surface with porous Pt electrodes at 1000x.....	76
Figure 45 Highly networked Pt electrode on CaZrO <sub>3</sub> pellet at 3500x.....	77
Figure 46 Nyquist plot of impedance measured from CaZr <sub>0.9</sub> In <sub>0.1</sub> O <sub>3-α</sub> pellet at 870°C. ..	78
Figure 47 Bode plot showing dependence of impedance magnitude on frequency.....	78
Figure 48 Bode representation showing variation of phase lag (θ) with frequency. ....	79
Figure 49 Schematic showing a polycrystalline pellet across which A.C and D.C resistance is measured.....	80
Figure 50 Electrical conductivity of undoped CaZrO <sub>3</sub> measured in air.....	82
Figure 51 Arrhenius plot of conductivity for samples of CaZrO <sub>3</sub> measured in air. ....	84
Figure 52 Bulk conductivities observed for Ca(Zr,In)O <sub>3</sub> and CaZrO <sub>3</sub> samples in air .....	87
Figure 53 Variation of resistance with temperature in CaZr <sub>0.95</sub> In <sub>0.05</sub> O <sub>2.975</sub> measured in air.....	89
Figure 54 Variation of time constants with temperature for CaZr <sub>0.95</sub> In <sub>0.05</sub> O <sub>3-α</sub> measured in air. ....	89
Figure 55 Variation of capacitances in In-doped CaZrO <sub>3</sub> measured in air.....	90
Figure 56 Variation of exponent n with temperature in In-doped CaZrO <sub>3</sub> . ....	91
Figure 57 Bulk and grain boundary conductivity of In-doped CaZrO <sub>3</sub> in argon. ....	93
Figure 58 Variation of bulk capacitance in In-doped CaZrO <sub>3</sub> with temperature in argon.....	93



Figure 59 Arrhenius plot of hole mobilities in In-doped CaZrO <sub>3</sub> .	94
Figure 60 Activation energy for the creation of holes in In-doped CaZrO <sub>3</sub> .	94
Figure 61 DC conductivity measured for CaZr <sub>0.9</sub> In <sub>0.1</sub> O <sub>3-x/2</sub> exposed to Ar+H <sub>2</sub> O.	96
Figure 62 DC conductivity measured for CaZr <sub>0.9</sub> In <sub>0.1</sub> O <sub>3-x/2</sub> exposed to Ar+H <sub>2</sub> O.	96
Figure 63 Total conductivities measured for CaZr <sub>1-x</sub> Mg <sub>x</sub> O <sub>3-x</sub> pellets. Results compared with undoped and In-doped CaZrO <sub>3</sub> .	97
Figure 64 Admittance representation of impedance data measured from CaZr <sub>0.9</sub> In <sub>0.1</sub> O <sub>3-α</sub> pellet at 870°C.	99
Figure 65 Circuit parameters extracted from impedance data at 870°C using the reduced CPE model.	100
Figure 66 Conduction domain diagram developed by Kurita et al. <sup>162</sup> to describe the defect properties of CaZr <sub>0.9</sub> In <sub>0.1</sub> O <sub>3-x/2</sub> materials.	101
Figure 67 Domain diagram highlighting the oxygen and hydrogen partial pressures in molten aluminum at 750°C.	101
Figure 68 Typical impedance spectrum measured in liquid aluminum at 1000K.	102
Figure 69 Typical impedance spectrum measured from a Ca(Zr,In)O <sub>3</sub> tube inserted in solid aluminum.	103
Figure 70 Voltage between argon and Mg-MgO measured using CaZr <sub>0.9</sub> In <sub>0.1</sub> O <sub>2.75</sub> as the solid electrolyte.	104
Figure 71 Comparison of voltage response at 720°C from tubular and pellet shaped electrolyte samples tested in Ar with Mg/MgO reference electrode. Cell construction used a porous support tube.	107

Figure 72 Schematic of cell configurations used to test sensors with Mg-MgO reference electrodes in argon.....	109
Figure 73 Theoretical voltage difference between Mg/MgO and Al/Al <sub>2</sub> O <sub>3</sub> reference electrodes calculated from thermochemical tables.....	109
Figure 74 Difference in voltage output measured between sensors containing Mg/MgO and Al/Al <sub>2</sub> O <sub>3</sub> reference electrodes dipped in liquid aluminum. ....	110
Figure 75 Voltage output from tubular sensor (Mg/MgO reference electrode) suspended in aluminum.....	111
Figure 76 Voltage measured from a sensor using Ca-CaH <sub>2</sub> reference electrode tested in Ar+5%H <sub>2</sub> environment. ....	112
Figure 77 EMF measured from a Ca(Zr,In)O <sub>3</sub> based sensor with Mg-Mgo reference electrode exposed to Ar and Ar+5%H <sub>2</sub> . Sensor shows a change in response with hydrogen content that is both stable and reproducible.....	114
Figure 78 Simultaneous measurements made by sensor and AlScan in Aluminum 356 melt at CANMET.....	116
Figure 79 Cross-section of reduced pressure test samples taken before and after degassing showing change in porosity.....	116
Figure 80 Comparison of voltage change caused due to degassing calculated from AlScan measurements and sensor outputs from 4 the different alloy melts. ...	118
Figure 81 A simple block diagram for a feedback control system that can be designed to optimize hydrogen content in molten aluminum. ....	123

Figure 82 Equilibrium oxygen partial pressures established by using metal-metal  
oxide mixtures and  $H_2O-H_2$ ,  $CO-CO_2$  gas mixtures as a function of  
temperature..... 124

## 1. INTRODUCTION

### 1.1. Motivation for research

Today's industrialized world places more and more emphasis on automatic control and real-time monitoring of all industrial processes. Aluminum degassing is one such industrial process which involves removal of dissolved hydrogen from the melt prior to casting. Since hydrogen removal is an important step in aluminum processing, there is a need to optimize the degassing process with a simple online detection system that can continuously monitor hydrogen levels in the melt. In-situ hydrogen detection in molten metal could lead to the development of feedback-controlled degassing systems which would substantially improve process efficiency and produce superior aluminum parts.

Most commercial hydrogen detection techniques transport a reference gas into and out of the liquid melt. This requires expensive equipment and complex practices that may appear unattractive to the common foundry-man. Concentration cell type potentiometric sensors using solid electrolytes offer a potentially inexpensive, simple solution to this problem. Such sensors typically use a gas phase reference to fix the hydrogen partial pressure. The voltage measured across the electrolyte is related to the hydrogen concentration in the melt according to the Nernst equation.

Although the electrochemical technique offers a simpler solution it still does not necessarily avoid the requirement of transporting a gas mixture through molten metal. The use of a metal-metal hydride mixture helps overcome this problem by fixing a

reference hydrogen partial pressure which can be calculated from thermodynamics. These materials however, are not very stable and have been known to degrade over time, limiting their use in commercial devices. Oxide materials should have better high temperature stability, so, condensed phase reference electrodes based on metal-metal oxide mixtures could offer devices with a longer shelf life.

## 1.2. Solid electrolyte properties

Electrolytes for high temperature electrochemical applications are usually solid oxides. The solid electrolyte electrically separates the reference electrode from the melt by allowing the passage of ions from one side to the other side, while blocking electronic transport. As molten aluminum presents a very harsh and corrosive high temperature environment, the solid electrolyte material used should have good chemical and thermal stability. Adequate electrical properties are also desired as sensor operation depends on the conduction of ionic defects through the electrolyte. In addition, the solid electrolyte material should be easily processed.

## 1.3. Hydrogen sensor development

$\text{Ca}(\text{Zr},\text{In})\text{O}_3$  based materials possess several attractive properties and have become popular for electrochemical applications in molten metal. These materials are relatively inert in the melt, have excellent thermal shock resistance and can be synthesized using a wide variety of techniques. The ability to conduct protons in the presence of hydrogen/moisture makes them specifically attractive for hydrogen sensing applications.

The current project investigates development of CaZrO<sub>3</sub>-based hydrogen sensors for molten aluminum applications. Issues related to solid electrolyte synthesis and processing were studied through structural characterization and the material's electrical properties were analyzed through conductivity measurements. Sensor prototypes using oxide based reference electrodes were fabricated, and tested in both laboratory and pilot plant conditions.

## 2. LITERATURE REVIEW

### 2.1 Porosity in aluminum castings

#### 2.1.1 Introduction

Aluminum is the most abundant metal found in the earth's crust and is one of the most successfully used structural materials. The silvery white element was first seen and named by Sir Humphry Davy in 1808.<sup>1</sup> Today it is the second largest metal produced in the world after iron, with total production in 2005 reaching 23,500 metric tones.<sup>2</sup> Aluminum possesses several interesting properties like low density, high strength and good corrosion resistance making it suitable for a wide range of applications.<sup>3,4</sup> Common usages of the material include automotive applications,<sup>5</sup> beverage packaging,<sup>6</sup> construction,<sup>7,8</sup> power transmission,<sup>9</sup> consumer appliances etc.

A large volume of aluminum parts are produced by casting processes. Liquid aluminum is poured into a mold cavity and then cooled to form the desired part. Although aluminum can be produced by all common casting processes, there are various issues that require the constant attention of foundrymen. One of the major foundry concerns is melt quality.<sup>10</sup> Inclusions, dissolved gas, oxide particles easily contaminate the melt.<sup>11</sup> These cause defective castings with degraded properties and normally get rejected by the consumer.

Since more and more scrap is being reused everyday,<sup>12</sup> companies that recycle aluminum find it imperative to monitor quality of the melt in order to remain competitive. While impurities and oxides can generally be prevented from entering the melt by taking proper precautions, porosity-type defects could be more difficult to avoid. Monroe<sup>13</sup> describes porosity as the most common complaint of metal casters, as many improvements in the quality, performance and reliability can be achieved by its elimination.

Porosity in aluminum castings is generally attributed to the entrapment of gas bubbles in the melt or metal shrinkage during solidification.<sup>14</sup> Aluminum experiences volumetric changes when forming the solid phase from molten state. If the shrinkage due to metal solidification is not compensated by delivering fresh liquid metal, a void can be created.<sup>15</sup> Large voids of this kind are typically formed when liquid metal gets isolated within the solid during solidification.

### 2.1.2 Hydrogen porosity in aluminum castings

Pores are also formed in castings due to the entrapment of hydrogen bubbles. Hydrogen is the only gas with sufficient solubility in liquid aluminum.<sup>16</sup> It is typically introduced into the melt during the interaction between aluminum and moisture. Molten aluminum reacts with moisture from the surroundings to form aluminum oxide (dross) and hydrogen according to the reaction,





The atomic hydrogen formed, dissolves in the melt due to its high solubility in liquid aluminum. Once the hydrogen content in the melt exceeds a threshold limit, gas formation occurs according to the equilibrium,



Alloy additions like magnesium have high hydrogen solubility and could increase hydrogen content if added in large amounts. Remelting of metal and usage of wet tools and refractory linings also result in increased hydrogen uptake by the melt.

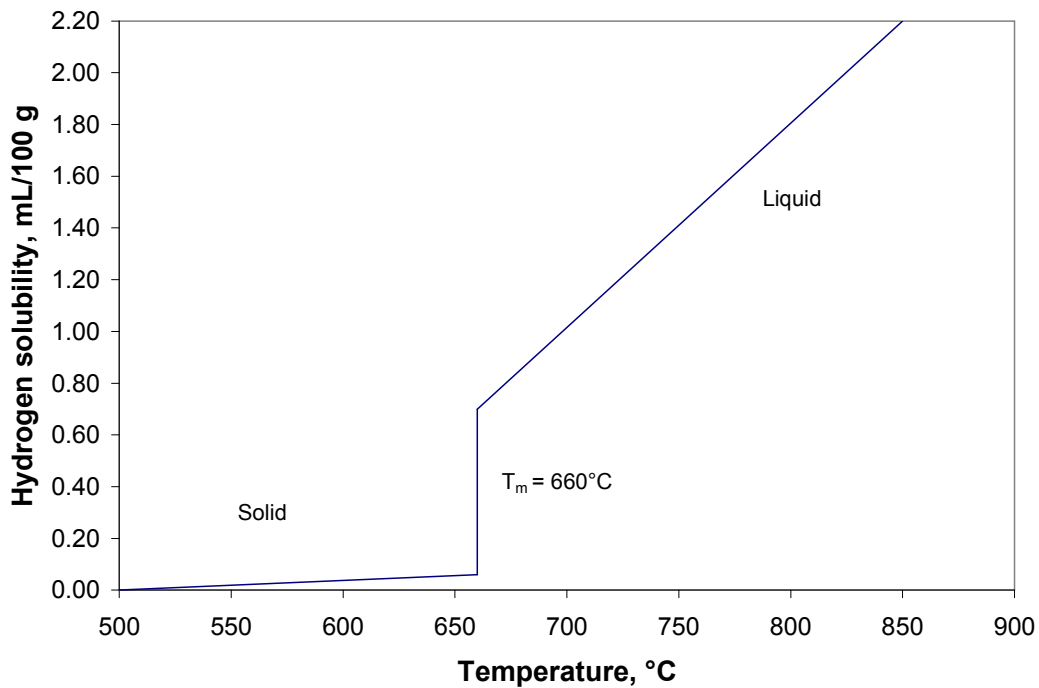


Figure 1 Variation of hydrogen solubility with melt temperature.<sup>16</sup>

Gas solubility in liquid metal is usually expressed in ml per 100 g of the metal, where 1 ml/100g = 0.9 ppm concentration by weight. The maximum solubility of

hydrogen in liquid aluminum is 0.67-0.77 ml/100 g of aluminum (660°C, 1 atm) while only 0.03 ml/100 g is soluble in solid aluminum. This corresponds to a 20-fold decrease in hydrogen solubility during solidification. The hydrogen solubility limit varies with temperature of the melt as shown in Figure 1.

Once molten metal is poured into the mold, it first solidifies along the mold walls. Reduced solubility leads to hydrogen being rejected at the solid-liquid interface thus increasing the gas content in the inter-dendritic liquid. Once the hydrogen content exceeds the solubility limit, pores are nucleated at dendrite roots and other heterogenous sites such as inclusions. The surface melt layer is exposed to cooler atmosphere and solidifies faster than the rest of the liquid. In the meantime hydrogen nuclei coalesce together and form bubbles. The solidifying metal traps the hydrogen bubbles present in the liquid pool, which leads to hydrogen porosity in the final casting. The basic steps of the above mentioned porosity forming mechanism are shown in Figure 2.

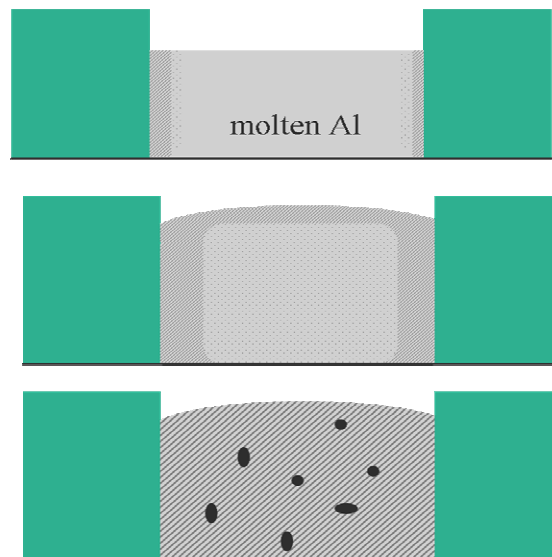


Figure 2 Stages involved in the formation of hydrogen porosity in aluminum castings.

### 2.1.3 Effect of porosity on properties

Most pores in aluminum castings are caused by a combination of shrinkage and hydrogen porosity. The defects cause several changes in the materials' properties. Pores can start fatigue cracks by acting as stress concentration sites and could lower fatigue resistance as well as strength.<sup>17</sup> Porous castings also experience a lack of pressure-tightness, reduced machinability and might require polishing of the surface defects prior to use.<sup>18</sup> Yield properties generally depend on the matrix material, and are thus less affected by porosity.

### 2.1.4 Hydrogen removal from liquid aluminum

As dissolved hydrogen is primarily responsible for porosity, it is desired to reduce the gas content in the melt. This is commonly achieved by the avoidance of hydrogen absorption and removing absorbed hydrogen prior to casting. Hydrogen removal basically involves diffusion of hydrogen from the melt to a carrier gas or vacuum. The efficiency of this process depends on alloy composition and temperature among other factors.

Common removal techniques used in many commercial foundries are natural outgassing, vacuum degassing and bubble degassing.

**Natural outgassing:** A decrease in temperature will reduce hydrogen solubility limit in the melt. Reducing the melt temperature can remove hydrogen if the hydrogen content exceeds the solubility limit at the lower temperature. So, hydrogen will then diffuse out of the melt to the environment with lower hydrogen content. This simple method has limited efficiency and is not always feasible.

**Vacuum degassing:** This technique involves the application of vacuum over the melt.<sup>19</sup> Since the hydrogen partial pressure in vacuum should be very low, hydrogen can be forced out of the melt. This method is more popular than the previous technique as high efficiencies have been reported. However, the expensive vacuum equipment makes it attractive only for high end applications where high melt purity is necessary.

**Bubble degassing:** In this process, a carrier gas is bubbled through the melt.<sup>20</sup> Hydrogen contained in the liquid metal diffuses into the gas bubbles due to a hydrogen partial pressure difference and gets transported out of the melt. Since gas bubbles are distributed throughout the melt, the process offers increased contact area and lowers the hydrogen diffusion distance.<sup>21</sup> These two factors result in higher process efficiency.

The important components of a bubble degassing equipment are the degassing agent and the setup used to flow gas into the melt. The system used to introduce the carrier gas into the melt must be able to produce small gas bubbles and distribute them uniformly. The degassing setup must not cause much disturbance to the melt surface, since loss of the protective layer might result in increased hydrogen absorption and inclusion formation.

The carrier agent should ideally have little or no hydrogen content. Interaction of the gas with melt additives is undesired, since this would alter melt composition thus affecting final properties of the cast product. Chlorine has been widely used as a degassing agent for aluminum melts. It is however, known to react with magnesium additives, and has been specifically used for “demagging” applications in aluminum.<sup>22</sup> On the hand, the ability to form volatile compounds with hydrogen could prove useful.

Chlorine reacts with hydrogen to form hydrogen chloride which exits the melt faster than other inert gases like argon.<sup>23</sup>

**Rotary degassing:** While tubes can be used to facilitate passage of the carrier gas through the melt, rotor units have been very successful in degassing systems.<sup>24</sup> Rotor units are allowed to rotate in the melt while releasing gas through its head. The gas immediately forms small, finely dispersed bubbles because of shear forces created in the melt due to rotor motion. Graphite is the material typically used for rotor construction. The process is highly efficient although maintenance costs are typically high.

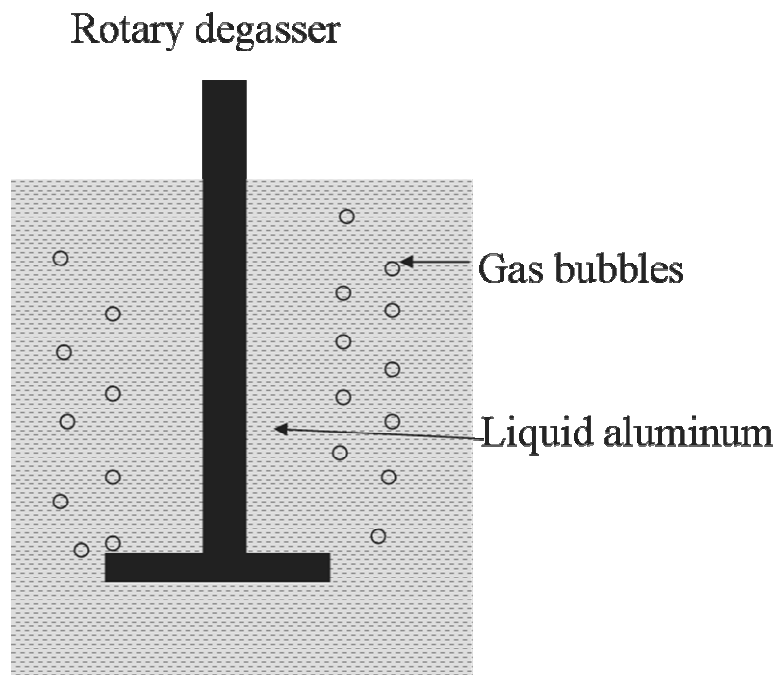


Figure 3 Fine dispersed gas bubbles produced by rotary unit for degassing molten aluminum.<sup>24</sup>

### 2.1.5 Hydrogen determination in aluminum melts

All the degassing techniques described reduce hydrogen levels to some extent. Gas content in the melt however does not remain constant as more hydrogen is continuously absorbed after degassing is completed. Proper control of the degassing process is only possible when the hydrogen content in the melt can be quantified.<sup>25</sup> Several methods have been developed and used by the aluminum casting industry to detect hydrogen.

A complete review of this topic has been presented by Makhlouf et al.<sup>26</sup> Three techniques for hydrogen detection, the reduced pressure test, AlScan/Telegas systems and electrochemical detection are described in this section.

**Reduced Pressure Test (RPT):** This simple test, also called the Straube-Pfeiffer test,<sup>27</sup> is a common technique used by foundry professionals to test the quality of their melt. Liquid metal is carefully poured into a small crucible and placed inside a vacuum bell jar. The metal then is allowed to cool down under the application of vacuum. The solidification process forms pores within the metal which are later examined by sectioning the sample. The nature and extent of porosity can be compared with reference photographic charts to estimate the hydrogen content in the melt. Additional information can also be obtained from pressure measurements and movement in the melt surface during solidification. Liquid metal samples with large amounts of dissolved hydrogen typically show a lot of surface movement on the application of vacuum.

A simple schematic of the RPT process is shown in Figure 4, while the photographic reference chart is shown in Figure 5. Although the RPT is a standard

industry procedure, it does not have high precision. The technique also requires considerable time for the sample to cool down before the hydrogen content in the melt can be estimated. For this reason, online sensors which can make in-situ hydrogen measurements are desired.

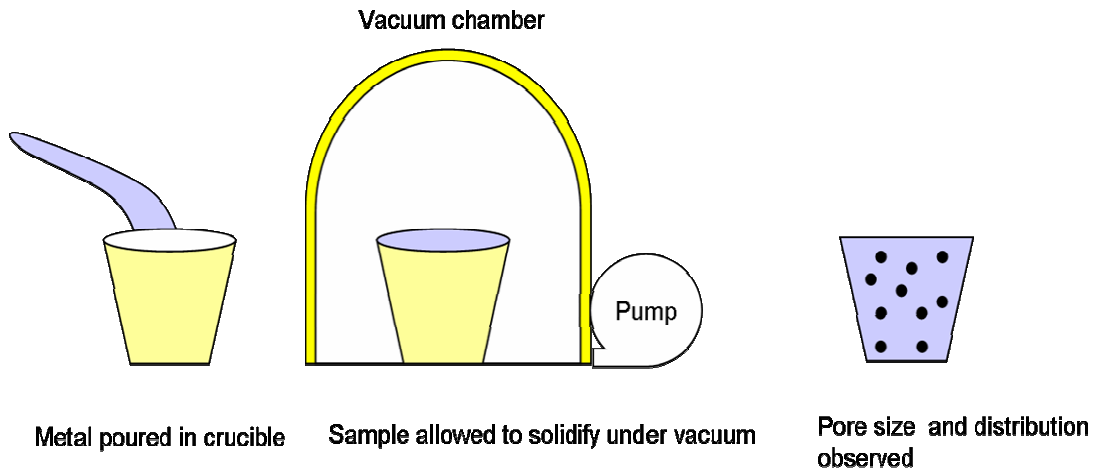


Figure 4 Steps involved in the reduced pressure test to estimate hydrogen content.

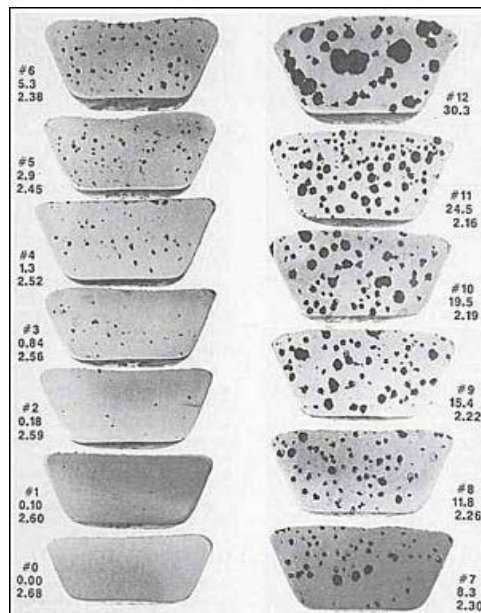


Figure 5 Standard photographic reference chart used to compare RPT samples showing estimates of porosity and sample density.

**Alscan/Telegas systems:** Commercial online systems for measuring the hydrogen content in molten aluminum are currently available (e.g. Telegas™ and AlScan™).<sup>28</sup> While Telegas is marketed by Alcoa,<sup>29</sup> Alscan was developed by Alcan based on the Telegas technique.

A schematic of the Alscan system is shown in Figure 6. In these systems, an inert gas like nitrogen is flowed through a porous ceramic probe that is suspended in the melt. Hydrogen from the melt equilibrates with the nitrogen gas stream.

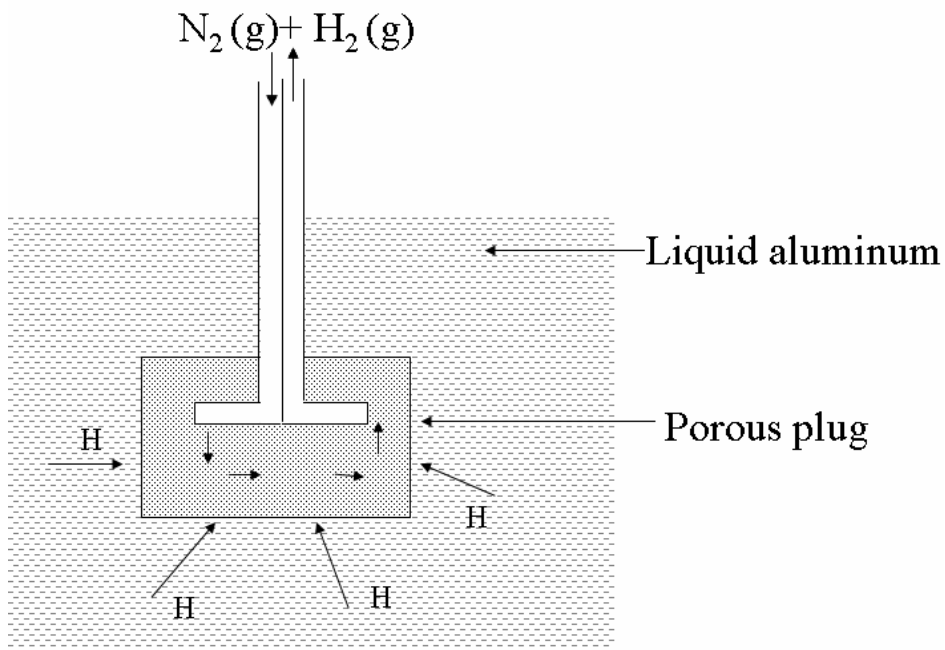


Figure 6 Schematic diagram of the Alscan probe.<sup>26</sup>

The equilibrium hydrogen concentration is given by Sievert's law<sup>30</sup> which relates the hydrogen concentration [H] in the melt to the hydrogen partial pressure over the melt (pH<sub>2</sub>) according to the equation,

$$[H] = S \cdot (pH_2)^{1/2} \quad (3)$$



where S is hydrogen solubility in the alloy melt (ml/100g, for 1 atm hydrogen). Hydrogen partial pressure in the melt is determined by measuring thermal conductivity of the nitrogen stream using a katharometer.

Alloying additions and melt temperature affect the solubility S, and are included in the following expression,<sup>26</sup>

$$[H] = S_0 \cdot (pH_2)^{1/2} \cdot CF(T) \cdot CF(A) \quad (4)$$

where  $S_0$  is the standard solubility in pure aluminum at 700°C, CF(T) is the temperature correction factor and CF(A) is the alloy correction factor. CF(A) depends on the concentration of the alloying elements and an equation to calculate CF(A) values for various aluminum alloys is given as,<sup>26</sup>

$$\log CF(A) = 0.017(\%Mg) - 0.0269(\%Cu) - 0.0119(\%Si) \quad (5)$$

The Alscan and Telegas systems have proved to be reliable and are the most widely units used in the industry. A 10-minute operation is generally used to produce consistent results. However, they are not without several drawbacks. The technique requires the transport of gas into and out of melt and thus devices are bulky and difficult to operate. The probe in these systems is quite fragile and tends to plug easily.<sup>26</sup> Also, these systems are cost prohibitive for several applications and have longer response times, so new designs, which can provide reliable data at an affordable cost are being developed.

**Electrochemical hydrogen sensors:** Potentiometric sensors based on solid electrolytes have found widespread application in the molten metals industry due to their ruggedness and stability at high temperatures.<sup>31</sup> These sensors offer the possibility of in situ measurement and faster response times.<sup>32</sup> Some disadvantages of such sensors include lack of sensitivity. However in many applications, the disadvantages are not prohibitive and many devices have been commercialized successfully.

Hydrogen sensors have also been developed for molten aluminum using the electrochemical technique. These devices typically measure the electromotive force (EMF) between the aluminum melt containing hydrogen (working) and an electrode whose hydrogen partial pressure is constant (reference). The measured voltage is directly related to the difference between the two hydrogen partial pressures and is given by the Nernst equation,

$$E = \frac{RT}{2F} \ln \frac{pH_2(I)}{pH_2(II)} \quad (6)$$

where R is the gas constant, T is the temperature, 2 for the number of electrons involved in the reversible reaction and F is Faraday's constant. Using such a device the hydrogen partial pressure could be calculated based on the measured EMF.

In 1978, Gee and Fray<sup>33</sup> developed a hydrogen sensor using CaH<sub>2</sub> as the solid electrolyte and Ca+CaH<sub>2</sub> as the reference electrode mixture. The solid state reference mixture fixed a stable hydrogen partial pressure and the sensor results were said to correlate with other measurement techniques. Thermal stability of the hydride-based

sensor materials was however a major concern as the device showed unstable responses and a short life.

Solid electrolyte based sensors based on proton conducting oxides have been investigated for use in molten metal applications. The use of an oxide material as the solid electrolyte imparts thermal stability to the device,<sup>34</sup> and various designs have been proposed and commercially tested. Zhuiykov<sup>35</sup> reviewed several proton conducting perovskite oxides and recommended the further research of barium and strontium cerates for use in various hydrogen sensors.

Among all the alkaline earth cerates and zirconates, indium-doped calcium zirconate became popular for use as solid electrolyte because of its excellent stability in molten aluminum. This compound has also been used to fabricate hydrogen sensors for copper and silver. Yajima et al.<sup>36</sup> developed a hydrogen sensor for molten aluminum based on indium-doped calcium zirconate electrolyte with a gas phase reference. The device used a gas phase mixture to fix the hydrogen partial pressure in the reference section. Figure 7 shows a schematic of the device developed for molten aluminum.

The electromotive force measured across this galvanic cell is given by the Nernst equation as shown in equation 6. The authors reported measurements that agreed with the theoretical voltage, so hydrogen concentration measurement with this method is possible. However, the method still involves a gas phase reference, which complicates sensor design.

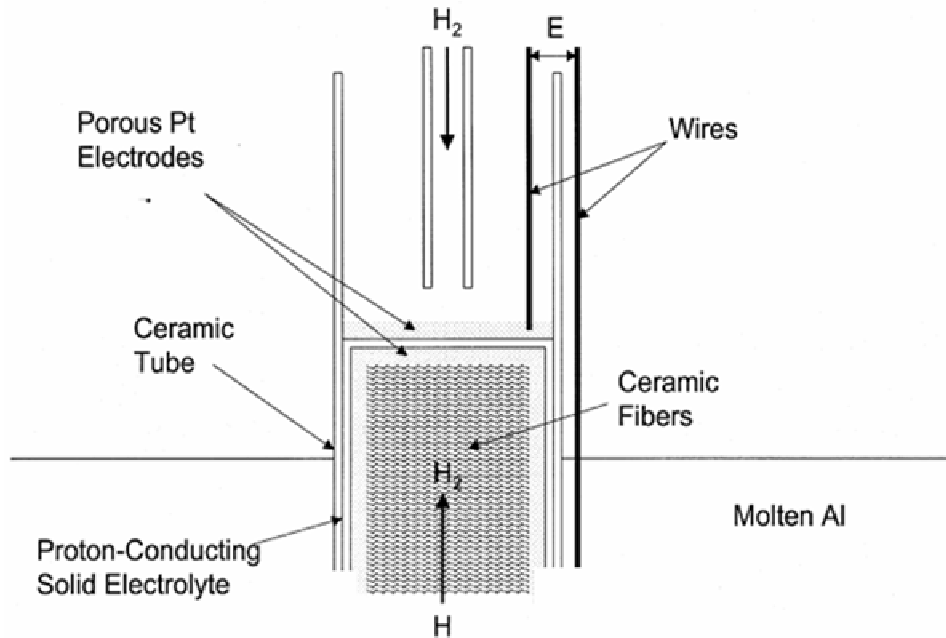


Figure 7 Schematic of a hydrogen sensor for molten aluminum.<sup>37</sup>

Zheng et al.<sup>37</sup> also constructed hydrogen sensors using doped  $\text{CaZrO}_3$  based materials. These devices made use of a condensed phase reference electrode containing a mixture of Ca and  $\text{CaH}_2$ . The use of the condensed phase electrode eliminates the need for transporting the gas into and out of the melt and thus can reduce device costs. However, the hydrides of Ca are extremely reactive and unstable even under controlled test conditions. To enhance the sensor stability, we proposed metal/metal oxide reference electrode systems using an In-doped calcium zirconate electrolyte for hydrogen sensing in molten aluminum.<sup>38</sup> The oxide electrodes might possess better stability and thus could be more suited for industrial use.

## 2.2 Electrochemical sensors based on solid oxide conductors

### 2.2.1 Introduction

A large number of chemical sensors are based on electrochemical principles. Electrochemical sensors are devices where analyte concentrations are determined by the charge exchange process at the electrodes. Electrochemical devices were first built with liquid electrolytes.<sup>39</sup> These were sometimes found to be bulky and clumsy. Drying or leakage of the electrolyte in these devices caused corrosion, shortened lifetime and limited functionality. Therefore, there has been a lot of progress in the direction of solid state electrochemical sensors.

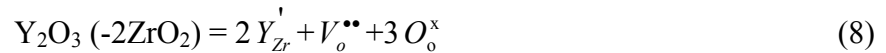
An important element of a solid state electrochemical sensor is the electrolyte across which a potential difference is established. In the case of high temperature applications, oxide-based ionic conductors are typically used because of their stability. The principles and application of various oxygen ion conducting solid electrolytes have been elaborately reviewed by Etsell and Flangas.<sup>40</sup>

Any material at  $T > 0$  K contains a specific number of imperfections, which are usually in the form of vacancies and interstitials. The presence of these is necessitated in a solid in thermodynamic equilibrium because of the entropy contribution to the Gibb's energy. Such defects fixed due to thermodynamic equilibrium, are called intrinsic defects. Since charge neutrality has to be maintained at all times, a positively charged defect is created for every negatively charged defect and thus the formation of ionic defect pairs is usually observed. Vacancy pairs and vacancy-interstitial pairs are common defects found in solid electrolytes.

Unlike certain halide conductors (fluorides), oxide materials rarely exhibit high ionic conductivity based on just intrinsic defects. Conductivity strongly depends on the number of charge carriers through the relation,

$$\sigma = n \cdot \mu \cdot e \quad (7)$$

where  $\sigma$  is the conductivity of the material,  $n$  is the number of defects,  $\mu$  is the defect mobility and  $e$  is the charge of an electron. Thus if the concentration of ionic defects were to be increased, the material's conductivity should improve. Extrinsic defects are typically produced by introducing aliovalent dopant ions into the lattice. A common dopant used in doping zirconia is yttrium oxide. Here,  $Y^{3+}$  cations occupy  $Zr^{4+}$  sites through the reaction,



The resulting relative negative charge leads to the creation of oxygen vacancies in order to maintain charge neutrality.

In an ion-conducting solid, the ions move between normal lattice positions. These ions are free to move through the lattice upon application of an electrical field or a concentration gradient. Ion movement usually occurs when the ion finds a vacant site or is able to move via an interstitialcy mechanism.<sup>41</sup> Ionic conductivity thus occurs due to imperfections (defects) in the lattice, which depend on the temperature and lattice elements.

Solid electrolyte systems could sometimes have more than one mobile defect species (oxygen vacancies, holes, protons, interstitials etc.). In such cases it is important

to know the individual species contribution to the overall conductivity. This is given by the transference number which is the fraction of the total conductivity contributed by each carrier. Transference number  $t_j$  is:

$$t_j = \sigma_j / \sigma_{\text{total}} \quad (9)$$

where  $\sigma_j$  is the conductivity of the mobile species  $j$  and  $\sigma_{\text{total}}$  is the total conductivity of the material.

The ionic transference number is the sum of all ionic contribution such that its sum with the electronic transference number should be unity. In the case of electrode applications in batteries, comparable contributions of electrons and holes could prove useful. However, for potentiometric concentration-type sensors, any electronic contribution to total conductivity is undesirable and a transference number close to 1 is preferred.

### 2.2.2 Use of solid electrolytes in sensors

Solid electrolyte based potentiometric devices are often used for detection of low concentrations and represent the most common class of sensors researched for high temperature applications.<sup>42,43,44</sup> In these devices, two electrodes are separated by a solid electrolyte material whose two sides are exposed to different concentrations of the species to be measured. The variation in species concentration establishes a chemical potential difference across the solid electrolyte.

In the case of charged particles like ions, the energy of the species also depends on the electrical potential of the region. This is given by the electrochemical potential which is the sum of the chemical potential and the contribution due to the electrical potential. A change in the electrochemical potential sets up a potential difference across the electrodes. Thus, the output of these devices is a D.C. voltage, which can be easily measured using a voltmeter.

A famous example of potentiometric devices for high temperature applications is the zirconia based oxygen sensor used in automotive applications.<sup>45</sup> Such sensors are solid oxide based potentiometric devices which measure a potential difference that occurs across the faces of an oxygen-ion conducting electrolyte. This potential difference is due to the difference in oxygen concentrations at the two faces of the electrolyte and is given by the Nernstian equation,

$$E = \frac{RT}{4F} \ln \frac{pO_2}{pO_2(ref)} \quad (10)$$

where  $pO_2$  is the oxygen partial pressure in the exhaust gas that needs to be measured,  $pO_2$  (reference) is the oxygen partial pressure fixed by the reference material and 4 is the number of electrons. Such sensors typically use air to establish a fixed reference oxygen partial pressure.

### 2.2.3 Sensor classification

Although potentiometric sensors are commonly used to measure species that are mobile in the electrolyte, this need not always be a requirement. In 1992, Weppner classified these types of devices according to the equilibrium that relates the activity of the species to be measured to the species that is mobile in the solid electrolyte.<sup>46</sup> In the



case of oxygen sensors using oxygen-ion conductors, no additional equilibria need to be established and these are called Type I sensors. The most common oxygen sensor used zirconia as a solid electrolyte which is usually doped in such a way that the dominant ionic defect is the oxygen vacancy.

Solid electrolytes can also be used to measure species that are present, but immobile in the electrolyte. These are called Type II sensors. An example of such devices are those developed by Alberti et al.<sup>47</sup> who report the use of phosphate based proton conducting electrolytes for developing oxygen sensors. In the case of Type III sensors, the electrolyte does not contain the species to be measured. However, the electrolyte contains a separate phase which equilibrates with the species to be measured and establishes a chemical potential which generates a response. The separate phase is termed as an auxiliary electrode and may be formed *in situ* or added separately at the start.

Sodium-ion conductors like  $\beta''$ -alumina<sup>48</sup> and NASICON<sup>49,50</sup> ( $\text{Na}_3\text{Zr}_2\text{Si}_2\text{PO}_{12}$ ) are excellent examples of solid electrolytes used in Type III sensors.  $\text{NO}_x$  sensors have been proposed based on devices using NASICON using  $\text{NaNO}_2$  as an auxiliary electrode. The typical cell structure for these sensors is,



where the gas-sensing reaction is,



Thus, by using  $\text{NaNO}_2$  as an auxiliary electrode, a  $\text{Na}^+$  ion conductor could be used to measure  $\text{NO}_2$ .  $\beta''$ -alumina based materials have been successfully used to develop magnesium sensors for molten aluminum. The  $\beta''$ -alumina based sensor establishes equilibrium between the dissolved magnesium in molten aluminum, and magnesium oxide and sodium oxide phases that are dissolved in  $\beta''$ -alumina to generate a voltage, corresponding to the magnesium concentration.

Potentiometric sensing devices are usually operated in open circuit conditions where no electrical current flows through the external circuit. A common source of error in some sensors is the presence of electronic conduction, which reduces the ionic transference number to below 1. Examples are high temperature applications like oxygen sensing in molten steel using zirconia-based electrolytes where temperatures around  $1600^\circ\text{C}$  increase  $\text{pO}_2$  at which electronic conductivity significant. With the onset of electronic conduction, there would be electrical current flowing through the electrolyte even under open circuit conditions. This would lead to lower voltage measurements than expected.

#### 2.2.4 Application of electrochemical sensors in molten metal processing

The choice of suitable materials is often the limiting factor in the development or improvement of high temperature technology. The harsh conditions prevalent in molten metals require materials to possess high mechanical and thermal stability. Since reaction rates are usually high at the high operating temperatures, materials should also possess high chemical stability. Zirconia-based solid electrolytes possess these qualities and have been used extensively in various sensor applications.

**Reference electrodes:** An important design consideration in the development of sensors for molten metals is the reference electrode. Gas phase reference electrodes are usually used in laboratory tests to fix a reliable reference concentration of the analyte to be detected. However there are inherent disadvantages associated with this type of electrode. Transport of gas into and out of the melt makes the sensor design complicated and bulky. Another drawback is the possibility of molecular gaseous species diffusing through the fine pores and microcracks of the electrolyte from the reference electrode to the liquid metal electrolyte interface. The gaseous enrichment will cause the reference potential to drift resulting in erroneous EMF readings. Hence, many investigations have been directed towards the development of chemically compatible solid reference electrodes.

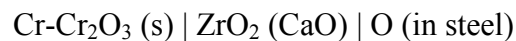
#### 2.2.5 Oxygen sensors for steel

One of the most common applications of solid electrolyte based potentiometric sensors is for oxygen sensing in molten steel.<sup>51</sup> During processing of molten steel, oxygen from reaction with surrounding atmosphere is removed by adding aluminum or silicon alloys. These react with the oxygen to form oxides, which are removed as slag. Determination of optimal amounts of alloys to be added requires knowledge of the oxygen content in the metal. An oxygen sensor can provide this information and such devices are used commercially in steel foundries.

The reference electrode used is a metal/metal oxide mixture that fixes a reference oxygen partial pressure on equilibrium. The most common reference electrode used is a Cr/Cr<sub>2</sub>O<sub>3</sub> mixture though the use of Mo/MoO<sub>2</sub> has also been studied. CaO stabilized

zirconia is used as the solid electrolyte up to 1600°C where oxygen partial pressures of about  $3 \times 10^{-13}$  atm (corresponds to 10 ppm oxygen in unalloyed iron) can be established. Below 10 ppm concentrations,  $ZrO_2$  (CaO) exhibits electronic conductivity and other electrolyte systems like  $ZrO_2$  ( $Y_2O_3$ )<sup>52</sup> and  $ThO_2$  ( $Y_2O_3$ )<sup>53</sup> have been developed to successfully measure oxygen activities corresponding to less than 1 ppm in steel.

The first important work in developing a galvanic cell based oxygen sensor for steel was done by Turkdogan et al.<sup>54</sup> who constructed a simple galvanic cell consisting of a  $ZrO_2$  (CaO) disc sealed into a silica tube. The tube was packed with a powder mixture of Cr and  $Cr_2O_3$ . The cell can be represented as



Pt or Mo wire was used to make contact with the electrode and suitable electrical contact was made with the melt. The cell was found to achieve a steady Nernstian response within 10 seconds of immersion into the melt.

Other designs proposed for oxygen sensing in steel are shown in Figure 8. Current oxygen sensors are of the disposable kind and devices have very short life times (Figure 8a).<sup>55</sup> Improving the seal between the reference electrode and molten steel can extend the lifetime of a sensor. Figure 8b shows a design where the zirconia electrolyte is isostatically pressed around the reference electrode. This provides a better seal for the reference electrode compared to the disposable sensor.<sup>51</sup> Another approach has been in the design of a non-isothermal sensor, in which the reference electrode is outside the

molten steel (Figure 8c). The reduced temperature lessens the requirements on the electrode seal.<sup>56</sup>

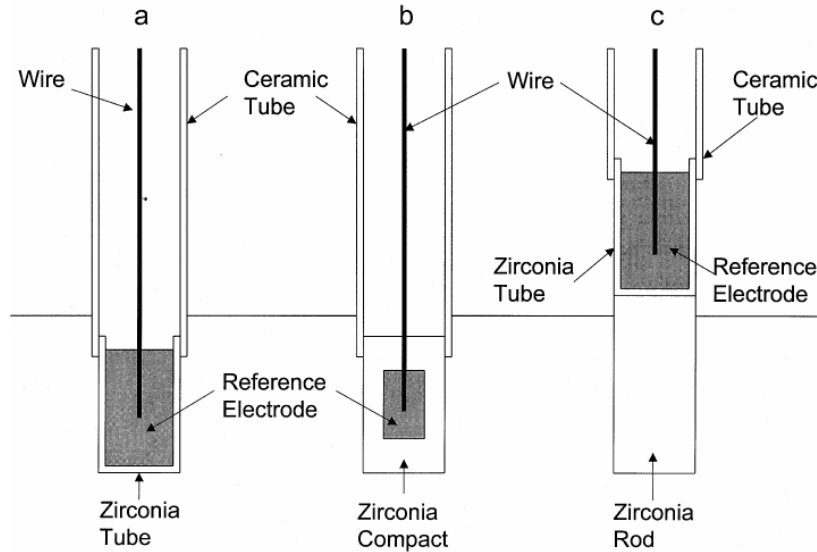


Figure 8 Schematic of typical designs for oxygen sensors for molten steel.<sup>55,51,56</sup>

### 2.3. Properties of calcium zirconate

$\text{CaZrO}_3$  has gained prominence as the material of choice for solid electrolyte applications in molten aluminum. A brief review of its structure, properties and applications will be presented in this section.

#### 2.3.1 Structure, properties and applications

$\text{CaZrO}_3$  is an equimolar phase of the  $\text{CaO-ZrO}_2$  binary system.<sup>57</sup> The phase diagram of this system (Figure 9) shows the material to remain stable upto  $\sim 2370^\circ\text{C}$  (melting point).  $\text{CaZrO}_3$  exists in two polymorphic forms: an orthorhombic phase at  $T < \sim 2000^\circ\text{C}$  and a cubic phase at higher temperatures. The precise phase transformation

temperature is not certain as values close to 1750°C and 1900°C have been reported. Two other Zr-rich ordered phases,  $\text{CaZr}_4\text{O}_9$  ( $\phi_1$ ) and  $\text{Ca}_6\text{Zr}_{19}\text{O}_{44}$  ( $\phi_2$ ) have been seen in limited temperature ranges.<sup>58,59</sup> A phase diagram detailing the formation and decomposition of these phases is shown in Figure 10.

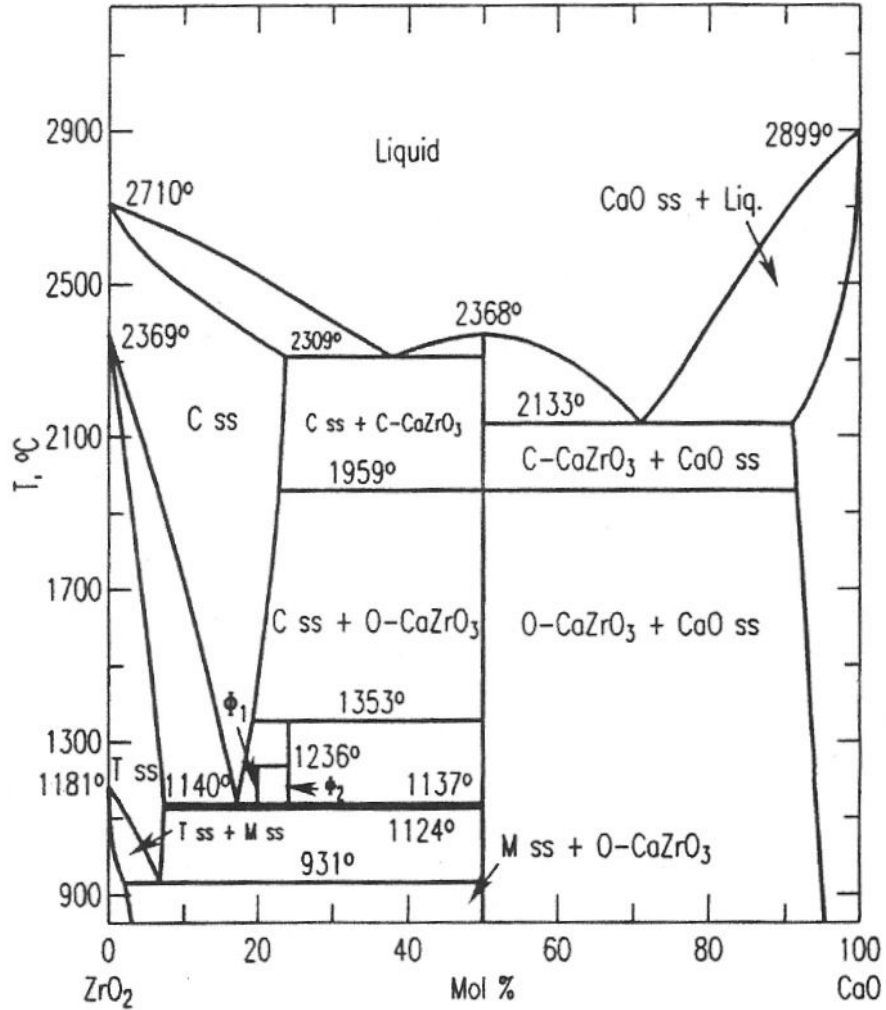


Figure 9 Phase Diagram of the CaO-ZrO<sub>2</sub> binary system.<sup>60</sup>

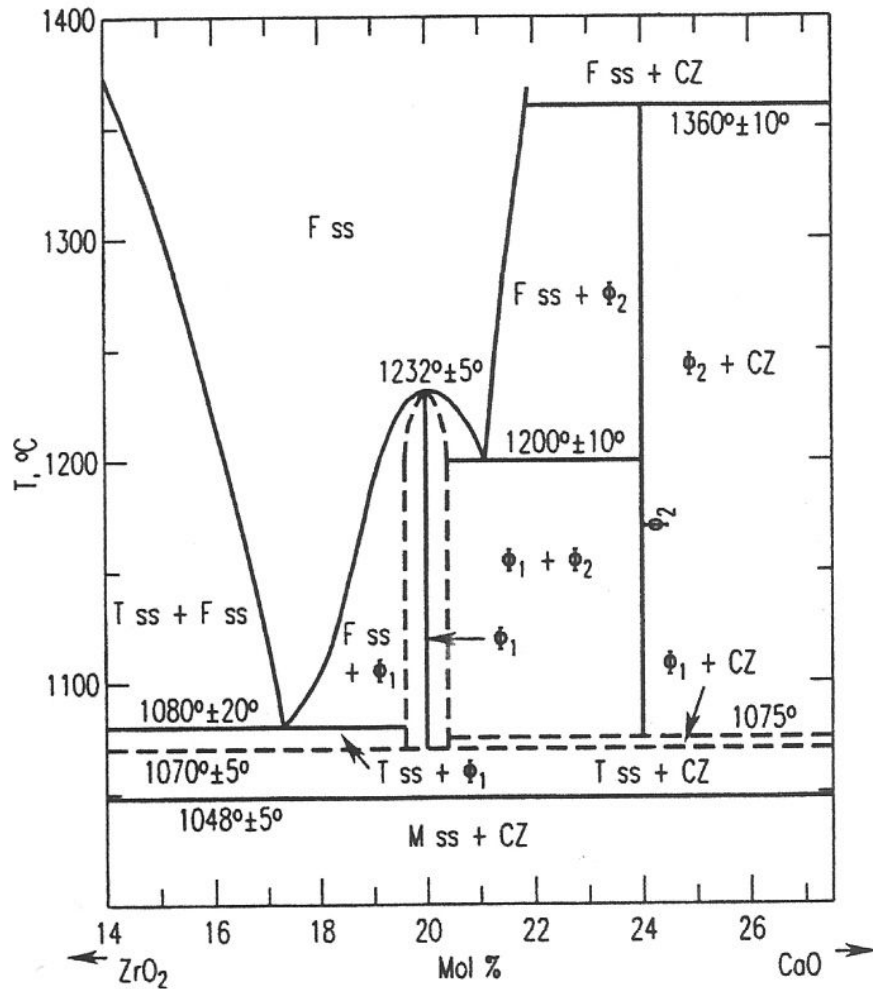


Figure 10 Phase diagram describing the decomposition of phases  $\phi_1$  and  $\phi_2$ .<sup>61</sup>

$\text{CaZrO}_3$  has been described to belong to the  $Pcmm$  symmetry group, isostructural with  $\text{CaTiO}_3$ .<sup>62</sup> The material has a perovskite structure comprised of corner sharing  $\text{ZrO}_6$  octahedra with the  $\text{Ca}^{2+}$  cation found in a 12-coordinate site. Unlike other common cubic perovskites such as  $\text{BaTiO}_3$  and  $\text{BaZrO}_3$ , the smaller  $\text{Ca}^{2+}$  cation makes the material orthorhombic with lattice parameters ( $a=5.5912 \text{ \AA}$ ,  $b = 8.0171 \text{ \AA}$ ,  $c = 5.7616 \text{ \AA}$ ,  $V = 258.26 \text{ \AA}^3$ ).<sup>63</sup> Figure 11 shows 2 schematic representations of the cubic perovskite structure drawn for  $\text{BaZrO}_3$ . The orthorhombic perovskite structure requires a tilt in the

ZrO<sub>6</sub> octahedra and Zr-O-Zr angles of 146° have been measured. All the atomic positions and bond distances for this material have been calculated by Shi et al.<sup>64</sup> using Density Functional Theory calculations. Figure 12 is taken from Islam's<sup>65</sup> representation of tilted octahedra observed in orthorhombic perovskites.

CaZrO<sub>3</sub> is an attractive material for a wide variety of applications. In 1998, Orera et al.<sup>66</sup> reported the characteristic infrared and Raman active modes of vibration, which were later confirmed by Zheng et al.<sup>67</sup> Orera and his coworkers proposed the use of CaZrO<sub>3</sub> doped with Er<sup>3+</sup> as an optical material due to its luminescence properties.<sup>68</sup> Waveguides designed using the material showed absorption and emission spectra of narrow bands along with high emission efficiencies.<sup>69</sup> CaZrO<sub>3</sub> has excellent catalytic and mechanical properties as porous composites have been offered for use in high temperature NO<sub>x</sub> filters<sup>70</sup> and lightweight structural components respectively.<sup>71</sup> The dielectric properties of CaZrO<sub>3</sub> have also been extensively studied.<sup>72</sup> The material has a dielectric constant ~30 and a quality factor ( $Q=1/\tan\delta$ ) of 3000 at 13 GHz.<sup>73</sup> The high

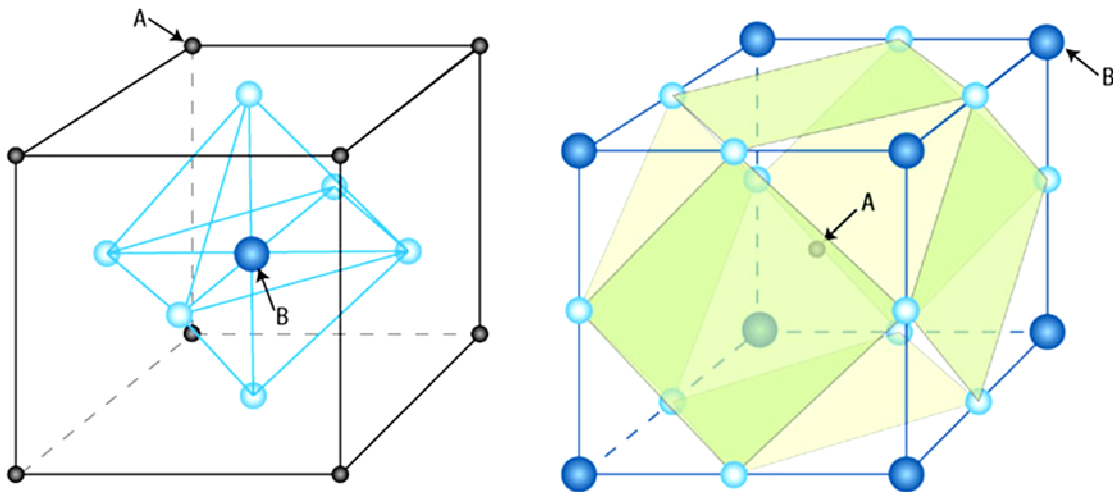


Figure 11 Schematic showing the ABO<sub>3</sub> type cubic perovskite structure of BaZrO<sub>3</sub>.<sup>74</sup>



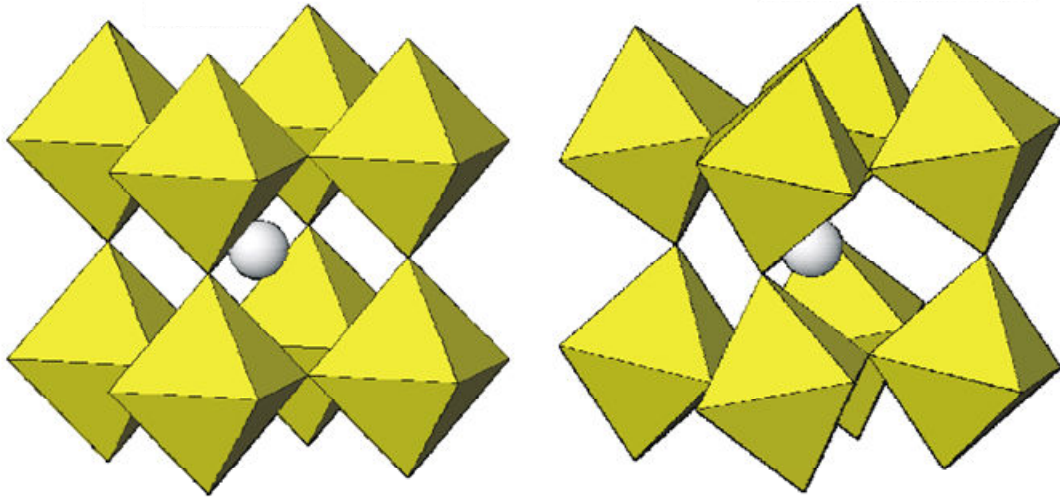


Figure 12 Structural comparison showing distorted  $ZrO_6$  octahedra in orthorhombic perovskites.<sup>63</sup>

dielectric constant combined with excellent thermal stability makes it attractive as a gate material for MOSFET applications.<sup>75</sup> Yu et al.<sup>76</sup> measured a leakage current density of  $9.5 \times 10^{-8} \text{ A/cm}^2$  at electrical field of 2.6 MV/cm.  $CaZrO_3$  additions have also been seen to greatly increase the dielectric constant<sup>77</sup> and temperature coefficient of capacitance (TCC) behavior<sup>78</sup> in  $BaTiO_3$  based capacitors.

### 2.3.2 $CaZrO_3$ based solid electrolyte materials

Since oxide basicity increases with increase in ionic size, mixed oxides containing Ca are thought to be more chemically stable than other typical oxides.<sup>79</sup> The stability of  $CaZrO_3$  based material combined with its ability to conduct ions, led to solid electrolyte applications in fuel cells and high temperature gas sensors.<sup>80</sup> Perhaps the widest studies of the material have been related to its electrical properties. The dominant defects in In-doped  $CaZrO_3$  were found to be holes, oxygen ions or protons depending on dopant type,

operation temperature and environment.<sup>81,82</sup> Wang et al.<sup>83</sup> doped  $\text{CaZrO}_3$  with small additions of  $\text{Al}_2\text{O}_3$ ,  $\text{MgO}$ ,  $\text{Y}_2\text{O}_3$  or a small excess of  $(\text{ZrO}_2, \text{CaO})$ , and found the material to be a hole-oxygen ion mixed conductor in air. Undoped  $\text{CaZrO}_3$  was found to be a p-type conductor at low temperatures and an oxygen ionic conductor at high temperatures. Following their initial study with alkaline earth cerates,<sup>84</sup> Iwahara and his coworkers reported protonic conduction in doped  $\text{CaZrO}_3$  in the presence of hydrogen.<sup>85</sup> Several studies detailing the electrical properties of the individual zirconates and cerates have since been conducted and review articles detailing various proton conducting ceramics and their applications have been published.<sup>86,87,88,89,90,91</sup>

Indium-doped calcium zirconate was first investigated for use as a proton conducting solid electrolyte in molten metal applications by Yajima et al.<sup>92</sup> Although the group published results showing conductivities in doped  $\text{CaZrO}_3$  were lowest among alkaline earth cerates and zirconates,<sup>93</sup> excellent chemical and mechanical stabilities made the material an attractive candidate for sensor applications in molten metal. In addition to being established as the material of choice in hydrogen sensors for molten aluminum applications, In-doped  $\text{CaZrO}_3$  has also been used in hydrocarbon sensors<sup>94</sup> and hydrogen isotope sensors<sup>95</sup>.

### 2.3.3 Proton conduction in In-doped $\text{CaZrO}_3$

Conduction mechanisms responsible for proton transport in doped cerates and zirconates have been reviewed previously.<sup>96,97</sup> The most popular theory involves presence of the protonic defect at the oxygen site in the form of a hydroxyl ion. Islam and his coworkers published a series of papers investigating protonic conduction in doped  $\text{CaZrO}_3$

by studying the influence of protons and dopants using *ab-initio* molecular dynamic simulation methods. The authors<sup>98</sup> reported that rotational and stretching motion of the O-H bond allowed protons to hop between oxygen atoms of adjacent octahedra rather than move as the hydroxyl ion. The equilibrium proton configuration was calculated to have an O-H bond distance of 1.01 Å. Energetics of the proton transfer was calculated from which activation energy of 0.74 eV was derived. A schematic of the steps involved in the proton conduction process is shown in Figure 13.

Formation energies of different Schottky and Frenkel defects in CaZrO<sub>3</sub> were computed by Davies and Islam.<sup>99</sup> The creation of Frenkel defects were seen to require high amounts of energy (> 4eV), indicating that the formation of ion interstitials is unlikely in the close packed perovskite structure. Proton-dopant interactions in the perovskite lattice have also been modeled by calculating binding energies associated with dopant-defect pairs.<sup>100</sup> A schematic of the defect-dopant interaction in CaZrO<sub>3</sub> is shown in Figure 14.

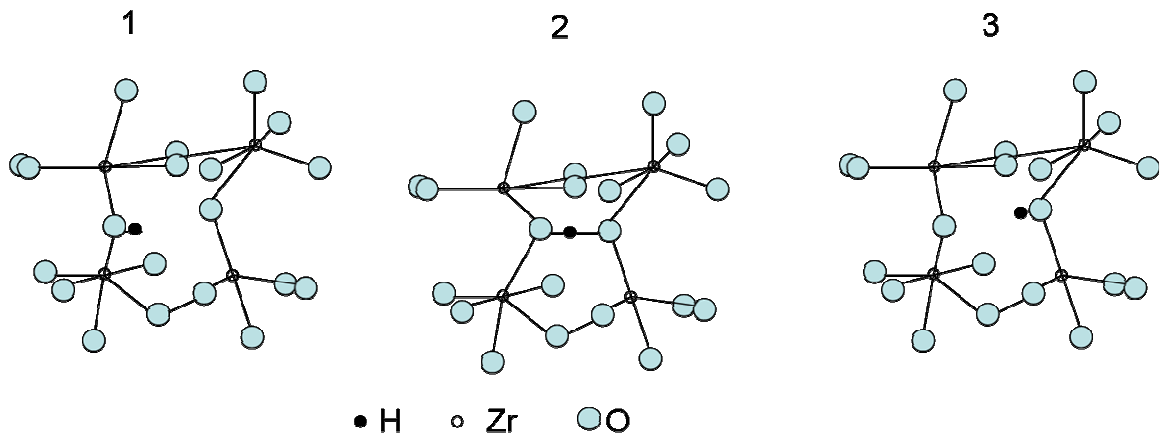


Figure 13 Schematic detailing steps involved in the transport of hydrogen through the CaZrO<sub>3</sub> lattice.<sup>99</sup>

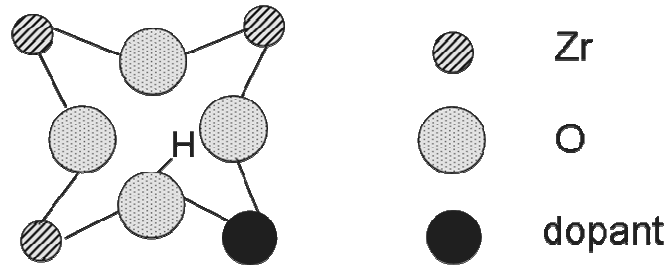


Figure 14 Proton-dopant interaction in  $\text{CaZrO}_3$  based materials.<sup>100</sup>

Table 1 these values for hydroxyl-dopant pairs for Ga, Sc and In computed using ab-initio methods. The negative value of E indicates that proton-dopant binding is favorable and might lead to defects being trapped at dopant sites. While less negative values were computed for Ga doping, In and Sc were both found to have higher binding energies. Yajima et al.,<sup>101</sup> however, report lower conductivities in Ga-doped  $\text{CaZrO}_3$  than In and Sc-doped  $\text{CaZrO}_3$ .

Dopant	E (eV)
Ga	-0.18
Sc	-0.30
In	-0.31

Table 1 Proton-dopant binding energies computed for In, Ga and Sc in  $\text{CaZrO}_3$ .

Experimental techniques have been used to confirm the presence of protons in cerates and zirconates. The trapping effect of protons at dopant sites has been independently confirmed in  $\text{SrZrO}_3$  based materials using muon spin relaxation measurements.<sup>102</sup> Knight<sup>103,104</sup> used neutron powder diffraction results to analyze

protonation in doped and undoped BaCeO<sub>3</sub>, and proposed a suitable site for the proton in the perovskite lattice. Infra-red spectra were used by Omata et al.<sup>105</sup> to identify three proton dissolution sites in In-doped CaZrO<sub>3</sub>. Higuchi et al.<sup>106</sup> used soft x-ray emission spectroscopy (SXES) and photoemission spectroscopy (PES) to investigate the presence of protons in In-doped CaZrO<sub>3</sub>. Energy differences between two proton-induced states suggest an activation energy of ~0.65 eV for protonic conduction. Hibino et al.<sup>107</sup> used temperature programmed desorption experiments and reported that proton concentrations and mobilities in In-doped CaZrO<sub>3</sub> were lower than other cerates and zirconates. This finding was also used to explain the lower conductivities in these materials as reported by Iwahara et al.<sup>93</sup>

Although many fundamental properties of a ceramic depend on structure, materials' synthesis also plays an important role in determining their final properties. It is therefore useful to choose an appropriate method for ceramic preparation. Some important techniques used to synthesize electrical ceramics, and in particular CaZrO<sub>3</sub> based materials, will be reviewed in the next section.

## 2.4 Ceramic Synthesis and Processing

### 2.4.1. Solid oxide synthesis

Mixed oxide materials have been traditionally synthesized using the solid oxide technique. This involves reacting individual oxides at high temperatures to form the desired product through a solid state reaction. Since this reaction requires intimate mixing and uniform distribution of the reacting materials, the starting oxides are first crushed and mixed together before the calcination. Powder milling reduces particle size which reduces diffusion distances for complete reaction of the cations. The method is simple and requires very little equipment. High calcinations temperatures and reaction times are, however, required. Contamination of the samples is also a possibility since the powders are in continuous contact with abrasive materials during the milling process.

The solid oxide route has been commonly used in the synthesis of alkaline earth cerates and zirconates. One of the early investigations involving  $\text{CaZrO}_3$  synthesis using the was reported by Nadler et al.,<sup>108</sup> who prepared single phase  $\text{CaZrO}_3$  by reacting  $\text{ZrO}_2$  with  $\text{CaO}$ ,  $\text{Ca(OH)}_2$  or  $\text{CaCO}_3$  at high temperatures. Of the different materials used,  $\text{CaCO}_3$  was found to show more complete reaction. This was attributed to better dispersion of the carbonate phase which produced a more active Ca species on dissociation. Pure  $\text{CaZrO}_3$  was also synthesized through the solid oxide route by Angers et al.<sup>109,110</sup> who annealed  $\text{CaO}$ -  $\text{ZrO}_2$  diffusion couples to grow  $\text{CaZrO}_3$  at the diffusion zone. The authors reported the formation of  $\text{CaZrO}_3$  to be strictly diffusion controlled by the transport of Ca in  $\text{CaZrO}_3$ . Yajima et al.<sup>101</sup> synthesized indium-doped calcium zirconate samples from powders of  $\text{CaCO}_3$ ,  $\text{ZrO}_2$  and  $\text{In}_2\text{O}_3$ . The oxide powders were

taken in the required proportions and mixed in a slurry using ethanol. Powders were then calcined, ball-milled, pressed and finally sintered to form the final sample pellet. Final powders were found to mainly contain  $\text{CaZrO}_3$  and the In-rich  $\text{CaIn}_2\text{O}_4$  phase.

#### 2.4.2. Wet chemical synthesis

Various wet chemical techniques have been developed to produce ceramic powders with a high level of homogeneity and small particle sizes. These involve the precipitation of oxides from a homogenous aqueous solution of the cations. Typical wet chemical methods include the sol-gel process, hydrothermal synthesis and oxalate coprecipitation.

**Sol-gel methods:** Reports on the sol-gel synthesis of  $\text{CaZrO}_3$  have previously been published.<sup>111,112</sup> This technique makes use of inorganic polymerization reactions to form an oxide network from molecular precursors. The use of molecular precursors reduces the temperature needed for powder sintering. End products usually have high purity and good homogeneity. The method also has its drawbacks as precursors are usually expensive. These chemicals do not have a long shelf life and are highly sensitive to moisture.

**Pechini method:**<sup>113</sup> This technique is a modified sol-gel process where cations are dissolved as nitrates or chlorides in aqueous solution. Chelation is then achieved by introducing an alpha hydroxycarboxylic acid like citric acid. A polyhydroxy alcohol like ethylene glycol is added to induce polyesterification at medium temperatures. This process results in the formation of a solid crosslinked polymer resin containing the cations in a highly homogenous mixture. Oxide powders are then obtained by burning the resin to remove all the organics.

**Hydrothermal synthesis:** Studies related to the hydrothermal synthesis of doped  $\text{SrZrO}_3$ <sup>114</sup> and  $\text{CaO-ZrO}_2$  solid solutions<sup>115</sup> have been reported. This technique does not require high calcination temperatures that are common to the other methods, as pressurized hot water is used to precipitate well-crystallized oxide powders. The method is simple and is easy to implement. It, however, needs high pressure equipment and reaction times can extend out into several days.

**Oxalate co-precipitation synthesis:** The oxalate coprecipitation process has become popular in the synthesis of precursor powders because of its simplicity and ability to produce large quantities of powder.<sup>116</sup> The method has been well researched and used to synthesize mixed oxide powders for superconductor<sup>117</sup>, semiconductor<sup>118</sup> and solid electrolyte<sup>119</sup> applications among many others. This precipitation method involves the precipitation of oxalate precursors by the addition of ammonium oxalate to the dissolved chloride or nitrate solution of the cations. Oxalate powders are usually more reactive which helps in shorter reaction times as well as reduced particle size.<sup>120,121</sup>



### 3. OBJECTIVES

This project aimed to investigate several aspects related to the development and fabrication of  $\text{Ca}(\text{Zr},\text{In})\text{O}_3$  based potentiometric sensors for hydrogen sensing applications in molten aluminum.

Specifically, the major research objectives of this study are –

1. To optimize the processes involved in fabrication of  $\text{CaZrO}_3$  based solid electrolyte tubes.
2. To investigate defect properties of  $\text{CaZrO}_3$  at a wide range of  $p\text{O}_2$ .
3. To design, construct, test and evaluate the performance of potentiometric hydrogen sensors for molten aluminum using oxide and hydride based reference electrodes.

## 4. EXPERIMENTAL METHODS

### 4.1. Ceramic preparation

**Solid oxide synthesis:** The solid electrolyte material was synthesized by calcining samples of  $\text{CaCO}_3$  (99.5%, Alfa Aesar),  $\text{In}_2\text{O}_3$  (99.99%, Alfa Aesar) and  $\text{ZrO}_2$  (99.9%, Alfa Aesar). Starting oxides were first weighed and crushed together using a mortar and pestle. The powder mixture was mixed with ethanol (absolute grade, Pharmco) in a glass jar, with a 3:1 ratio of ethanol to powder. Cylindrical zirconia beads were added to the glass jar and then set on twin rollers of a rotary ball-mill (#CZ-921 6T, U.S. Stoneware) for 5 days. Ethanol was evaporated away from the sample after milling by drying the sample at room temperature. The milled powder was then placed in an alumina boat and calcined at various temperatures using a hot furnace. A tube furnace (#2-221, Mellen) was used for calcinations up to  $1200^\circ\text{C}$ , whereas heating up to  $1400^\circ\text{C}$  was achieved using a high temperature muffle furnace (#46100, Thermolyne). Typical calcination times used were 5-24 hours. All calcinations were done in laboratory air.

**Oxalate Co-precipitation Synthesis:** Liquid phase synthesis of the mixed oxide was achieved by first precipitating oxalate precursor powders. The starting materials,  $\text{ZrOCl}_2 \cdot 8\text{H}_2\text{O}$  (99.9%, Alfa Aesar),  $\text{CaCO}_3$  and  $\text{In}_2\text{O}_3$ , were first dissolved in a 1:1 solution of concentrated HCl and distilled water by heating at  $70^\circ\text{C}$  amidst constant stirring. Crystals of  $\text{ZrOCl}_2 \cdot 8\text{H}_2\text{O}$  were dissolved in distilled water using stirring and

added to the acidic solution. This solution (Solution A) was then introduced drop-wise into an alkaline solution of oxalic acid (Solution B), which was maintained at pH 9 by adding  $\text{NH}_4\text{OH}$  (Fischer Scientific). An excess amount of oxalic acid was used to ensure complete precipitation of the cations. The resulting curdy white solution (Solution C) was stirred continuously for 30 minutes at  $50^\circ\text{C}$ , and then allowed to age for 3 hours. The precipitate was separated by filtration, and washed 3 times using distilled water to remove chloride impurities from the powders. Chloride removal was checked by adding few drops of silver nitrate to the supernatant solution, as a white silver chloride precipitate was seen to form immediately in the presence of the chloride. The chloride free precipitate was finally washed with ethanol and allowed to room dry for 12 hours. The precursor powders were dried for 12 hours at  $100^\circ\text{C}$  to remove moisture and then calcined for perovskite formation. A calcination procedure similar to that described for the solid oxide synthesis was followed.

Solution A	$\text{ZrOCl}_2 \cdot 8\text{H}_2\text{O} + \text{CaCO}_3 + \text{In}_2\text{O}_3$ dissolved in $\text{HCl} + \text{H}_2\text{O}$ and stirred at $70^\circ\text{C}$
Solution B	Oxalic acid crystals dissolved in distilled water + $\text{NH}_4\text{OH}$ , pH 9
Solution C	Solution A added slowly into B, stirred at $50^\circ\text{C}$

Table 2 Solutions A, B and C used in the co-precipitation synthesis of  $\text{Ca}(\text{Zr},\text{In})\text{O}_3$

To investigate the efficacy of using surfactants in oxalate coprecipitation, precursor powders were also synthesized using polyethylene glycol (PEG). In this process, 5 wt % PEG 200 (Sigma-Aldrich) was first mixed with distilled water and added to Solution A. Flakes of PEG 1450 (Sigma) were then dissolved in ethanol and added to

Solution C. The rest of the procedure was similar to that described already. The advantage of adding a ball-milling step to the coprecipitation process was explored by wet milling dried precursor powders using ethanol for 2 days. The milled precursors were then calcined using previously described procedure.

Flowcharts depicting the two different synthesis processes are shown in Figure 16. Mg-doped  $\text{CaZrO}_3$  powders were synthesized using the exact same process described above, but using MgO as the starting oxide instead of  $\text{In}_2\text{O}_3$ .

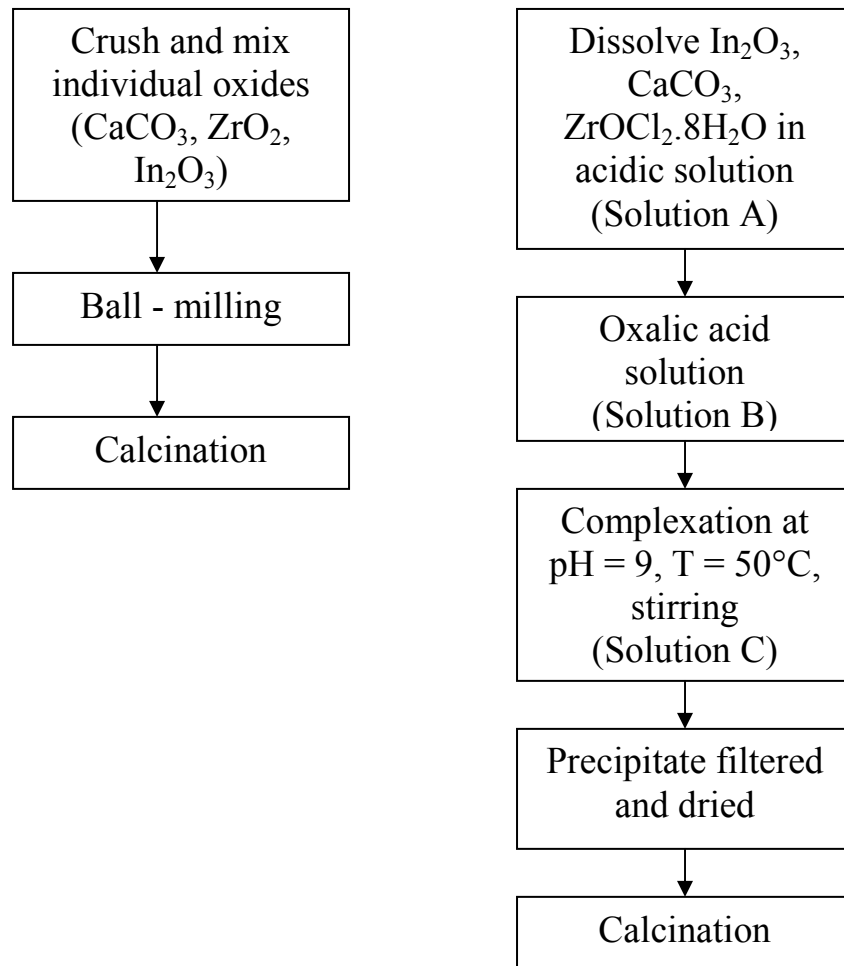


Figure 15 Flowcharts of the solid oxide (left) and co-precipitation synthesis (right) processes used to synthesize the solid electrolyte material  $\text{Ca}(\text{Zr},\text{In})\text{O}_3$

## 4.2. Powder characterization and processing

**Materials Characterization:** Powders prepared by the solid oxide and co-precipitation processes were characterized using different techniques.

1. X-ray Diffraction (XRD): Powders were placed on a glass slide and the surface was flattened with a spatula. The slide was then inserted into a Rigaku DMAX-B vertical diffractometer. Powder samples were exposed to X-rays (40 kV, 40 mA) from a Cu-target and the intensity of the diffracted x-rays was measured between 20° and 90° using a detector. A scan speed of 5 degrees/min and a sampling interval of 0.05 degrees were typically used.
2. Scanning Electron Microscopy (SEM): Powders obtained from the synthesis processes were stuck on conductive carbon tape and then gold coated using a sputter coater. JEOL JSM 840 and JEOL JSM 7000F FE-SEM were operated at 20 kV to take secondary electron images at high magnifications. Compositional analysis of the powders was accomplished using the Oxford Instruments Electron Dispersive X-ray Spectroscopy (EDS) system.
3. Fourier Transform Infra Red Spectroscopy (FTIR): Powder samples were first mixed with KBr (Wilmad Glass Co.) and then pressed uniaxially to form pellets. Measurements were made in the transmissive mode within a spectral region of 400-4000  $\text{cm}^{-1}$  using the Perkin Elmer Spectrum GX FTIR.
4. Particle Size Analysis: Microtrac S3500 system employing laser scattering was used to analyze sizes of the various particles in the solution.

**Processing:** The calcined powders were used to form solid electrolyte pellets and tubes. Pellet samples were fabricated by first compacting the powders using a stainless steel

mold. Powders were placed in the mold and pressed under uniaxial load for 2 minutes before removal. Mold Wiz® F-57 NC was used as a release agent to prevent the compacted particles from sticking to the mold walls. Pressed pellets of the solid electrolyte were placed in an alumina boat and sintered at temperatures between 1200°C and 1400°C for 9 to 18 hours. Pellets of 8-10 mm diameter and 2-3 mm in thickness were obtained.

Solid electrolyte tubes were fabricated using slip casting. A schematic detailing the process steps is shown in Figure 16. Calcined powders were ball-milled for 7 days with ethanol to form a slurry mixture. Alumina powder (99.9%, Johnson Matthey) was then hand-compacted with a cavity into which the slurry was poured. The liquid was allowed to wet the walls of the mold for approximately 5 minutes after which the excess was drained off. The cast tube was allowed to dry in the mold for 12 hours at room temperature. The mold was then broken open and the green tube removed. Alumina impurities on the surface of the tube were carefully brushed away. The tube was finally sintered by placing in the furnace and heated at temperatures between 1200°C and 1400°C for 9 to 18 hours. The resulting sintered closed-one-end tubes were ~20 mm in length, 4-5 mm in diameter and had a wall thickness of 0.8-1 mm.

Experiments were also conducted to investigate the effect of particle size on settling. Small amounts of powder were added to water taken in a 10 ml graduated cylinder and then allowed to settle after shaking. The liquid column slowly separated into a clear region and a turbid region containing the powder particles. The height of the turbid region was measured as a function of settling time.

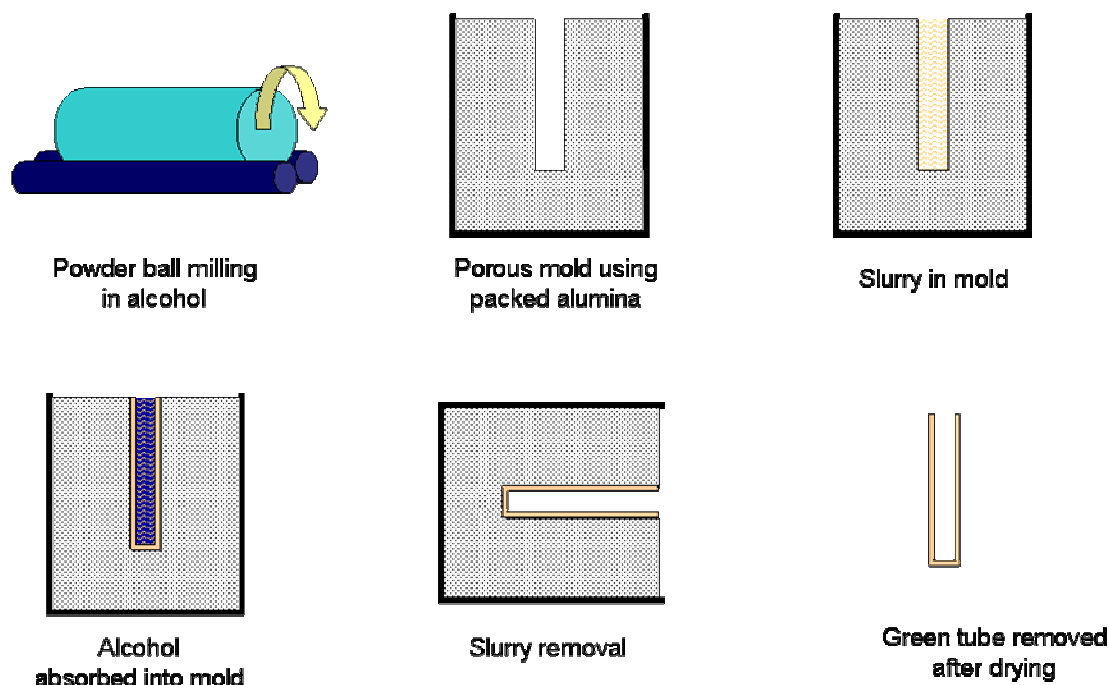


Figure 16 Process steps involved in the forming of fresh electrolyte tubes using slip casting

#### 4.3. Electrical measurements

A.C. impedance and 2-probe D.C. resistance measurements were performed to characterize the electrical properties of the material. Pellet samples with platinum electrodes were used for these experiments. Platinum paste (A 3786, Engelhard) was applied uniformly over the faces of the pellet. The organic binder was burnt away by heating the pellet at 800°C for 3 hours. The pellet was then spring-loaded into a sample holder which was inserted into a tube furnace and heated to temperatures between 600°C

and 1000°C. Samples were tested in an inert atmosphere by passing argon gas through the furnace. To test the samples in a moisture-rich environment, the gas was passed through water before entering the furnace. The relative humidity in the laboratory was measured. Conductivity measurements were also made in laboratory air. Molybdenum wires (99.95%, Alfa Aesar) were used as contact leads in the case of reducing environments (Ar, Ar+H<sub>2</sub>O) whereas platinum wires (unalloyed, Aldrich) were used for experiments conducted in air. Pieces of platinum foil (99.9%, 0.1 mm thick, Aldrich) were placed on both sides of the pellet to improve electrical contact.

2-probe D.C. measurements were carried out at temperatures between 600°C and 1000°C by measuring the resistance across the pellet using a Fluke 887B Graphic Multimeter. Temperatures were set and controlled using Syscon REX-C100 temperature controllers and a solid state relay. A.C. impedance measurements were made at the same temperature range using the Solartron SI 1260 Impedance/Gain Phase Analyzer. A perturbation signal of 5-10 mV was applied across the pellet and the resulting impedance curves were analyzed and fitted using the Complex Non-linear Squares (CNLS) software tool available in the ZView package.

Impedance spectroscopy was also used to study the material properties at low oxygen partial pressures. The closed-one-end electrolyte tubes were filled with aluminum powder. Molybdenum wire (1.27-mm diameter) was inserted in a ceramic sleeve and suspended into the electrolyte tube to act as one of the lead wires. The electrolyte tube was then inserted into a 3-cm long alumina support tube and sealed using the Aremco 517 sealant. The assembly was then suspended in a graphite crucible filled with aluminum powder. A molybdenum wire inserted into a ceramic tube was also suspended



in the aluminum powder inside the crucible. The graphite crucible was suspended in a quartz tube, which was heated in a tube furnace at different temperatures between 500°C and 1000°C. Dry argon was flowed into the furnace to maintain a very low oxygen pressure. A schematic of the cell is shown in Figure 17.

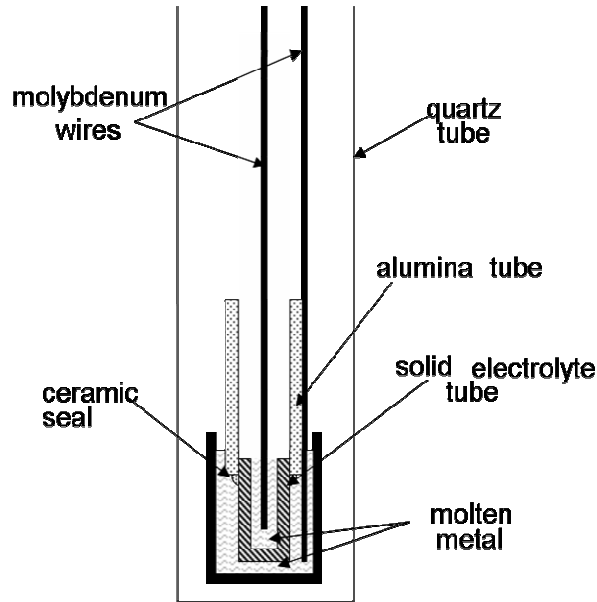


Figure 17 Schematic of cell design used to measure impedance at very low oxygen pressures. Very low oxygen partial pressures are fixed on opposite sides of the electrolyte by using molten aluminum.

#### 4.4. Sensor fabrication and testing

Solid electrolyte tubes were used to construct hydrogen sensors. Tubes were first manually filled with the reference electrode materials, which were a mixture of metal-metal oxide or metal-metal hydride. Powder mixtures of magnesium (99+%, Aldrich)-magnesium oxide were typically used as oxide based reference electrodes while calcium (98.8%, Alfa Aesar)-calcium hydride (98%, Alfa Aesar) or zirconium (99.95%, Alfa

Aesar)-zirconium hydride (99.7%, Alfa Aesar) mixtures were used as hydride electrodes. In the case of magnesium-magnesium oxide electrodes, magnesium powder was added to the tube. It was assumed that some of the magnesium would react with residual oxygen to form MgO at the high operation temperatures and provide the oxide phase necessary to establish equilibrium. No additional magnesium oxide powder was therefore added to the reference electrode.

A molybdenum lead wire sheathed in a alumina sleeve was inserted into the electrolyte tube to act as the reference lead. The open mouth of the tube was sealed with a ceramic adhesive (Ceramabond 571-P, Aremco Products). The reference assembly was cased inside a porous alumina tube (Fairey Ceramics) which has better thermal shock resistance than high density alumina.

**Gas phase measurements:** Laboratory tests were conducted by suspending the assembly in a tube furnace through which argon with varying hydrogen concentrations was passed. Ar-5% H<sub>2</sub> gas was used as the hydrogen source from which different hydrogen partial pressures were established by mixing with pure argon. Voltage measurements were made between the wire inserted inside the solid electrolyte tube (reference), and a molybdenum wire (working) which was wrapped around the outside of the tube (working). Platinum electrodes were applied on the tube surface as previously described for experiments involving gas phase measurements.

**Testing in molten metal:** For measurements in liquid metal, the sensor assembly was sealed within steel tubes to add structural integrity and provide better protection from the harsh melt environments. The working section of the sensor was constructed by inserting a molybdenum wire into an alumina sleeve. A schematic and a photograph of

the final construction of the sensor and its actual picture are shown in Figure 18 and Figure 19 respectively.

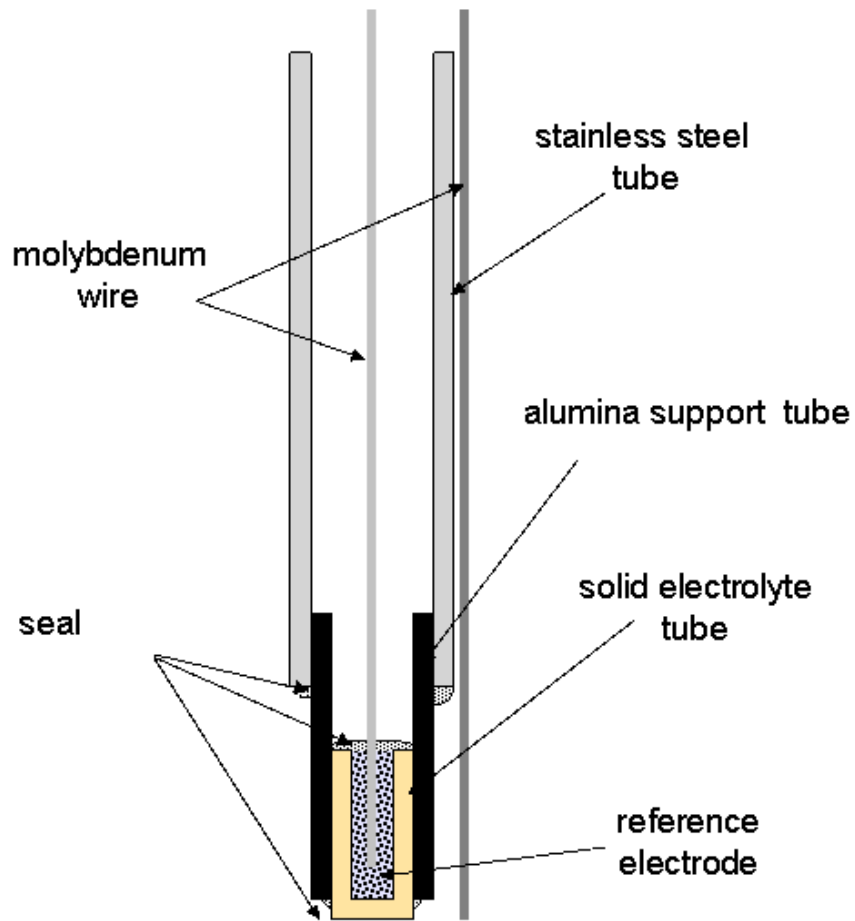


Figure 18 Schematic of the  $\text{Ca}(\text{Zr,In})\text{O}_3$  based potentiometric sensor designed to detect hydrogen in molten aluminum. Metal-metal oxide and metal-metal hydride mixtures used as condensed phase reference electrodes.

Aluminum alloy ingots were melted using an induction furnace. At a temperature of  $720^\circ\text{C}$ , sensors were inserted into the melt. Care was taken so that probes went past the alumina slag layer at the surface and became in contact with the liquid metal. D.C. voltage measurements were made periodically between the two lead wires. The furnace power was turned off during measurements as this was found to affect sensor readings.

Hydrogen content was reduced by flushing the melt with argon carrier gas. During runs involving degassing, the sensor was pulled out from the melt and reinserted after degassing. This was done to prevent any structural damage to the probe.

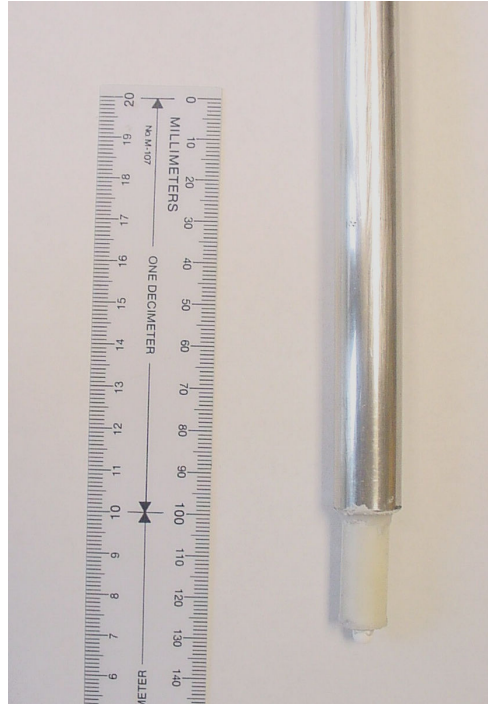


Figure 19 Picture of a sensor prototype constructed for pilot plant testing

**Pilot plant experiments** were conducted at the Canadian Metallurgical Laboratories, Ottawa, CA. Sensors were tested along with a commercial AlScan hydrogen analyzer in various commercial aluminum alloys. A picture describing this experiment is shown as Figure 20. About 20 kg of the charge material was melted in a box furnace and the temperature was controlled at 730°C. AU sensors were first dipped into the melt, after which the AlScan probe was introduced. After the initial measurements, rotary degassing was performed to change the hydrogen content in the melt (Figure 21). The two probes were then reinserted after degassing to simultaneously

estimate the reduction in hydrogen levels. Liquid metal samples were taken before and after degassing for reduced pressure test experiments. Liquid aluminum was poured into a small crucible which was placed under a bell jar. The sample was allowed to solidify under vacuum, after which it was sectioned for porosity examination.

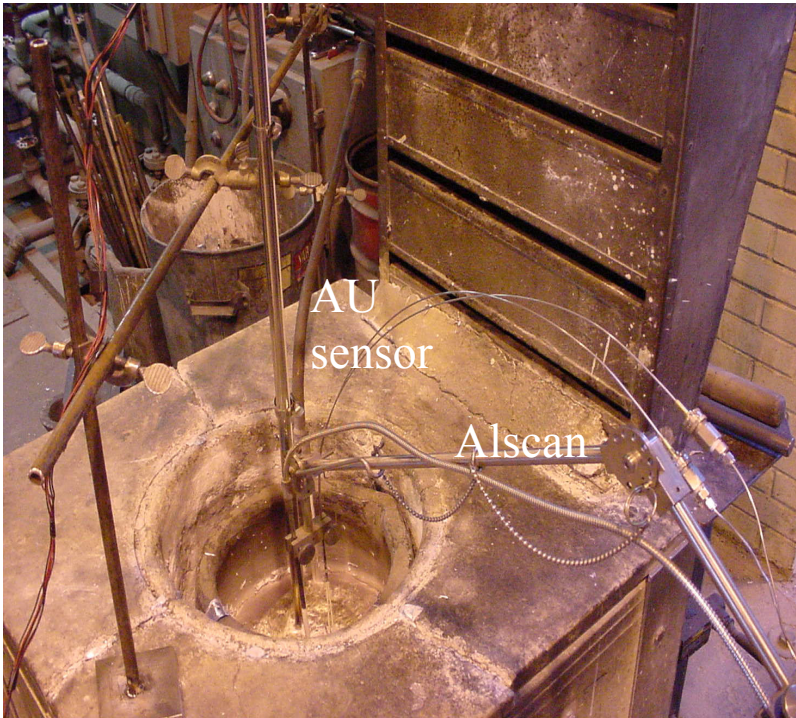


Figure 20 AU sensor and AlScan making simultaneous measurements in a commercial alloy melt at CANMET, Ottawa CA.



Figure 21 Commercial rotary degasser used to reduce hydrogen content in the melt between sensor measurements.

## 5. RESULTS AND DISCUSSION

### 5.1 Synthesis, processing and characterization of doped and undoped calcium zirconate

#### 5.1.1 Solid oxide synthesis

The material  $\text{CaZr}_{1-x}\text{In}_x\text{O}_{3-x/2}$  ( $0 \leq x \leq 0.2$ ) was first prepared using the solid oxide technique. Phases involved in the formation of  $\text{CaZrO}_3$  were evaluated using X-ray diffraction (XRD). XRD patterns from the individual oxides ( $\text{CaCO}_3$ ,  $\text{ZrO}_2$ , and  $\text{In}_2\text{O}_3$ ) were obtained for comparison and are shown in Figure 22, Figure 23 and Figure 24. XRD spectra obtained from 10 mol% In-doped  $\text{CaZrO}_3$  prepared from the solid oxide route are shown in Figure 25.

Figure 25 shows x-ray diffraction peaks from oxide mixtures which were calcined at 3 different temperatures (1000°C, 1200°C and 1400°C) for a period of 12 hours. Peaks matched well with those attributed to the orthorhombic  $\text{CaZrO}_3$  phase and were indexed with reference card (#35-0790) obtained from the Joint Committee on Powder Diffraction Standards database (JCPDS). The peak positions show good agreement with the diffraction profile obtained from commercially available  $\text{CaZrO}_3$  (Aldrich) shown in Figure 25. Peaks appear to be well-formed indicating crystalline nature of the synthesized product.

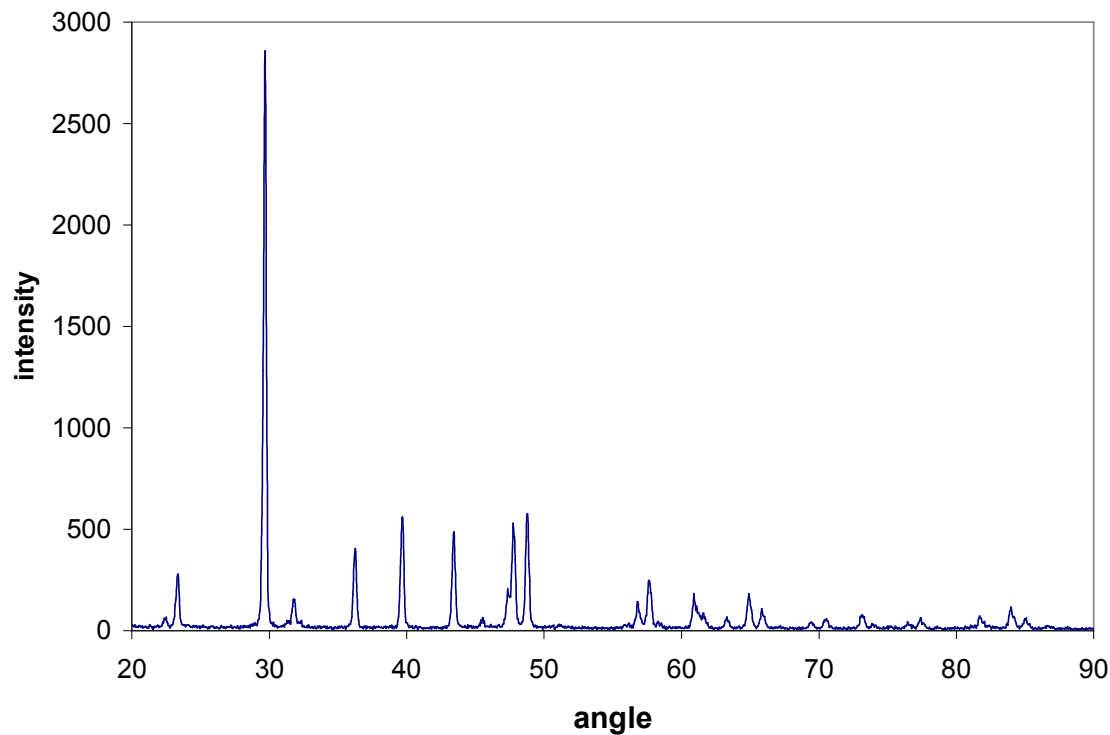


Figure 22 XRD pattern from a pure sample of CaCO<sub>3</sub> used in the solid oxide synthesis

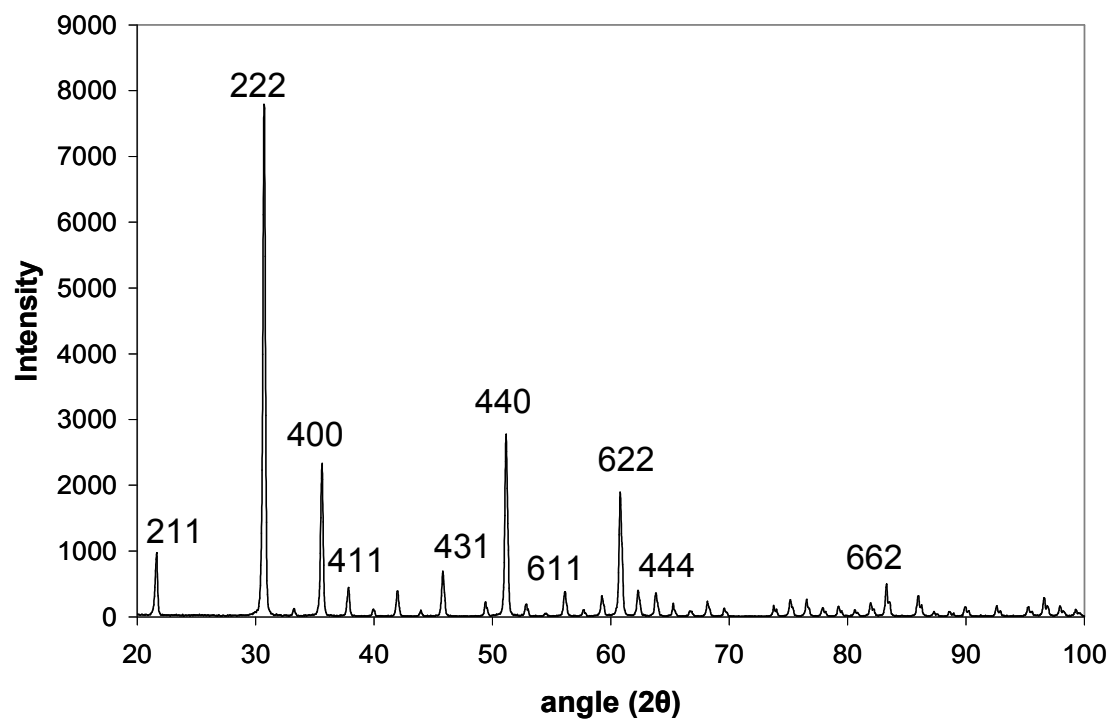


Figure 23 XRD pattern from a pure sample of In<sub>2</sub>O<sub>3</sub> used in the solid oxide synthesis



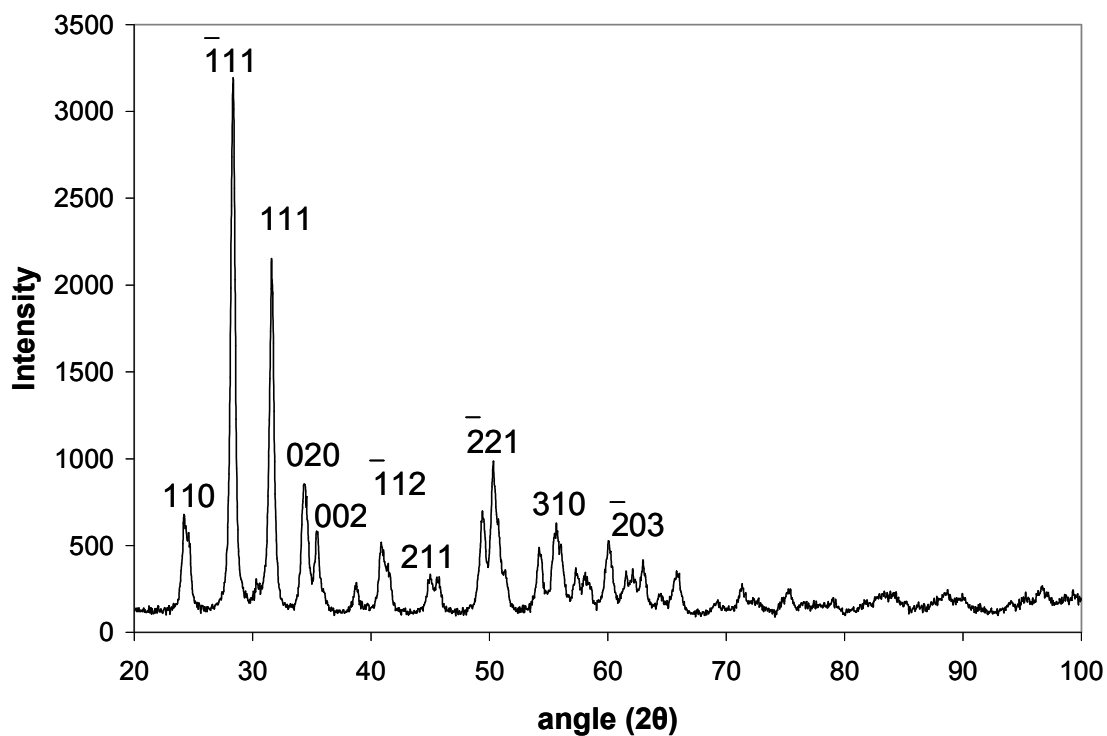


Figure 24 XRD pattern from pure  $ZrO_2$  used in the solid oxide synthesis

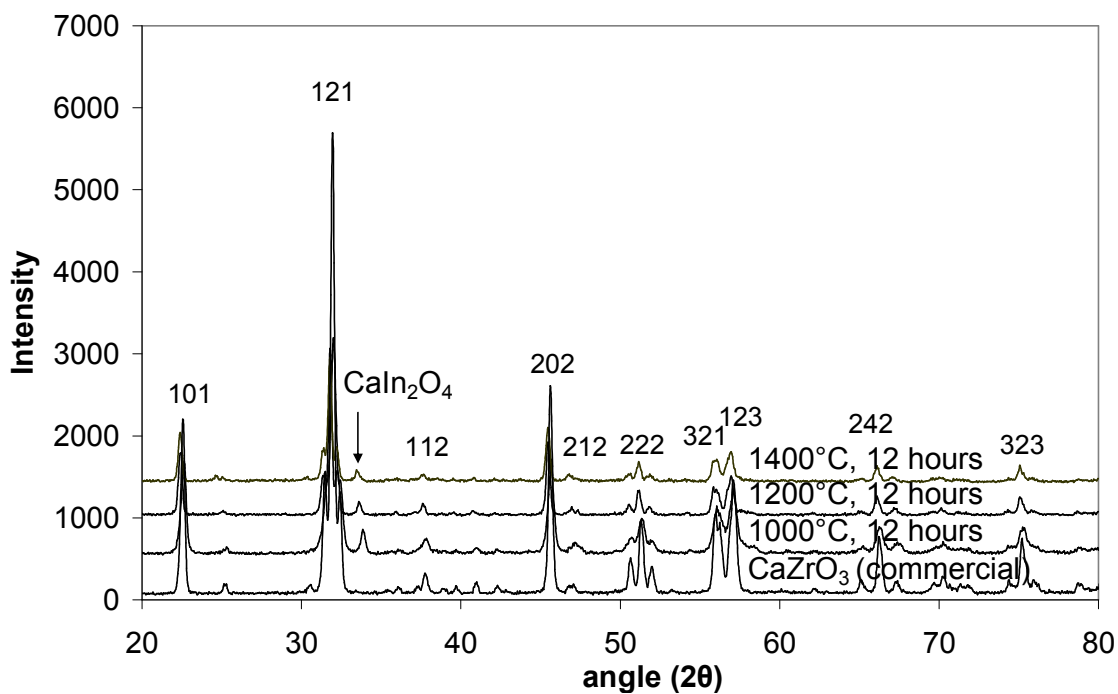


Figure 25 XRD pattern from  $CaZr_{0.9}In_{0.1}O_{2.95}$  synthesized using the solid state route

The XRD pattern in Figure 25 also shows a separate peak at  $2\theta = 33.4^\circ$ , which could not be indexed to the perovskite phase. The position however, matches well with the (121) peak of the In-rich  $\text{CaIn}_2\text{O}_4$  phase (JCPDS #17-0643).<sup>92</sup> This suggests that all the indium was not completely dissolved in the perovskite lattice, such that the doped powders prepared from the solid oxide route are a mixture of two phases ( $\text{CaZrO}_3 + \text{CaIn}_2\text{O}_4$ ).

## 5.1.2 Oxalate coprecipitation synthesis

### 5.1.2.1 Precursor synthesis and characterization

Oxalate decomposition to form  $\text{CaZrO}_3$  was investigated as an alternate to the solid oxide route of synthesis. The precursor oxalate was first synthesized through a coprecipitation reaction of the cations using oxalic acid as a chelating agent. Figure 26 shows typical XRD results from oxalate precursor powders obtained after drying. Powders are clearly seen to have some amorphous character at regions around  $30^\circ$ . Although crystalline features are also visible in the spectrum, the peak intensities are quite low compared to the peaks obtained from the solid oxide samples, indicating lesser crystallinity in the precursor powders.

The crystalline peaks in Figure 26 can be attributed to the monoclinic  $\text{CaC}_2\text{O}_4$  phase and were indexed based on the JCPDS reference card (#21-0838). While the presence of this phase is consistent with other published reports, there has been disagreement over the other phases present in the system.

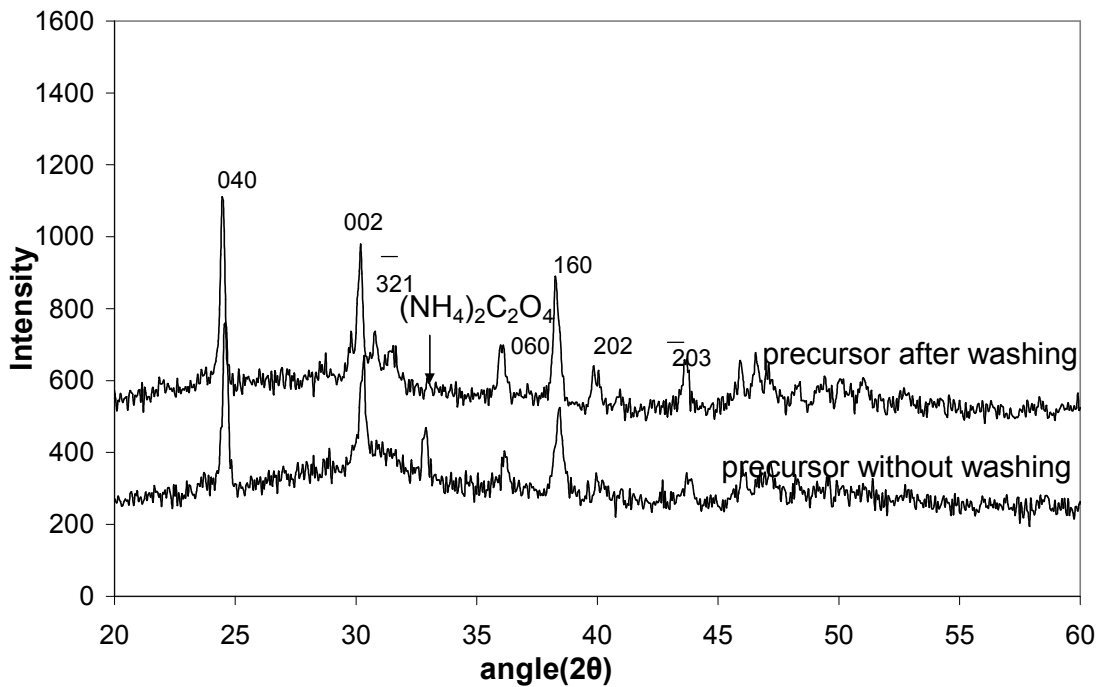


Figure 26 XRD pattern typical of precursor powders obtained from co-precipitation process with and without using washing as process step.

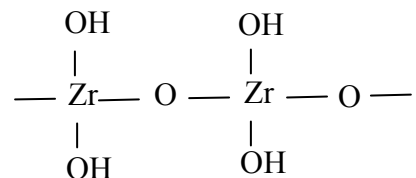
Wei et al.<sup>122</sup> and Le et al.<sup>123</sup> reported the presence of a  $\text{ZrC}_2\text{O}_4 \cdot \text{H}_2\text{O}$  phase in the precursor material based on XRD data. However, the XRD peaks shown by the authors are either very small or match closely with those of  $\text{CaC}_2\text{O}_4 \cdot \text{H}_2\text{O}$  (JCPDS#17-0541). Following the work of Le et al., van Rij et al.<sup>124</sup> conducted a more thorough investigation of this system and concluded that  $\text{CaC}_2\text{O}_4 \cdot \text{H}_2\text{O}$  was the only major crystalline phase present in the precursor powder.

Other researchers have used the co-precipitation technique to produce mixed oxalates of the form  $\text{CaZr}(\text{C}_2\text{O}_4)_3 \cdot \text{H}_2\text{O}$ <sup>125</sup> and  $\text{CaZrO}(\text{C}_2\text{O}_4)_2 \cdot x\text{H}_2\text{O}$ .<sup>126,127</sup> However, these studies did not involve structural characterization as the phase formula was

primarily derived from empirical calculations. Chapelet-Arab et al.<sup>128</sup> and Audebrand et al.<sup>129</sup> carried out systematic single crystal studies and pointed out that the oxalate formed must have a formula of  $\text{Ca}_2\text{Zr}(\text{C}_2\text{O}_4)_4 \cdot n\text{H}_2\text{O}$ .

Although different mixed oxalate precursors have been synthesized involving  $\text{Ca}^{2+}$  and  $\text{Zr}^{4+}$  cations, none have been shown to decompose directly to form the perovskite phase. While Saavedra et al.<sup>125</sup> report that single phase perovskite can be formed from their process, secondary (CaO) phases can be seen in their XRD results. A mixture of phases ( $\text{CaCO}_3$ ,  $\text{CaZrO}_3$  and CaO) is also seen after thermal decomposition of the compound synthesized by Chapelet-Arab et al.<sup>128</sup>

The precipitation of zirconium ( $\text{Zr}^{4+}$ ) has been discussed in detail by Baes and Mesmer<sup>130</sup> as well as Curtis and Degueldre.<sup>131</sup> Due to their high charge and small radius, zirconium ions have a high tendency to get hydrolyzed. At the precipitation conditions, the cation is supposed to be present in the polymer form,



which precipitates as  $\text{ZrO}(\text{OH})_2$  (zirconium oxyhydroxide).<sup>132</sup> This phase has a characteristic broad amorphous hump at  $\sim 30^\circ$  in the XRD spectra.<sup>133</sup> The XRD spectrum in Figure 26 contains a broad hump at  $\sim 30^\circ$  suggesting that zirconium could be present in the amorphous phase.

The solubility products in water for  $\text{CaC}_2\text{O}_4 \cdot \text{H}_2\text{O}$ <sup>134</sup>,  $\text{ZrO}(\text{OH})_2$ <sup>124</sup> and  $\text{In}(\text{OH})_3$ <sup>135</sup> are  $\sim 10^{-9}$ ,  $\sim 10^{-49}$  and  $\sim 10^{-34}$ , respectively. Since these values do not lie close to each

other, the simultaneous precipitation of the cations in the form of mixed oxalates is improbable.<sup>136</sup> Zirconium speciation specially is a complex process which depends on several irreversible reactions. A specific study investigating the problems associated with controlled zirconium precipitation using the oxalate technique was carried out by Kirby et al.<sup>137</sup> Nature of oxalate addition, oxalate concentration, and temperature were among the many parameters that were observed to affect Zr precipitation.

The oxalate and hydroxide species have very low solubilities at pH 9 and are expected to precipitate out completely. Figure 26 contains an additional XRD peak in the spectrum from powders prepared without using the elaborate washing procedure. The peak position matches with that of ammonium oxalate, which could have been formed during the precipitation reaction. Ammonium oxalate has been found to inhibit sintering in other oxide systems,<sup>138</sup> so careful washing of the powder is an important step in the precursor powder preparation.

Investigation of the powders using infra-red spectroscopy is useful to understand the nature of the bonds present in the oxalate precursor. Figure 27 shows peaks obtained from transmittance mode FTIR carried out on the precursor powder. The prominent features seen in the FTIR spectra are at 509, 655, 779, 1311 and 1603  $\text{cm}^{-1}$ , and a few small peaks are found at wave numbers greater than 3000  $\text{cm}^{-1}$ . The peaks found in the spectra match well with those seen by other researchers. Girija et al.<sup>139</sup> credit a peak at 1318  $\text{cm}^{-1}$  to stretching of the metal-carboxylate bond while a peak at 510  $\text{cm}^{-1}$  is said to be due to in-plane O-C-O bending. Ouyang et al.<sup>140</sup> and El-Shall et al.<sup>141</sup> assign a peak at 1620  $\text{cm}^{-1}$  to antisymmetric carbonyl stretching. Maurice-Esteva et al.<sup>142</sup> credit a band at 780  $\text{cm}^{-1}$  to out-of-plane bending of the water molecule, while antisymmetric and

symmetric stretches for coordinated water are said to cause small peaks above  $3000\text{ cm}^{-1}$ . The difference in the two spectra is seen by way of a small peak at  $2950\text{ cm}^{-1}$  in the sample prepared without the washing step. This position corresponds to a peak found in ammonium oxalate, consistent with the results discussed from the XRD shown in Figure 26.

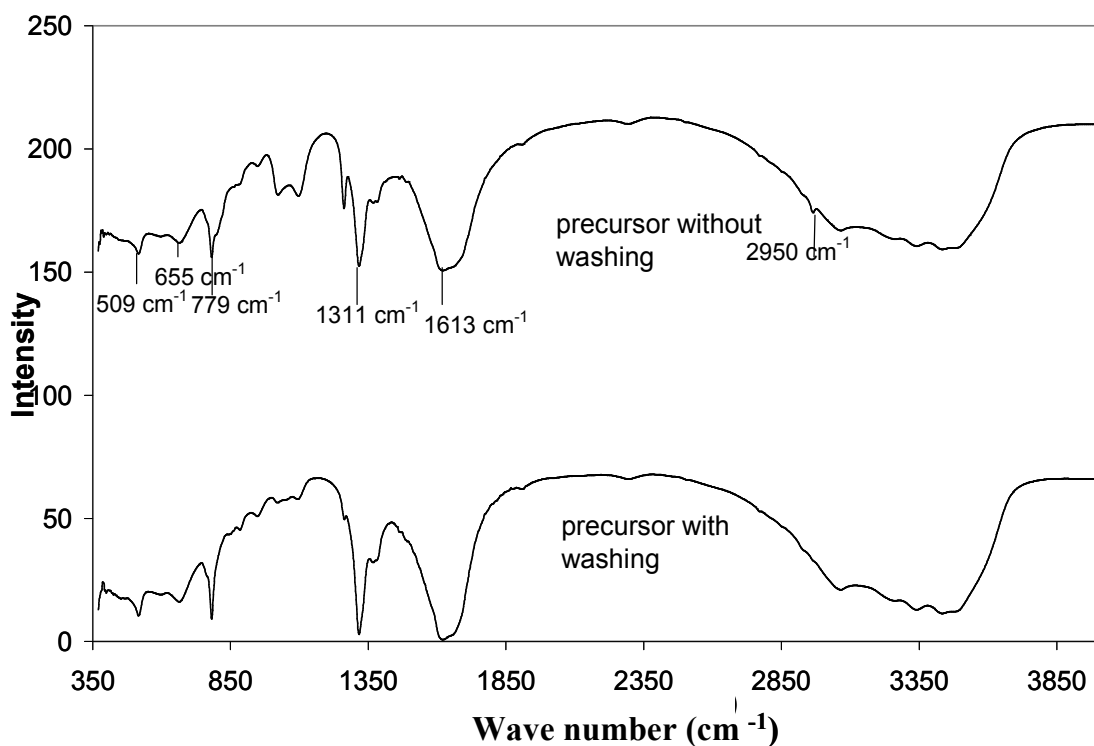


Figure 27 FTIR spectra obtained from precursor powders prepared with and without using the washing step

#### 5.1.2.2 Oxalate decomposition

The oxalate precursor powders were heated at various temperatures to produce the perovskite material. XRD was used to investigate the formation of various phases during

oxalate decomposition. Diffraction peaks seen in the different powders are shown in Figure 28.

After heating at 530°C for 3 hours, the calcium oxalate species was found to have decomposed and formed the calcium carbonate phase. This could have been achieved by the loss of CO<sub>2</sub> species during the heat treatment. 2 broad humps at 30° and 50° are also seen indicating the presence of Zr in the form of an amorphous zirconia.<sup>143</sup> Further heating to 830°C formed the CaZr<sub>4</sub>O<sub>9</sub> phase along with CaO. Presence of the perovskite CaZrO<sub>3</sub> was also seen in this diffraction pattern. Powder calcinations at 1200°C formed the perovskite phase with small amounts of CaO and CaIn<sub>2</sub>O<sub>4</sub>. The appearance and disappearance of these phases were found to be consistent with data published by Le et al.<sup>123</sup>

Figure 28 shows disappearance of the CaIn<sub>2</sub>O<sub>4</sub> peaks after calcinations at 1400°C for 12 hours. This is in contrast to results from solid oxide synthesis (Figure 25) where the In-rich CaIn<sub>2</sub>O<sub>4</sub> phase was found even after heating the sample at similar conditions. Electron X-ray Dispersive Spectroscopy (EDS) analysis of the powders showed presence of all the three cations with proportions matching the desired stoichiometry. The oxalate co-precipitation technique thus seems to be a suitable synthesis method as both an absence of prominent secondary phases as well as good control over stoichiometry was achieved.

Further analysis of the disappearance of the CaIn<sub>2</sub>O<sub>4</sub> peak (Figure 28) was carried out using XRD. The patterns obtained from powders calcined at 1000°C, 1200°C and 1400°C are shown in Figure 29.

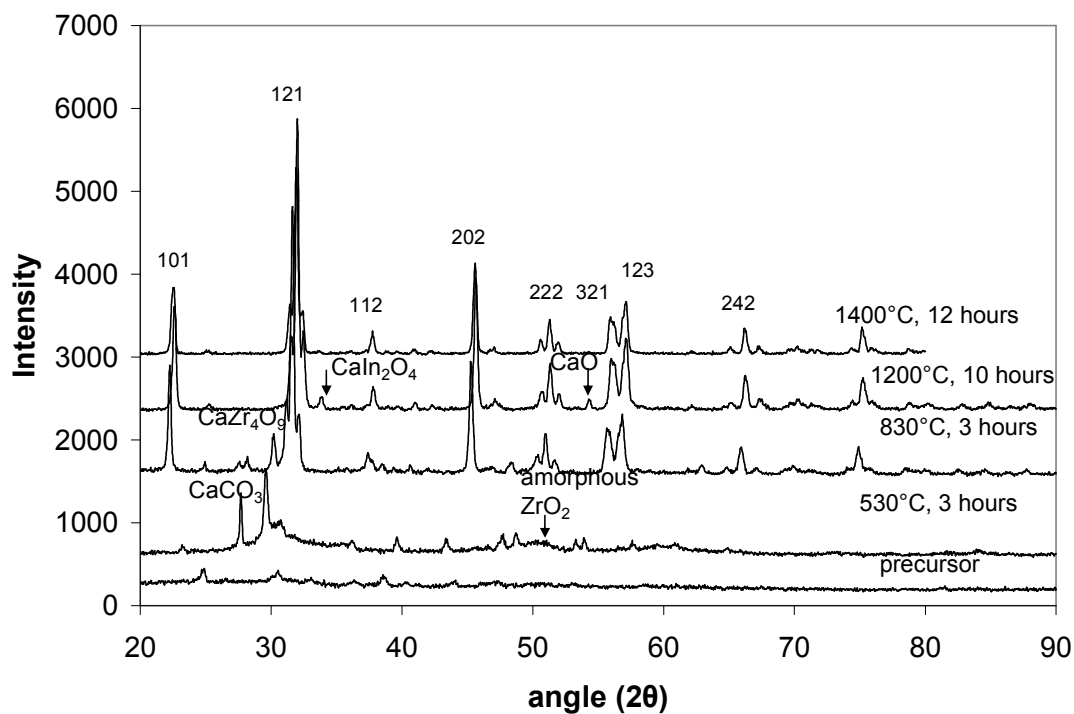


Figure 28 Phases formed during perovskite formation from precursor decomposition

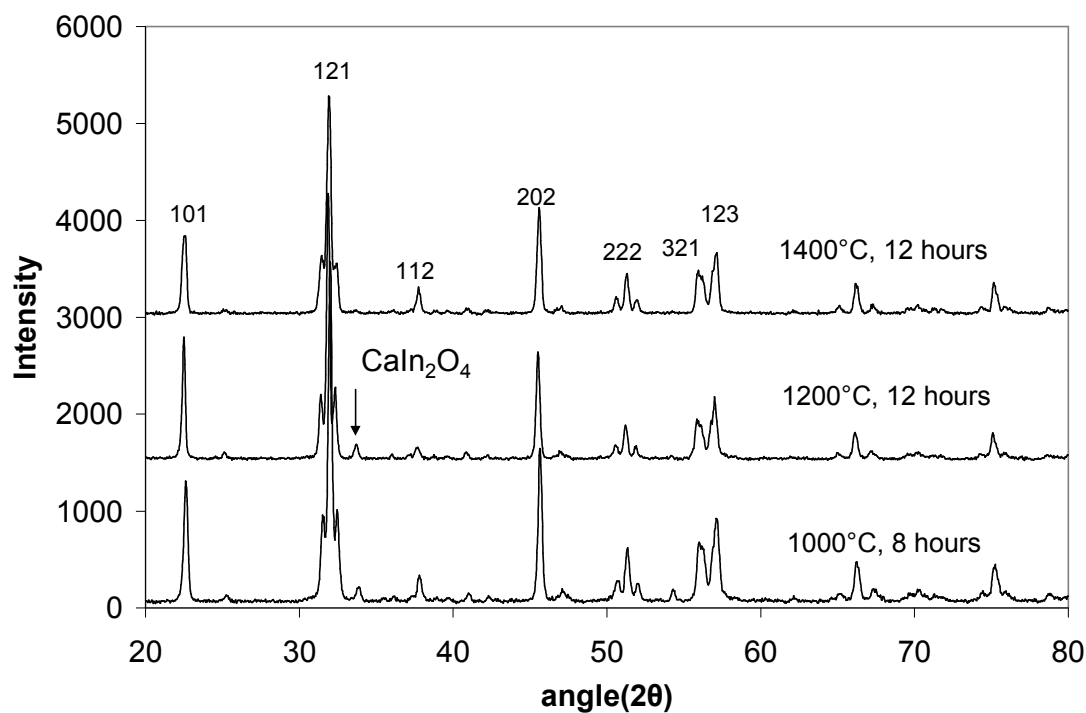


Figure 29 Disappearance of In-rich secondary phase  $\text{CaIn}_2\text{O}_4$  at high temperatures



The amount of  $\text{CaIn}_2\text{O}_4$  decreased with thermal treatment as shown in Figure 30 using the ratio of integrated peak intensities of  $\text{CaIn}_2\text{O}_4$  peak at  $33.4^\circ$  and (121)  $\text{CaZrO}_3$  peak at  $22.35^\circ$ . The  $\text{CaIn}_2\text{O}_4$  peaks decrease more rapidly in samples calcined at  $1400^\circ\text{C}$  as compared to samples calcined at  $1200^\circ\text{C}$ .

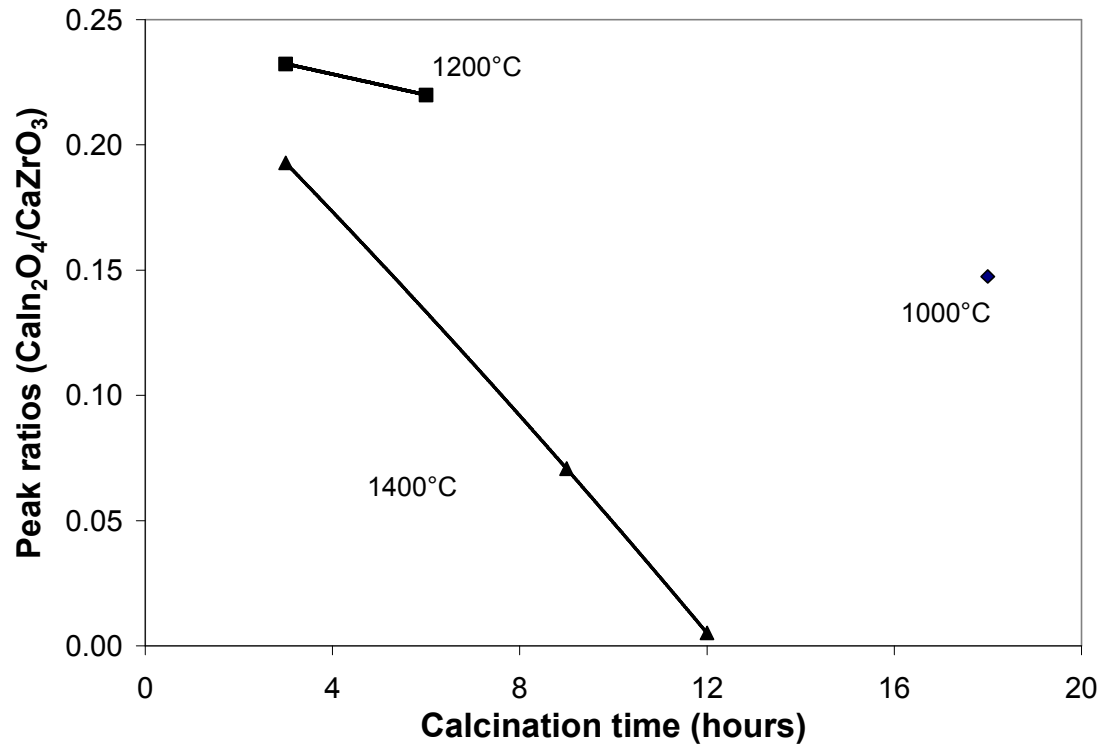


Figure 30 Disappearance of the In-rich peak in  $\text{CaZr}_{0.9}\text{In}_{0.1}\text{O}_{2.95}$  shown by a decrease in peak ratios.

Indium ( $\text{In}^{3+}$ ) is present in the  $\text{CaZrO}_3$  lattice as a substitutional dopant on the B site. Due to differences in cation sizes and charge, a certain concentration limit exists below which the perovskite lattice is able to dissolve the dopant in its structure. Presence of the dopant in amounts larger than this solubility limit causes precipitation of an In-rich secondary phase ( $\text{CaIn}_2\text{O}_4$ ) which could affect the electrical properties of the material.

Since the formation of the  $\text{CaIn}_2\text{O}_4$  phase depends on the total indium concentration, it is useful to monitor its presence by preparing samples with varying dopant content.

Figure 31 shows XRD patterns from  $\text{CaZrO}_3$  powders with various indium concentrations using the coprecipitation technique. All the powders prepared were calcined at  $1400^\circ\text{C}$  for 12 hours. XRD peaks from pure  $\text{CaZrO}_3$  powder obtained from Aldrich are added for comparison. While all the major peaks present could be ascribed to the perovskite phase, presence of the  $\text{CaIn}_2\text{O}_4$  phase was clearly seen in samples with  $x > 0.15$ .

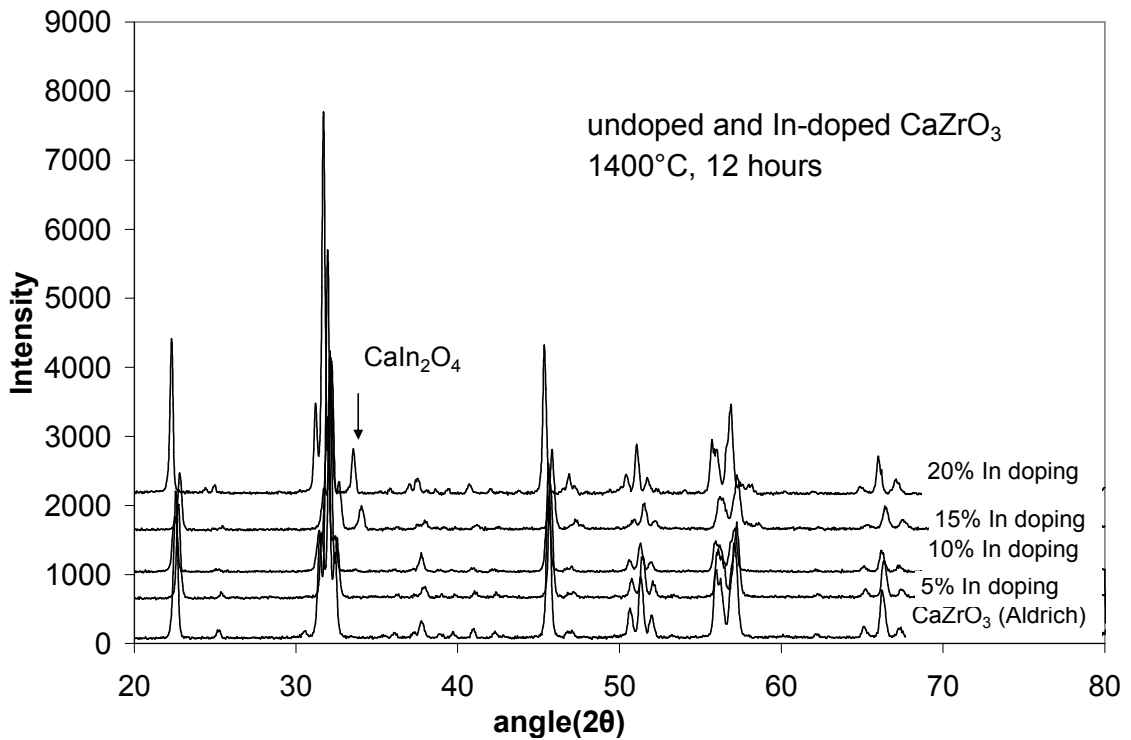


Figure 31 Formation of In-rich  $\text{CaIn}_2\text{O}_4$  phase due to increased indium content in the perovskite powder.

The lack of a prominent peak in the XRD data does not necessarily mean absence of the phase. Peak ratios and d-spacing calculations were used to better estimate the

concentration at which the secondary phase formed. A plot of the peak ratios for powders with varying indium concentrations is shown in Figure 32. These were calculated by dividing the integrated intensity of the secondary peak by the integrated intensity of the  $\text{CaZrO}_3$  (121) peak. The ratios seem to increase in higher indium concentrations, and also suggest the presence of the secondary phase at indium levels greater than 5%. This is comparable with the 4 mol% solubility reported by Kobayashi et al.<sup>144</sup> The authors base their argument on findings by Iwahara,<sup>101</sup> who reported incidence of the  $\text{CaIn}_2\text{O}_4$  peak in sintered samples of 5 mol% In-doped  $\text{CaZrO}_3$ .

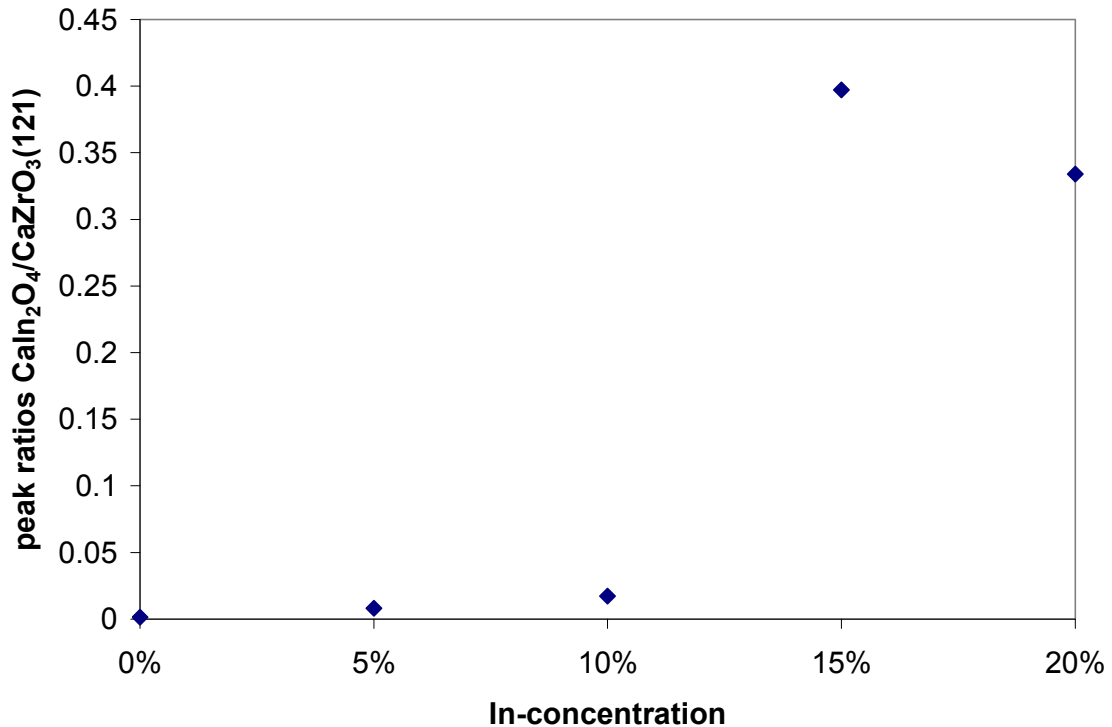


Figure 32 Increase in peak ratios of integrated intensities in  $\text{CaZrO}_3$  powders with varying In contents.

XRD results from samples with varying indium concentrations were used to calculate variations in the lattice parameters with doping. Cohen's method was used to

arrive at lattice parameter values which were well comparable to those listed in the JCPDS card. The variation in the cell volume ( $V$ ) calculated from the individual lattice parameters is shown in Figure 33. Although the data shows considerable scatter, the plot clearly indicates an initial increase in cell volume on indium doping suggesting that solubility of indium in these samples is between 0 and 5%.

Although further in-depth analysis is required to accurately determine the true solubility limit, the XRD data helps in making a rough estimate. It is also important to recognize the importance of samples attaining equilibrium, as it might take several days of heating to dissolve the dopant completely.

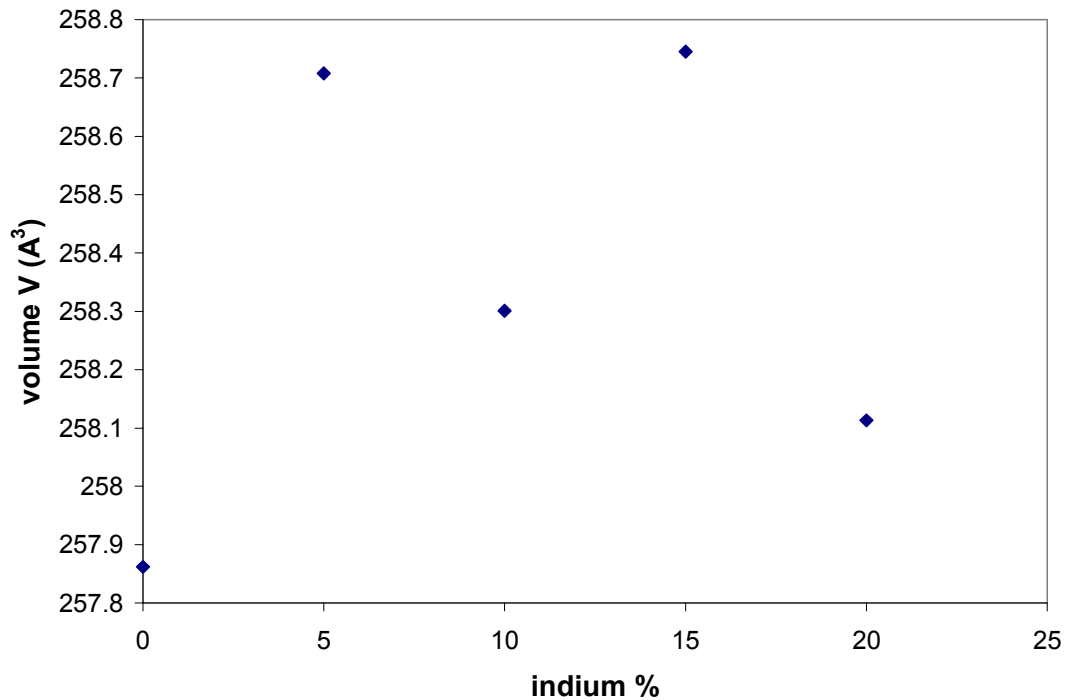


Figure 33 Variation of cell volume ( $V$ ) with increasing indium concentration in  $\text{CaZrO}_3$ .

Mg-doped  $\text{CaZrO}_3$  were also produced using the oxalate coprecipitation technique. XRD data from precursors decomposed at different calcinations conditions are shown in Figure 34. While the ordered phase  $\text{CaZr}_4\text{O}_9$  ( $\phi 1$ ) was visible in powders decomposed at  $800^\circ\text{C}$ , calcinations at higher temperatures ( $1000^\circ\text{C}$ ,  $1200^\circ\text{C}$ ) fully formed the perovskite material. All the peaks obtained from 10 mol% Mg-doped  $\text{CaZrO}_3$  powders were attributed to the perovskite phase and appropriately indexed. No extra peaks were seen in the XRD profile which suggests the absence of any prominent secondary phases.

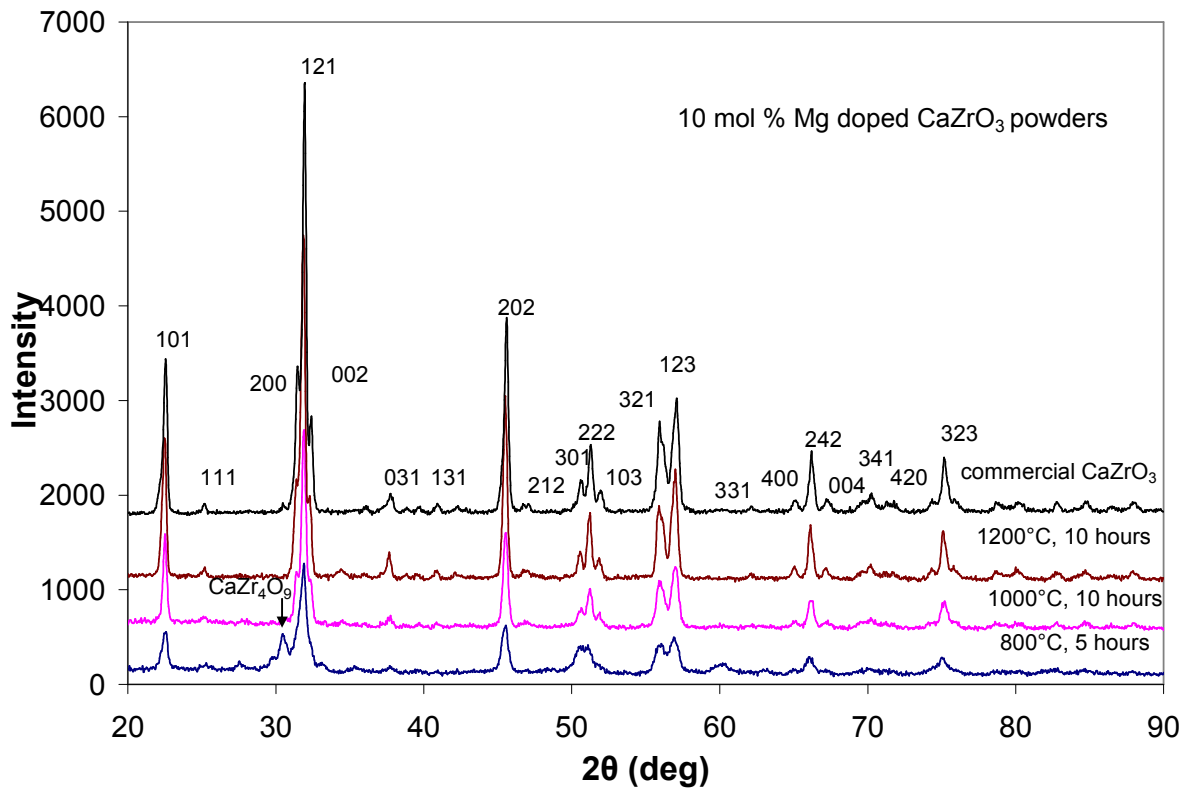


Figure 34 Mg-doped  $\text{CaZrO}_3$  powders obtained from oxalate precursor decomposition

#### 5.1.2.3 Effect of dispersant addition

An improvement to the co-precipitation process was attempted by adding dispersants to the liquid phase synthesis. Addition of organic surfactants like

PolyEthylene Glycol (PEG), to the liquid mix process could lead to reduced particle size either by inhibiting agglomeration or by causing deagglomeration of secondary particles formed earlier in the process.

The first mechanism explains particle size reduction based on PEG's ability to prevent agglomeration.<sup>145</sup> Since PEG is a non-ionic polymer, it consists of neutral hydrophobic and hydrophilic parts. The O-H bonds are, however, polar and should form linkages within the system by hydrogen bonding. According to Ece et al.<sup>146</sup>, the interfacial energy at the particle/liquid interface is reduced because of these surface linkages as the adsorbed polymer produces repulsive forces between the suspended particles. Steric stabilization of the dispersion results in limited particle-particle interactions and reduced agglomeration. A schematic of particles separated by PEG molecules is shown in Figure 35.

Uhland et al.<sup>147</sup> propose a different mechanism in which PEG is said to promote deagglomeration and redispersion of particles. According to this model, osmotic pressure is created due to a change in the chemical potential of the solvent within and outside the agglomerate. Since the osmotic pressure is inversely related to the molecular weight of the polymer, a lower molecular weight PEG should be more effective in breaking down larger agglomerates. SEM micrographs of Fe-Ni double oxalates shown by Uekawa et al.<sup>148</sup> confirm that particle size increases with increasing molecular weight of PEG.

SEM micrographs of the powders synthesized in this work are shown in Figure 36 and Figure 37. Figure 37 shows the considerable agglomeration in powders prepared using without PEG, while better-dispersed, finer powders are present in the case of PEG

addition (Figure 36). This confirms the theory that addition of PEG helps in the formation of powders with reduced particle size and agglomeration.

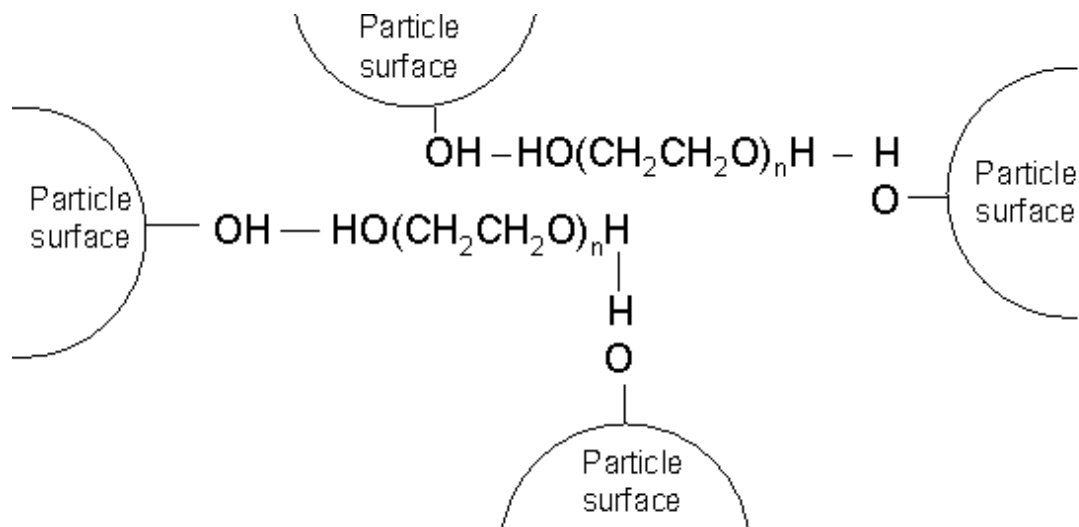


Figure 35 Schematic of surfactant PEG preventing particle agglomeration by limiting particle-particle interactions.

The particle size distribution was characterized using the laser scattering technique, results from which are shown in Figure 38 and Figure 39. The addition of PEG had an effect on the distribution. Powders synthesized without PEG consist mainly of larger particles with a relatively narrow distribution. Addition of the surfactant however, results in a wider distribution with an increase in the amount of smaller agglomerates.

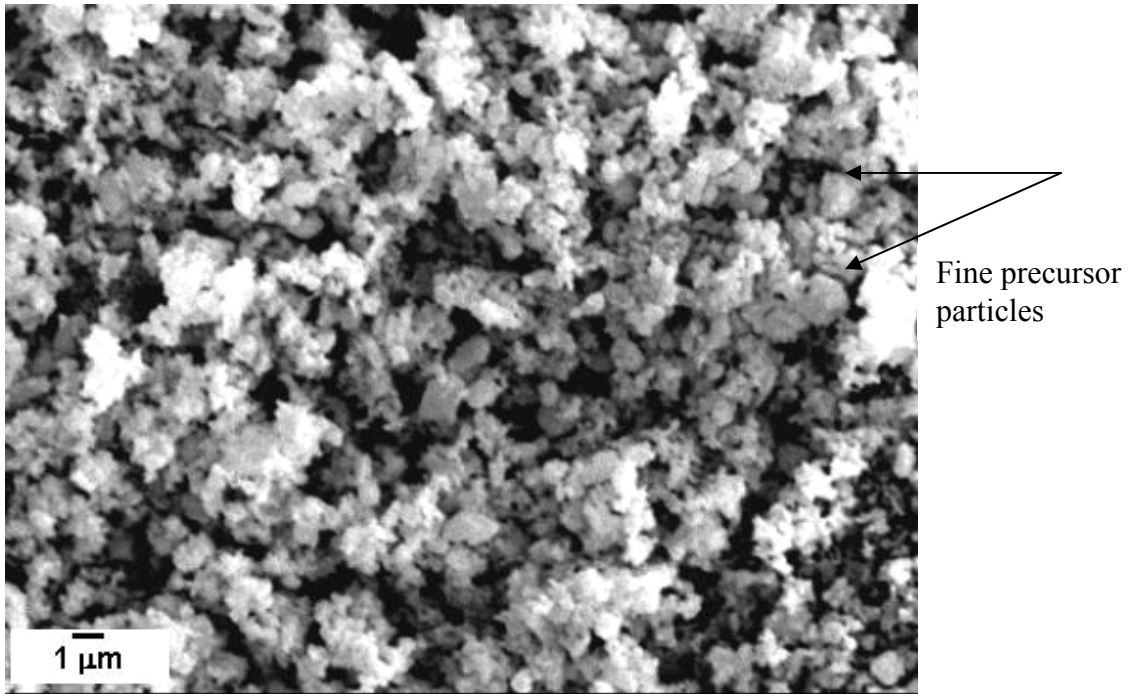


Figure 36 SEM image of precursor particles synthesized using PEG as a surfactant.

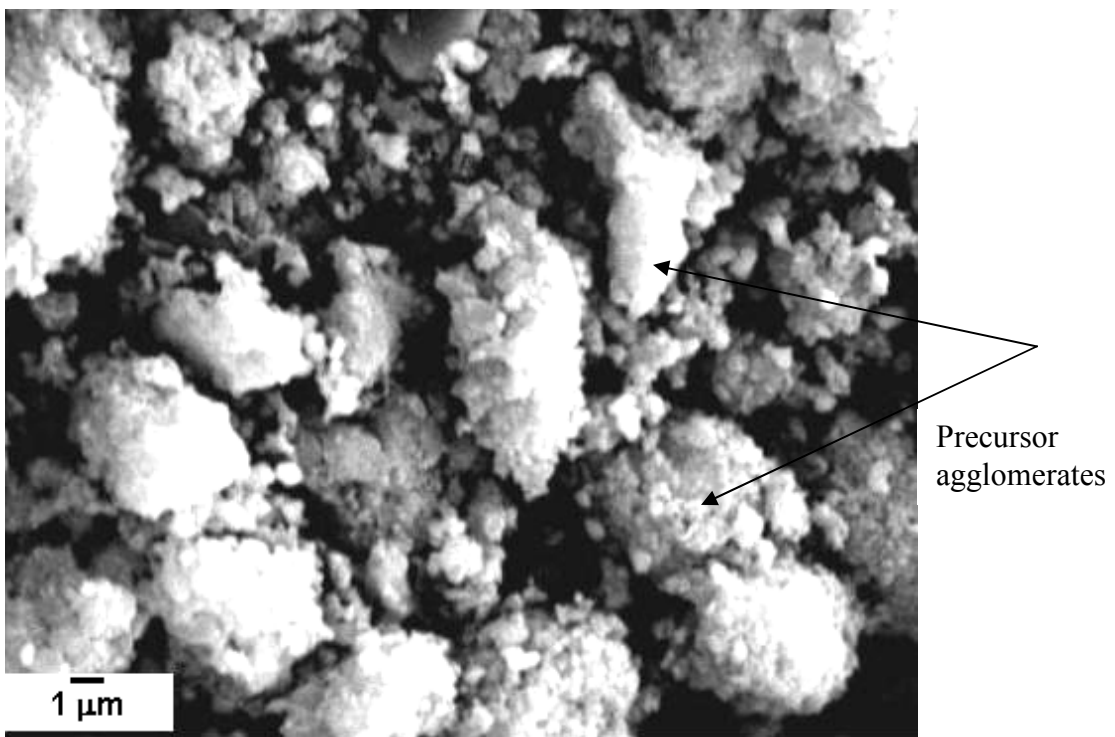


Figure 37 SEM image of precursor particles synthesized without use of PEG.



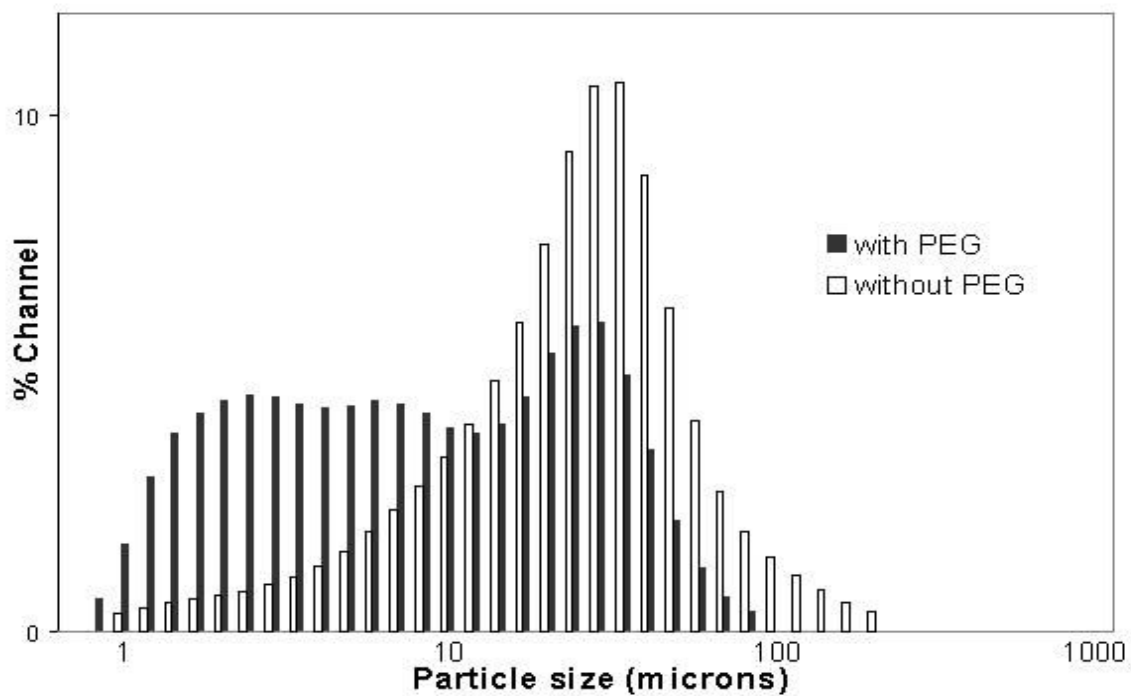


Figure 38 Effect of PEG addition on particle size distribution of precursor powders.

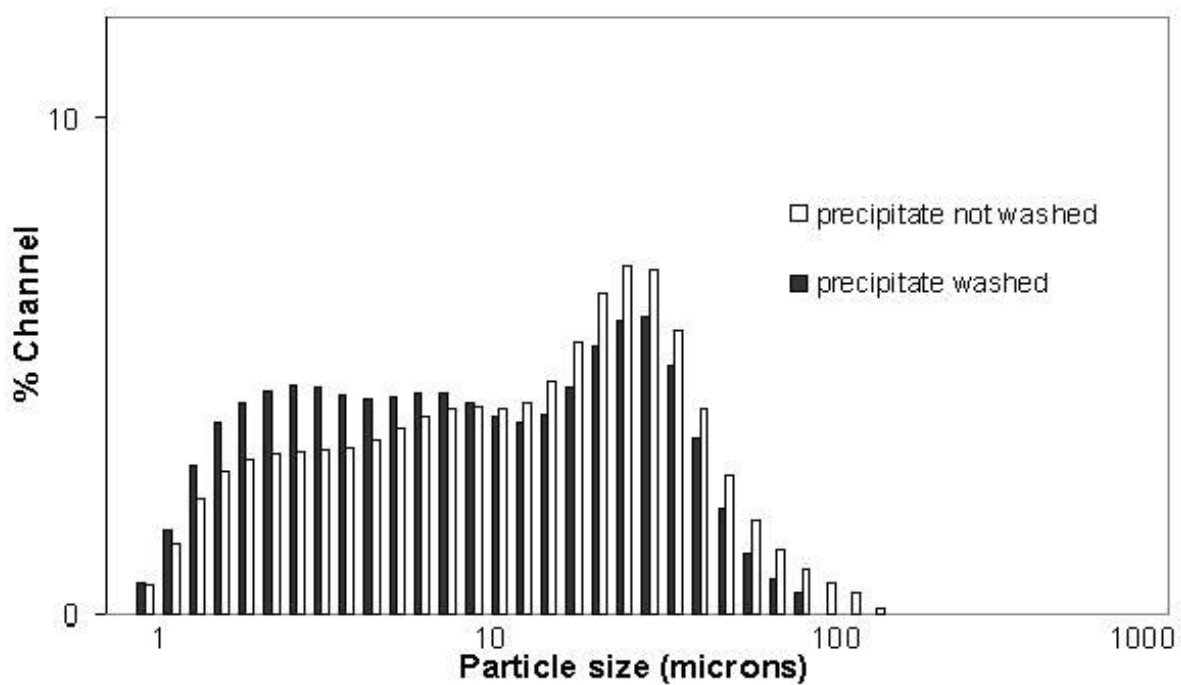


Figure 39 Effect of precipitate washing on particle size distribution of precursor powders.

Washing of the precursor powders with ethanol and water affects the particle size distribution. Although the distribution does not change as much as for PEG addition, smaller particles are formed with washing. According to Kaliszewski and Heuer<sup>149</sup>, the ethanol treatment aids in the formation of surface ethoxide groups, which inhibits growth of inter-particle bridges by displacing adsorbed water that causes hydrogen bonding between the polar water molecules. The reduced number of inter-particle bridges could produce weaker agglomerates which would explain the smaller particles.

Addition of the surfactant was also seen to affect particle settling. A plot of the particle level height against settling time is shown in Figure 40. Powders prepared using PEG are smaller and appear to be less agglomerated. These should be less heavy than particles formed in the absence of the surfactant, and therefore settle down more slowly. The slow settling results in the minimal drop in the height of the particle column when compared to powders prepared without PEG addition.

Figure 41 shows XRD plots from perovskite powders produced using the surfactant along with powders produced without the PEG addition process. The addition of surfactant was found to improve the kinetics of perovskite formation as shown in the XRD of precursors decomposed at 850°C. XRD spectra of powders prepared without PEG contain a large peak matching with the Zr-rich  $\phi_1$  phase ( $\text{CaZr}_4\text{O}_9$ ) and several other unidentified peaks (marked with #), while powders prepared using PEG addition as a process step contain peaks only from  $\text{CaZrO}_3$ . This result is somewhat explained by the previous particle size, shape and distribution analyses where PEG was seen to help reduce the size and agglomerative nature of the precursor particles.

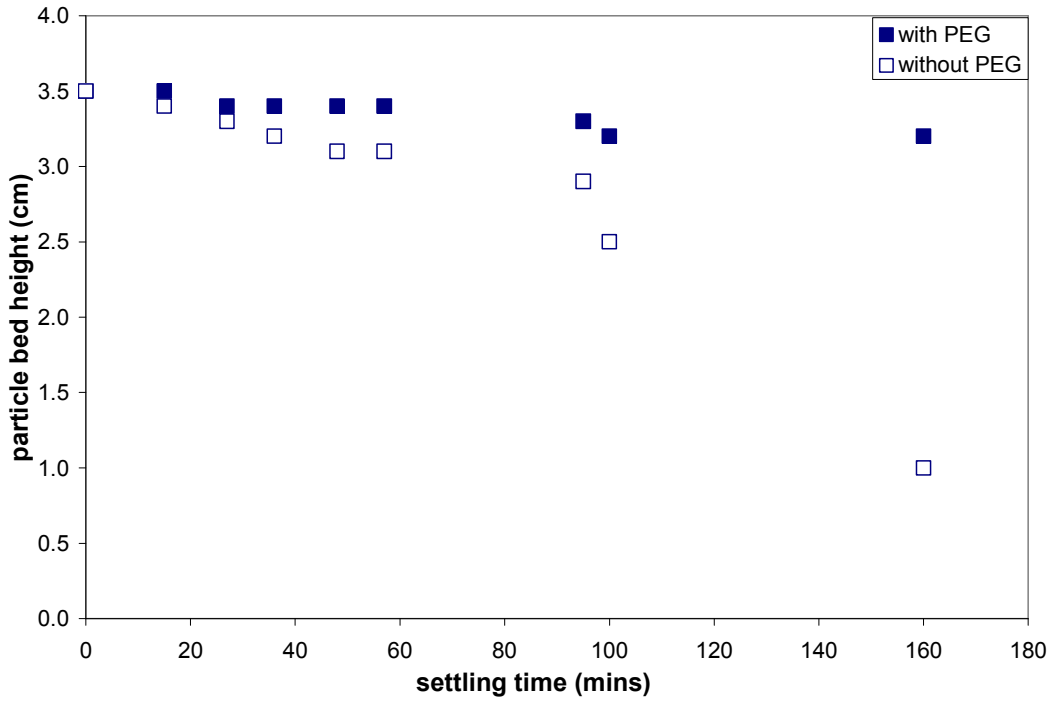


Figure 40 Influence of PEG on particle settling. Powders prepared using PEG settled down slower than those prepared without PEG indicating smaller sizes.

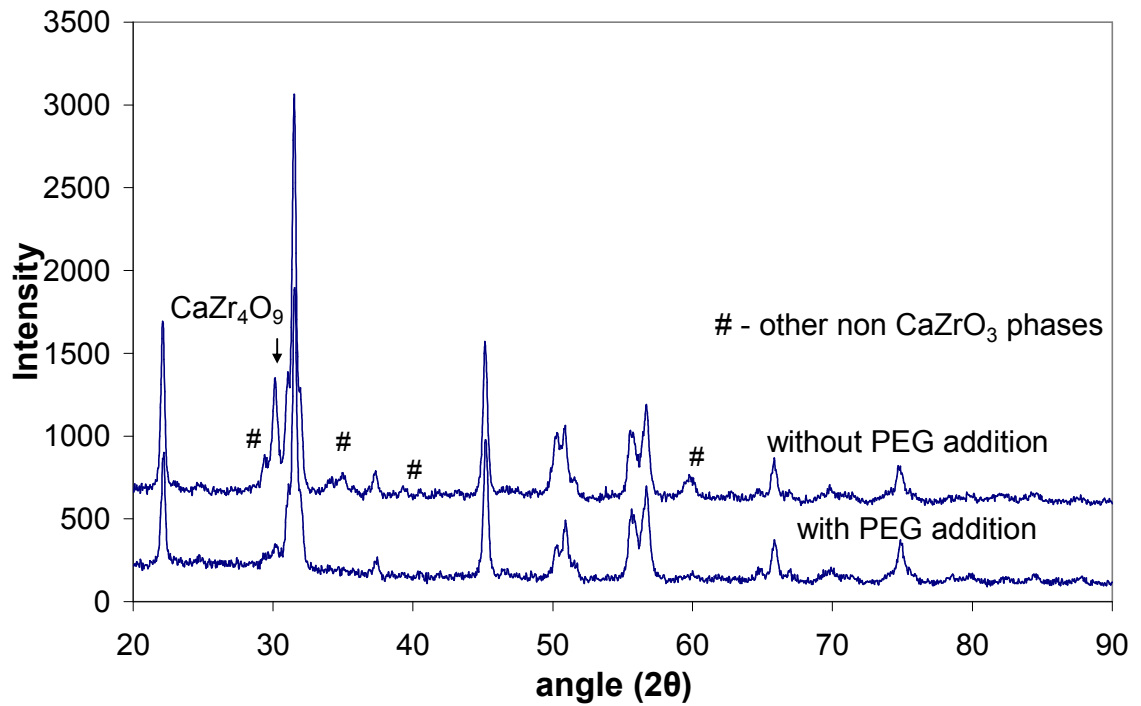


Figure 41 Effect of PEG addition on perovskite formation from precursor powders.

If faster kinetics in the case of PEG assisted precursor particles were to be attributed to smaller particles, particle size reduction by mechanical means should also bring about similar results. To test this hypothesis, the precursor particles were broken down further by ball-milling. Figure 42 shows perovskite formation from the decomposition of precursor powders which were milled for 2 days. XRD peaks from powders that were directly calcined without milling are also shown for comparison. The milled powders can be seen to form the  $\text{CaZrO}_3$  perovskite after calcinations at  $900^\circ\text{C}$  while additional secondary phases ( $\text{CaZr}_4\text{O}_9$ ,  $\text{CaO}$ , and  $\text{CaCO}_3$ ) are still found in the powders that were directly calcined at the same temperature. Some additional peaks are even present in the unmilled powders after calcining at a higher temperature of  $1200^\circ\text{C}$ .

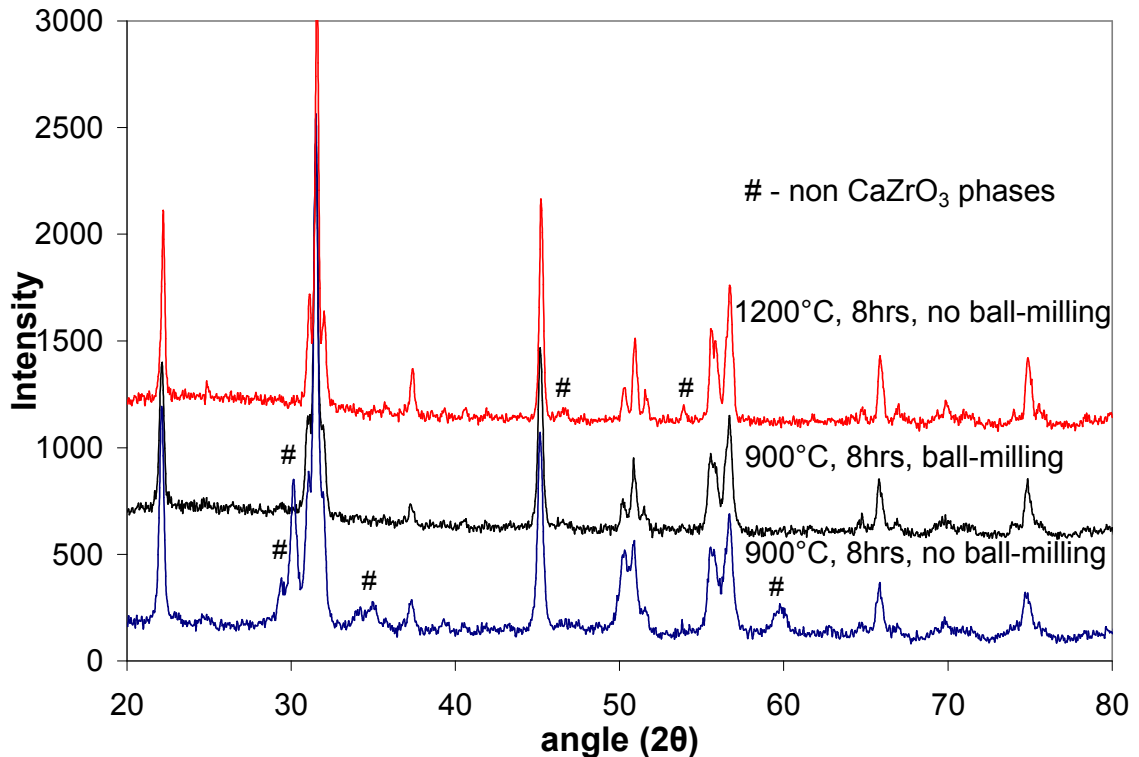


Figure 42 Effect of ball-milling on perovskite formation from precursor powders.

prepared without PEG.

The XRD plots Figure 41 and Figure 42 show that precursor powders that were either ball-milled or prepared using PEG result in the formation of  $\text{CaZrO}_3$  without any secondary phases. The consequence of ball-milling precursor powders prepared using PEG is however not clear. To investigate this effect, precursor powders were ball-milled for 2 days after being prepared using PEG. XRD peaks obtained from the decomposition of the milled powders at  $800^\circ\text{C}$  and  $950^\circ\text{C}$  are shown in Figure 43.

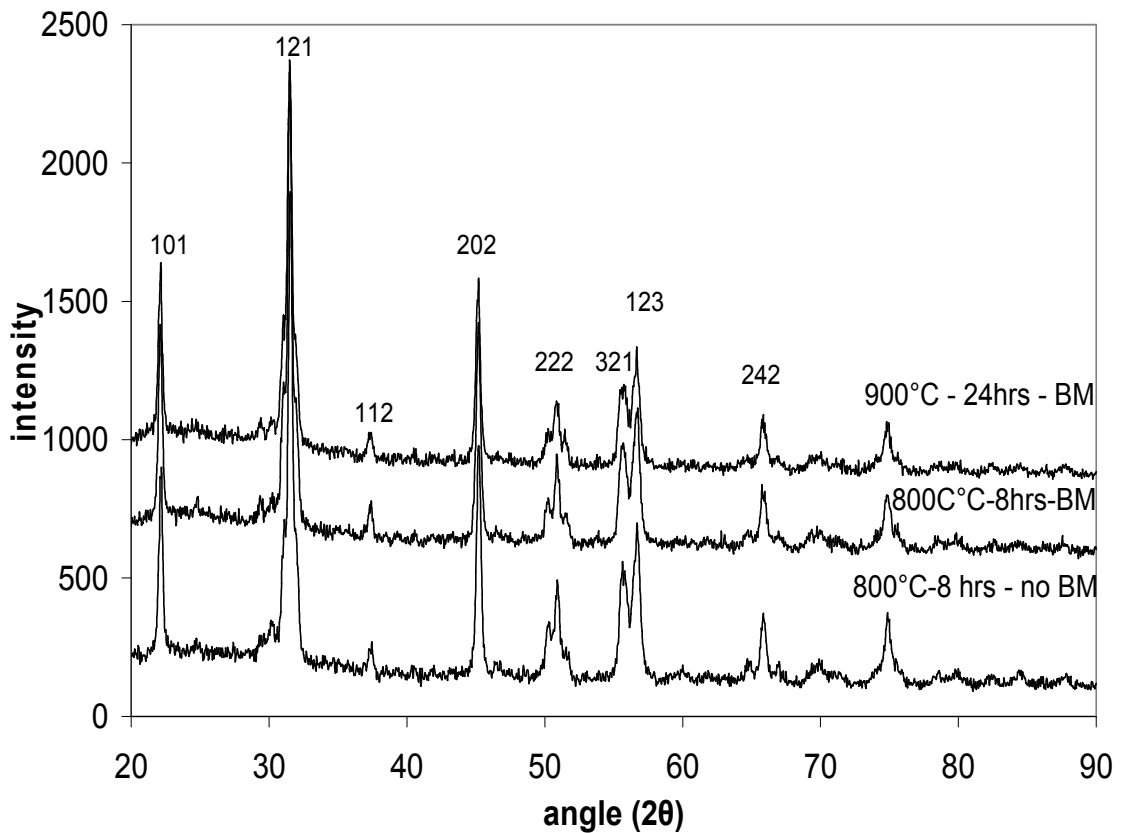


Figure 43 Effect of ball-milling on perovskite formation from precursor powders prepared using PEG.

The XRD results appear very similar to those from unmilled precursor powders that were prepared using PEG and decomposed at 800°C. Since no additional phases are seen the perovskite powders prepared using PEG seem to remain unaffected by the ball-milling step. Thus by adding PEG during the co-precipitation process, the energy and time intensive milling procedure could be avoided.

## **5.2 Electrical characterization of the solid electrolyte material**

For application as a solid electrolyte, electrical properties of the material are crucial. Since the defect properties of an ionic conductor might change according to the conditions, elaborate electrical characterization of the material under different environments is important to determine its applicability. The electrical properties of In-doped CaZrO<sub>3</sub> were measured by carrying out high temperature D.C. and A.C. resistance measurements across the sample pellet that was suspended in a furnace. Platinum electrodes applied on the faces of the pellet for electrical contact are shown in Figure 44 and Figure 45. The highly conductive pellet face ( $R < 1$  ohm across diameter of the pellet) was found to be porous and connected. Since reactions usually occur at triple phase boundaries (electrode-electrolyte-gas), the porous electrodes should improve electrochemical interactions.

### **5.2.1 Solid electrolyte characterization using impedance spectroscopy**

The electrical properties of In-doped CaZrO<sub>3</sub> were investigated using impedance spectroscopy. The spectrum in Figure 46 shows impedance data measured from a CaZr<sub>0.9</sub>In<sub>0.1</sub>O<sub>3-x/2</sub> pellet at 870°C. Impedance is a reactive form of the resistance and has

both resistive and capacitive elements. Real and imaginary parts of the impedance ( $Z'$  and  $Z''$ ) plotted against each other are shown in the Nyquist plot, while the frequency dependent Bode representations are shown in Figure 47 and Figure 48.

The Nyquist plot shows two semicircular relaxations seen at different frequency regions. These semicircles were attributed to bulk and grain boundary contributions and modeled using a circuit comprising of 2 R-CPE (R-resistance, CPE-constant phase element) units in series, with a series resistance ( $R_c$ ) for contact. Such circuits, also called as brick layer models (BLM), are common in the modeling of electrochemical impedance data from polycrystalline materials.<sup>150</sup> Fit results achieved using this 2 layer BLM model are shown as trend lines in each of the impedance plots. Table 3 shows the equivalent circuit model used along with the individual parameters that were extracted from the data fit.

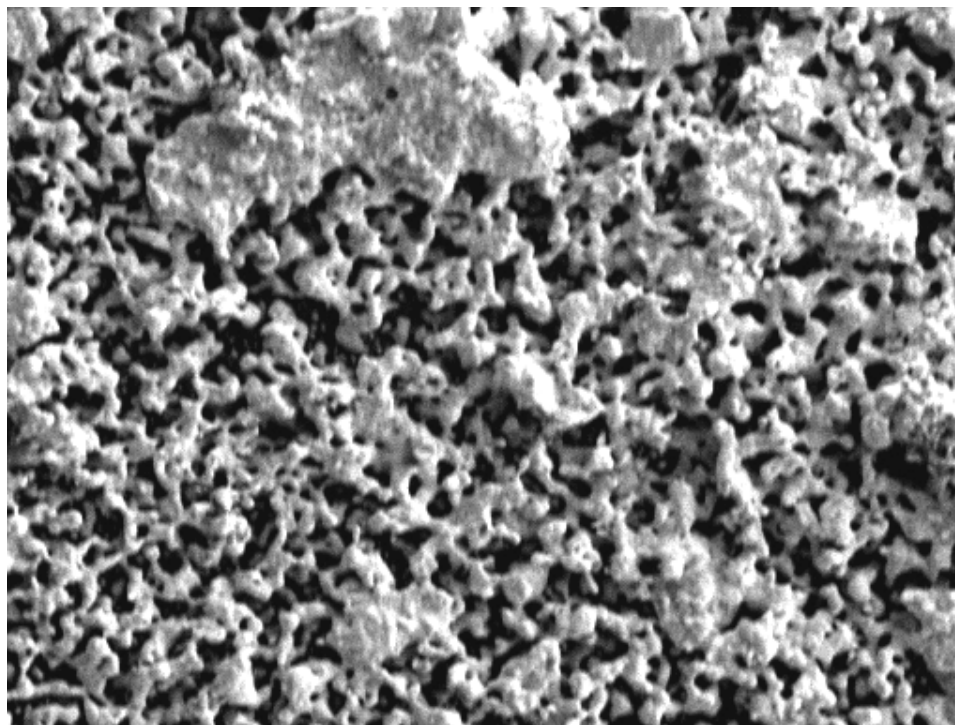


Figure 44 Pellet surface with porous Pt electrodes at 1000x.

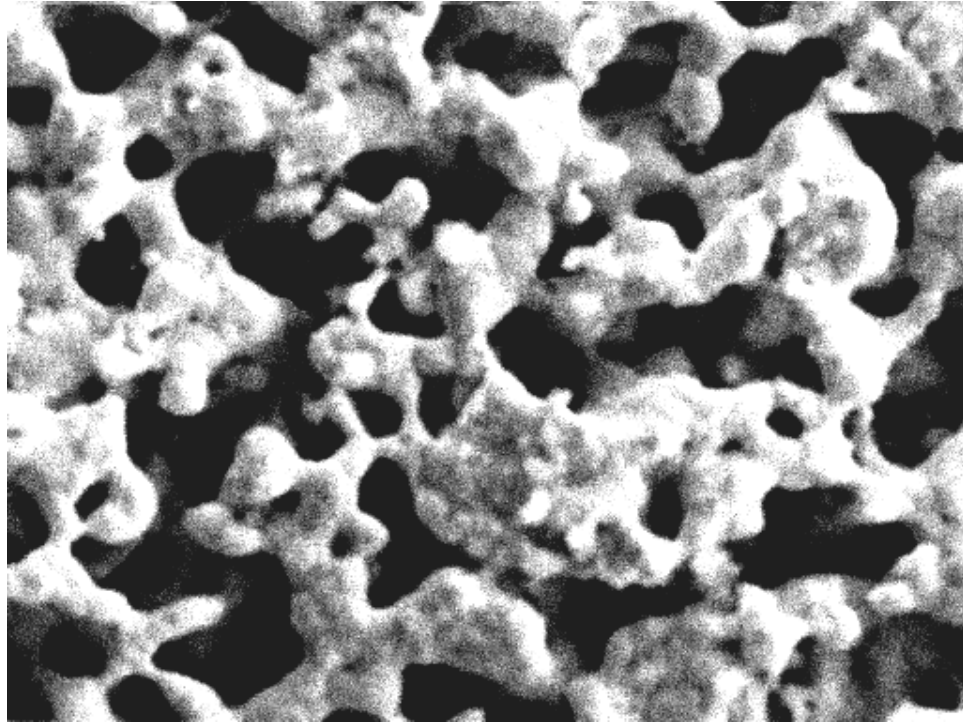


Figure 45 Highly networked Pt electrode on  $\text{CaZrO}_3$  pellet at 3500x.

The capacitance values  $C_1$  and  $C_2$  obtained for the 2 semicircles are  $3.2 \times 10^{-10}$  F and  $1.2 \times 10^{-6}$  F, respectively. As expected, the low frequency capacitance (grain boundary) is much higher than that of the high frequency semicircle (bulk). Grain boundaries normally act as sinks for impurities, which increases their capacitance. This results in a large value of the time constant ( $\tau = RC$ ), thus shifting the semicircle to lower frequencies. Schematic of a polycrystalline ceramic microstructure shown in Figure 49 containing randomly oriented individual grains separated by grain boundaries.



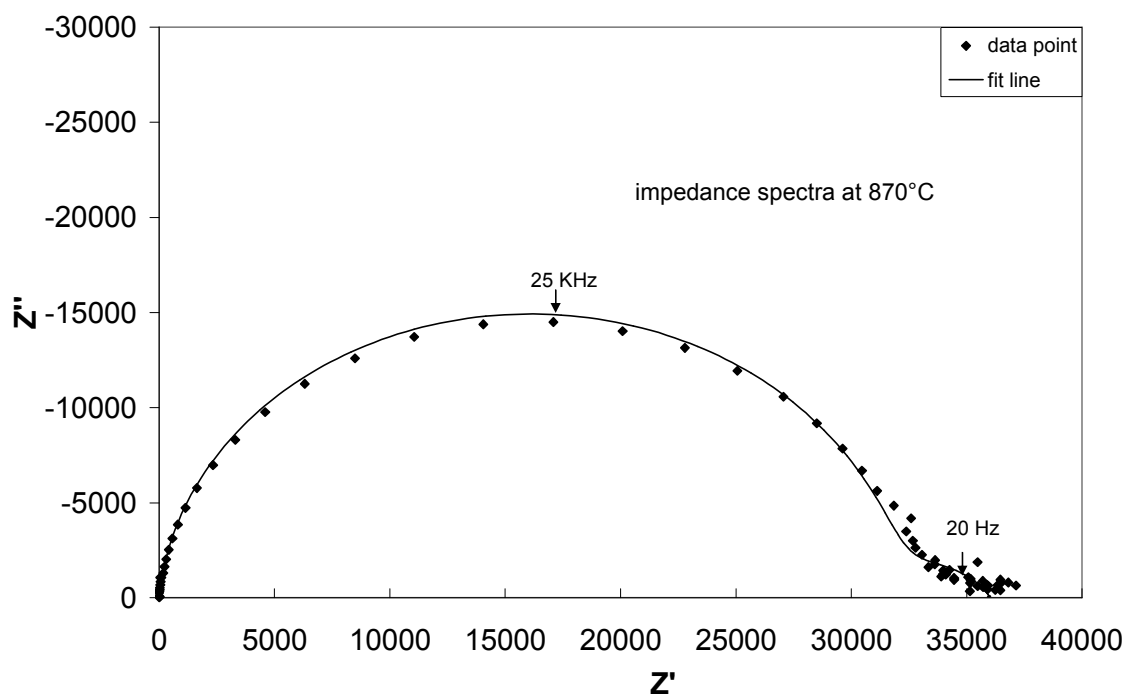


Figure 46 Nyquist plot of impedance measured from  $\text{CaZr}_{0.9}\text{In}_{0.1}\text{O}_{3-\alpha}$  pellet at 870°C.

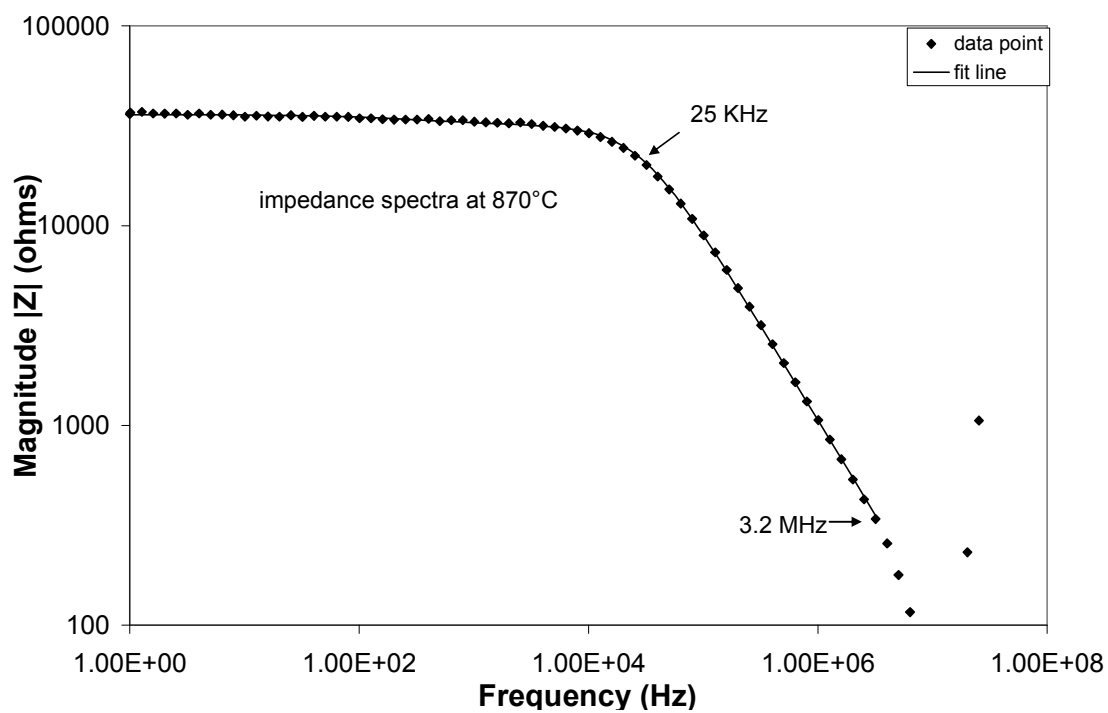


Figure 47 Bode plot showing dependence of impedance magnitude on frequency.

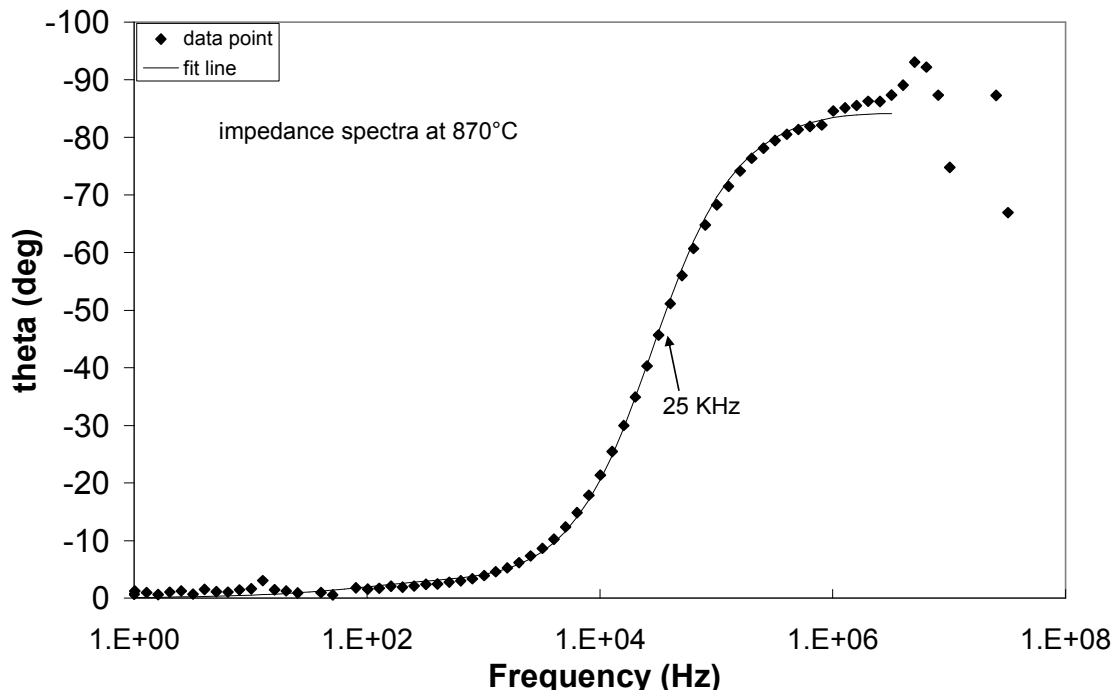
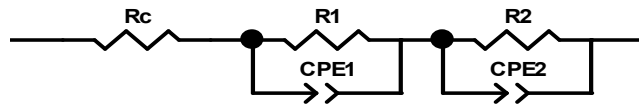


Figure 48 Bode representation showing variation of phase lag ( $\theta$ ) with frequency.



Element	Value	Error %
Rc (ohms)	4.2	N/A
R1 (ohms)	31783	1.19
CPE1-T (F)	3.12E-10	4.42
CPE1-P	0.95	0.37
R2 (ohms)	4236	11.02
CPE2-T (F)	1.19E-06	47.6
CPE2-P	0.69	11.7

Table 3 Two layer brick layer model along with values of circuit parameters extracted from relaxations observed at 870°C.

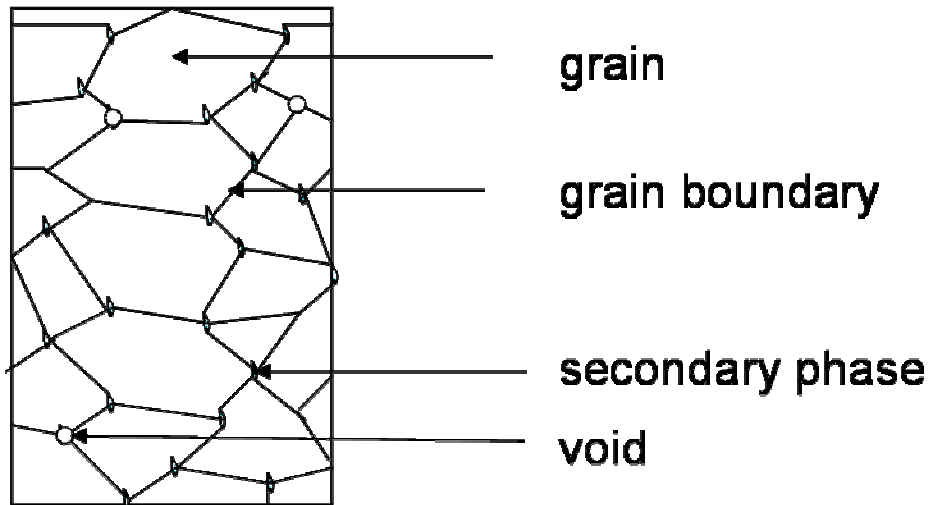


Figure 49 Schematic showing a polycrystalline pellet across which A.C and D.C resistance is measured.

As described earlier, semicircular relaxations seen in the impedance spectrum were modeled using the equivalent circuit shown. The model used a series resistance,  $R_s$  to represent the contact resistance of the lead wires, while  $R_1$  and  $R_2$  were attributed to the grain and grain boundary resistance contributions. Constant phase elements (CPE1 and CPE2) were used to model the individual capacitive contributions. This distributed element is defined by 2 values CPE-T and CPE-P, where impedance  $Z$  is given by  $Z_{CPE} = A(j\omega)^{1-n}$ .

The term CPE-T gives the capacitance of the element, whereas CPE-P (empirical factor,  $n$ ) accounts for depressed nature of the semicircles. A value of 1 for  $n$  indicates pure capacitance, while any heterogeneity in the material lowers  $n$ . The values of CPE1-P represent the level of homogeneity in the current paths. Conduction through the bulk appears to be highly homogenous since values of CPE1-P are close to 1, which is

indicative of an ideal Debye-like relaxation. Grain boundaries, on the other hand, usually act as sinks for impurities which make the conduction process heterogeneous. This is evident from the values of CPE2-P which are much lower than the ideal value of 1.

The circuit model proposed represents the impedance data well. Fitting errors are consistently less than 15% for almost all elements. The relatively higher errors in fitting the capacitive element at lower frequencies is one of the limitations of the brick layer model detailed by Fleig et al.<sup>151</sup> The model is however highly suitable for analysis of bulk properties. This circuit will hence fore be used in modeling the impedance measurements carried out in this work.

### 5.2.2 Conductivity of undoped CaZrO<sub>3</sub> in air

As electrical conduction in a solid electrolyte is a temperature-activated process, the increase in conductivity with temperature for ceramic materials bears an Arrhenius relationship. Figure 50 shows an Arrhenius plot of the D.C. conductivities measured from an undoped CaZrO<sub>3</sub> pellet at various temperatures in air. The plot also shows conductivity values reported in other literature sources. Wang et al.<sup>152</sup> measured D.C conductivities at a higher temperature range with a pellet synthesized using the solid oxide method. Rog et al.<sup>153</sup> and Dudek et al.<sup>154</sup> have also reported conductivities for pure CaZrO<sub>3</sub>. Conductivities typically around ( $10^{-5}$  ohm<sup>-1</sup>cm<sup>-1</sup> at 900°C) were measured. These agree reasonably well with the literature. They are quite comparable to the values published by Rog et al.,<sup>153</sup> but slightly higher than those reported by Dudek<sup>154</sup> and Wang et al.<sup>152</sup> Discrepancies in the literature can be explained by differences in microstructure since electrical conductivity is extremely sensitive to processing.

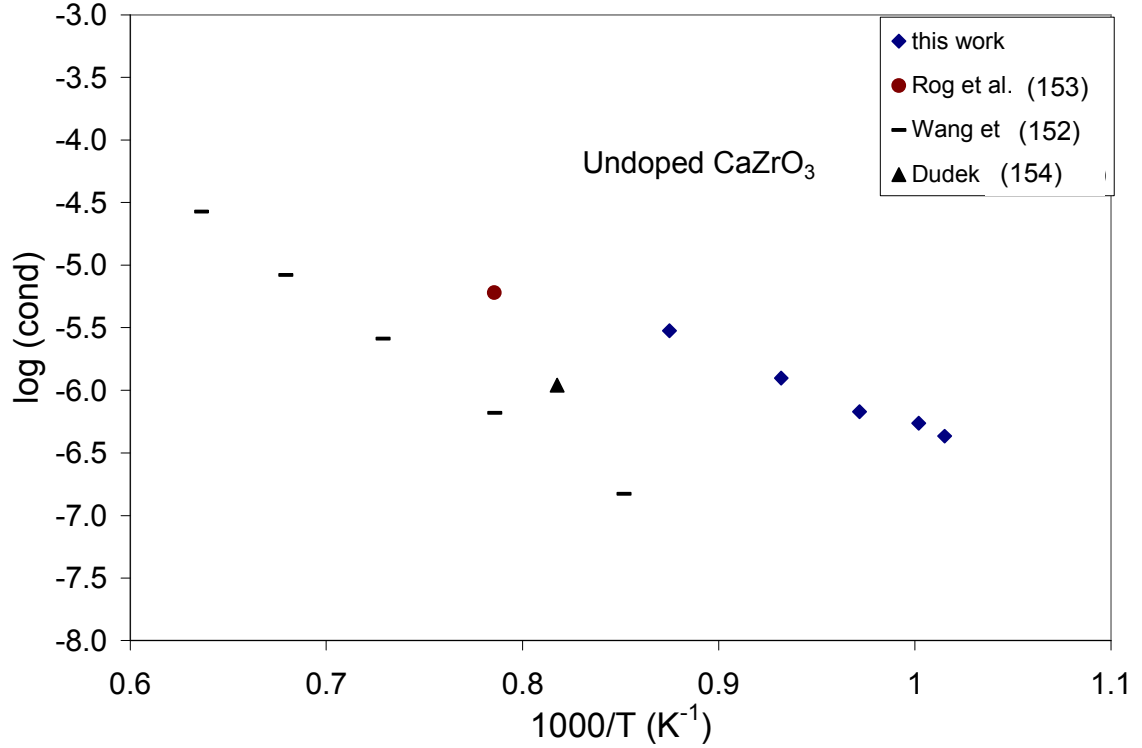


Figure 50 Electrical conductivity of undoped CaZrO<sub>3</sub> measured in air.

The high temperatures necessary for electrical conduction in CaZrO<sub>3</sub> based materials help in overcoming activation energies for the formation and migration of various defect species. The Arrhenius equation for conductivity is written as:

$$\sigma = A \cdot \exp \left[ -\frac{E_a}{RT} \right] \quad (12)$$

where  $\sigma$  is the total conductivity,  $E_a$  is the activation energy,  $R$  is the gas constant,  $T$  is the temperature in K and  $A$  is the pre-exponential factor. Temperature-activated ion hopping is responsible for conduction. The conductivity can be derived from random walk theory and is of the form:<sup>155</sup>

$$\log (\sigma \cdot T) = \log (A) - \frac{E_a}{RT} \quad (13)$$

Using the above equation, the activation energy for the conduction process can be computed from the slope of the line drawn in the plot of  $\log (\sigma \cdot T)$  vs  $1/T$ .

Figure 51 shows an Arrhenius type conductivity plot for undoped  $\text{CaZrO}_3$  measured in air. The measurements are highly linear ( $R^2 = 0.99$ ), with an activation energy of about 1.2 eV, which is in agreement with value of 1.14 eV reported by Hwang et al.<sup>156</sup> for a similar temperature range. The plot also shows linear trends calculated from literature data. Activation energies of 2.16 eV and 2.42 eV were calculated from Janke's<sup>157</sup> measurements with non-stoichiometric  $\text{CaZrO}_3$  at higher temperatures.

De Pretis et al.<sup>158</sup> carried out conductivity measurements on pure  $\text{CaZrO}_3$  and concluded the material to be a p-type conductor in air. This would mean holes are the predominant defect species responsible for conduction across the electrolyte. The Kroger-Vink notation for the formation of holes can be written as:



where  $V_o^{\bullet\bullet}$  is an oxygen vacancy,  $h^{\bullet}$  is a hole and  $O_o^x$  denotes oxygen on an oxygen site.

At 1000°C, Dudek et al.<sup>154</sup> carried out EMF measurements using a concentration cell and measured an oxygen ion transference number of 0.92. This would suggest that pure  $\text{CaZrO}_3$  is mainly an oxygen-ion conductor at higher temperatures. Data from Wang et al.<sup>152</sup> and Janke et al.<sup>157</sup> also agree with this as the activation energy calculated from

their work is close to the ( $\sim 2\text{eV}$ ) value reported for oxygen ion vacancy migration in  $\text{CaZrO}_3$ .<sup>159</sup>

Figure 51 also shows a set of conductivity measurements extracted from A.C. impedance work carried out by Wang et al.<sup>160</sup> While the authors plotted the data set as a single series, it seems better represented when replotted as two different lines split based on the temperature range. The different slopes indicate that the activation energy (or dominant defect species) changes with increase in temperature, which would explain a possible transition of the predominant defect from holes to that of oxygen ion vacancies at the higher temperatures.

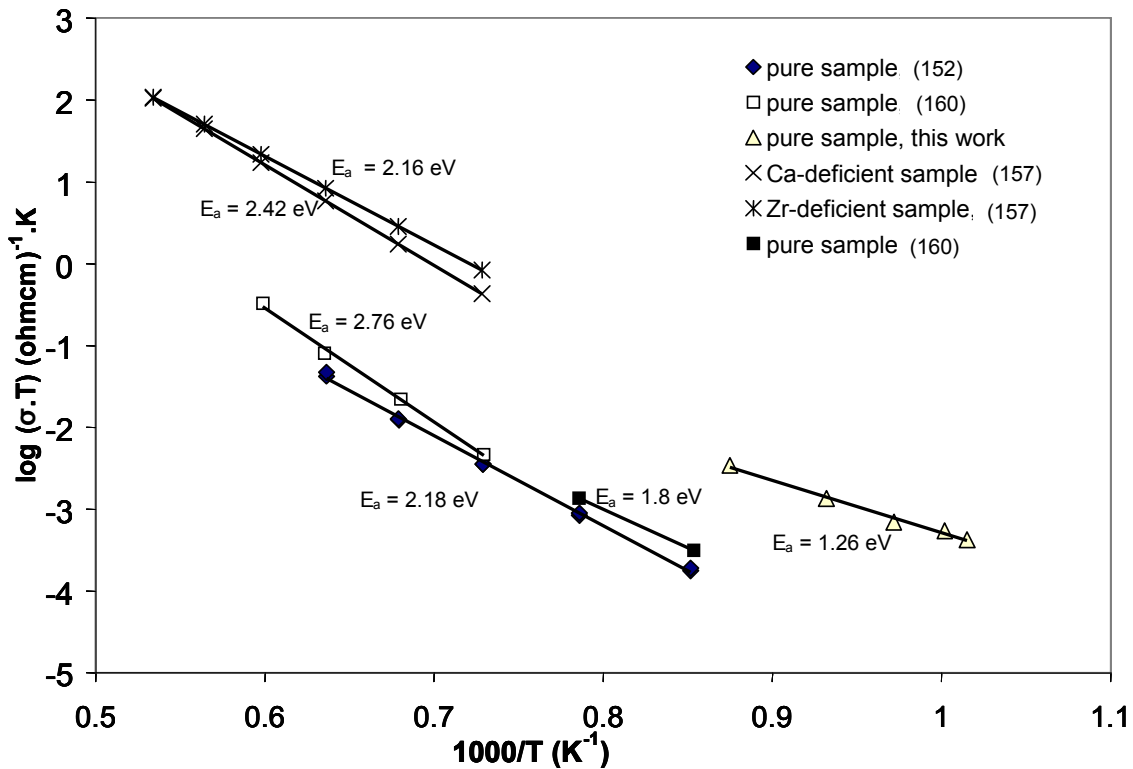


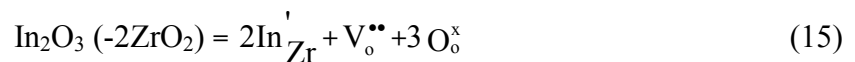
Figure 51 Arrhenius plot of conductivity for samples of  $\text{CaZrO}_3$  measured in air.

Sample description	Reference	Temperature range (K)	Activation energy
Undoped (D.C)	This work	983-1173 K	1.26 eV
Undoped (D.C.)	Hwang et al. <sup>156</sup>	870-1370 K	1.25 eV
Undoped (A.C-hi freq)	Wang et al. <sup>160</sup>	1370-1670 K	2.76 eV
Undoped (A.C-total R)			2.75 eV
CaO+CaZrO3 (D.C)	Janke et al. <sup>157</sup>	1373-1873 K	2.16 eV
ZrO2+CaZrO3 (D.C)			2.42 eV
Undoped (D.C.)	Wang et al. <sup>152</sup>	1173-1573 K	2.18 eV

Table 4 List of activation energies reported for stoichiometric and non-stoichiometric CaZrO<sub>3</sub> according to mode of measurement and temperature range.

### 5.2.3 Conductivity of In-doped CaZrO<sub>3</sub> in air

Although stoichiometric CaZrO<sub>3</sub> seems to behave like a p-type semiconductor in air, changes in the electrical behavior are expected when the dopant is incorporated into the lattice. The introduction of the aliovalent (different valence) In<sup>3+</sup> cation results in a substitution reaction. In<sup>3+</sup> (0.8 Å, VI fold) is closer in size<sup>161</sup> to the Zr<sup>4+</sup> cation in the octahedral arrangement (0.72 Å), than the Ca<sup>2+</sup> cation (1.12 Å ) present in the VIII coordinate site.<sup>63</sup> The substitution therefore causes the replacement of some of the Zr<sup>4+</sup> ions in the lattice and creates oxygen vacancies to maintain electrical neutrality. One vacancy is created for every 2 dopant (In<sup>3+</sup>) substitutions through the following reaction,





where,  $\text{In}'_{\text{Zr}}$  is the substituted indium ion on the zirconium site. While oxygen vacancies form holes in the presence of oxygen, they react with moisture to form protons which dissolve in the lattice. The Kroger-Vink notation for this reaction can be written as,



where  $\text{H}^\bullet$  represents the proton formed.

Bulk conductivity values of  $\text{Ca}(\text{Zr},\text{In})\text{O}_3$  pellets were measured using D.C. and high frequency A.C. measurements. Increases in total conductivity of the material are expected with doping since additional vacancies have been created. Conductivities observed in undoped and indium-doped  $\text{CaZrO}_3$  samples are plotted in Figure 52. Conductivities in 5 mol% In-doped  $\text{CaZrO}_3$  are 1-2 orders of magnitude larger than that observed in undoped samples. Results obtained by Wei et al.<sup>122</sup> also compare well with the observed data as a similar slope is observed. Data fitting using the circuit model yields resistance and capacitance contributions of the bulk and grain boundary components. The magnitude of the slope (and hence  $E_a$ ), should remain unchanged irrespective of whether resistances or conductivities are plotted against temperature, although the sign reverses. The Arrhenius behavior of bulk and grain boundary resistances calculated at various temperatures is plotted in Figure 53.

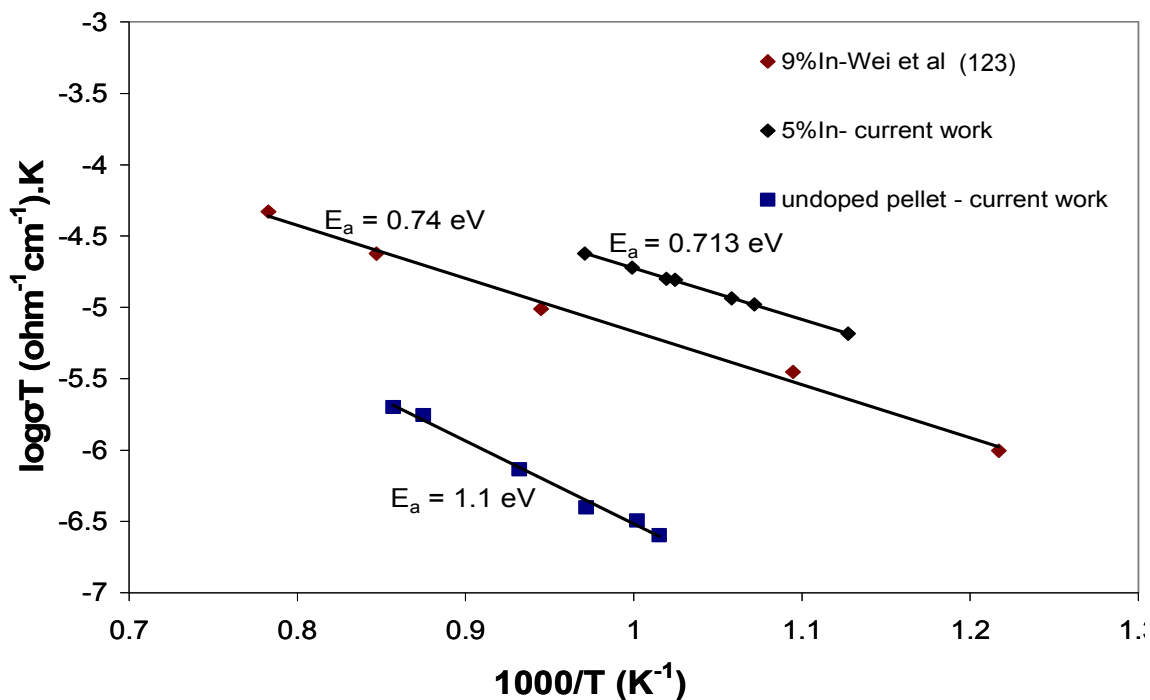


Figure 52 Bulk conductivities observed for  $\text{Ca}(\text{Zr},\text{In})\text{O}_3$  and  $\text{CaZrO}_3$  samples in air

In the plot, R1 represents the high frequency resistance (grain) and R2 represents the low frequency resistance (grain boundary). The D.C resistance measured at the same temperature range using a multimeter is also plotted. A linear trend is observed in all of the data sets. Similar slopes are observed in the lines representing D.C resistance, total resistance (R1+R2) and high frequency bulk resistance (R1). This trend has been previously observed by Wang et al.<sup>160</sup> The activation energies calculated from the various slopes are shown in the figure.  $E_a$  for bulk conduction (from R1) from a  $\text{CaZr}_{0.95}\text{In}_{0.05}\text{O}_{3-x/2}$  sample measured in air was  $\sim 0.7$  eV, whereas that for grain boundary conduction (from R2) was  $\sim 1$  eV.

The measured bulk  $E_a$  value (0.7 eV) matches well with the 0.76 eV measured by Kurita et al.<sup>162</sup> for protonic conduction. Since holes are suspected to be responsible for

conduction in undoped CaZrO<sub>3</sub> tested in air, the shift towards proton conduction must be due to doping. The creation of protons has already been discussed as shown in (4). Using molecular dynamic simulations, Islam<sup>163</sup> predicted an interstitial position for the proton which moves by way of inter-octahedra jumps between the oxygen atoms. The author calculated activation energy of 0.74 eV for the protonic conduction, a value that agrees well with this work as well as other experimental data.

The activation energy associated with low frequency grain boundary resistance (R<sub>2</sub>) appears to be higher than that measured for bulk and total resistance. This matches findings from Hwang et al.,<sup>156</sup> who measured bulk activation energy of 0.85 eV and grain boundary activation energy of 1.2 eV. The higher activation energy could be due to inhomogeneities present in the grain boundaries that could impede the ion hopping processes.

The time constants for the individual relaxation processes ( $\tau_1 = R_1C_1$ ,  $\tau_2 = R_2C_2$ ) were calculated using the individual resistance and capacitance values obtained from the data fit. The Arrhenius plot of these two time constants is shown in Figure 54. The slope of the line attributed to the bulk time constant matches that observed for bulk resistance. Similar slopes would mean similar activation energies, indicating that the bulk capacitance remained invariant with temperature. This trend has been observed in pure CaZrO<sub>3</sub> samples by Wang et al.<sup>160</sup> The grain boundary time constant had a different activation energy (0.6 eV) from that of grain boundary resistance (1.07 eV). It should be noted that the linear fit however, does not seem to be satisfactory with a R<sup>2</sup> value of 0.62.

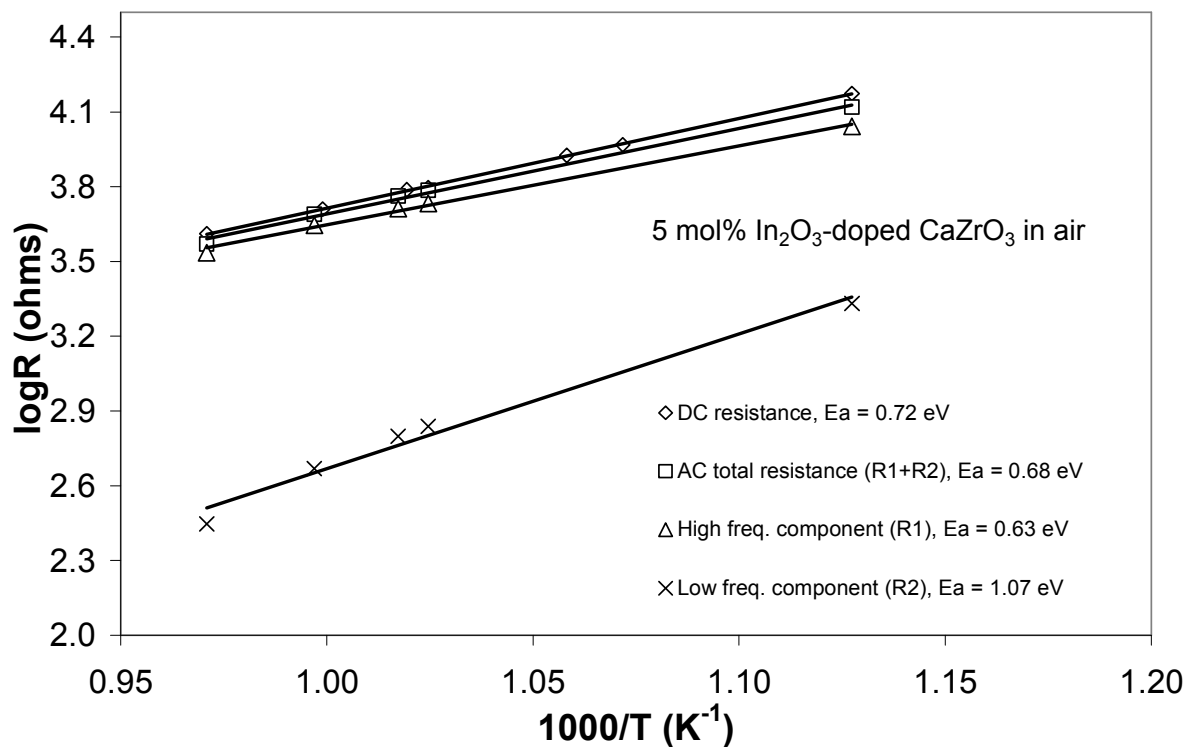


Figure 53 Variation of resistance with temperature in CaZr<sub>0.95</sub>In<sub>0.05</sub>O<sub>2.975</sub> measured in air.

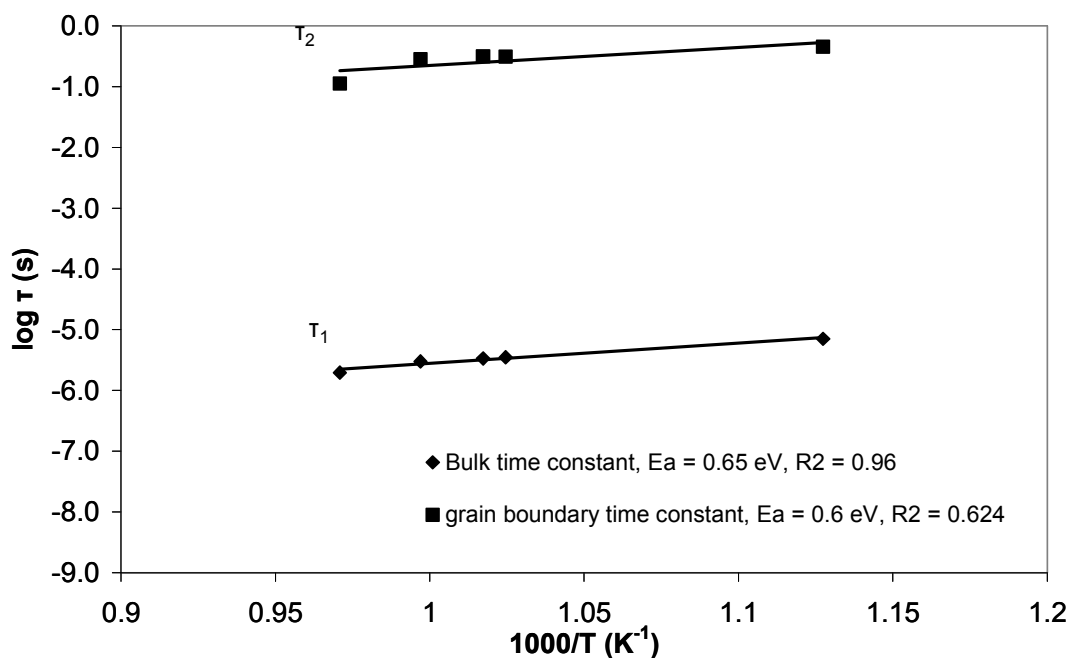


Figure 54 Variation of time constants with temperature for CaZr<sub>0.95</sub>In<sub>0.05</sub>O<sub>3-α</sub> measured in air.

Capacitances obtained from the data fit are plotted in Figure 55. Data reported by Wang et al.<sup>160</sup> is also shown for comparison. Bulk capacitances are found to be of the order of ( $\sim 0.1\text{nF}$ ), while grain boundary capacitances which remain high presumably due to the presence of impurities, are close to ( $\sim 1\mu\text{F}$ ). Capacitances attributed to the bulk appear to remain constant with temperature, while grain boundary capacitances seem to vary with temperature, a trend different from that observed in pure  $\text{CaZrO}_3$  by Wang et al.<sup>160</sup> However, there seems to be again considerable scatter in the points similar to the component's resistance and time constant contributions plotted earlier.

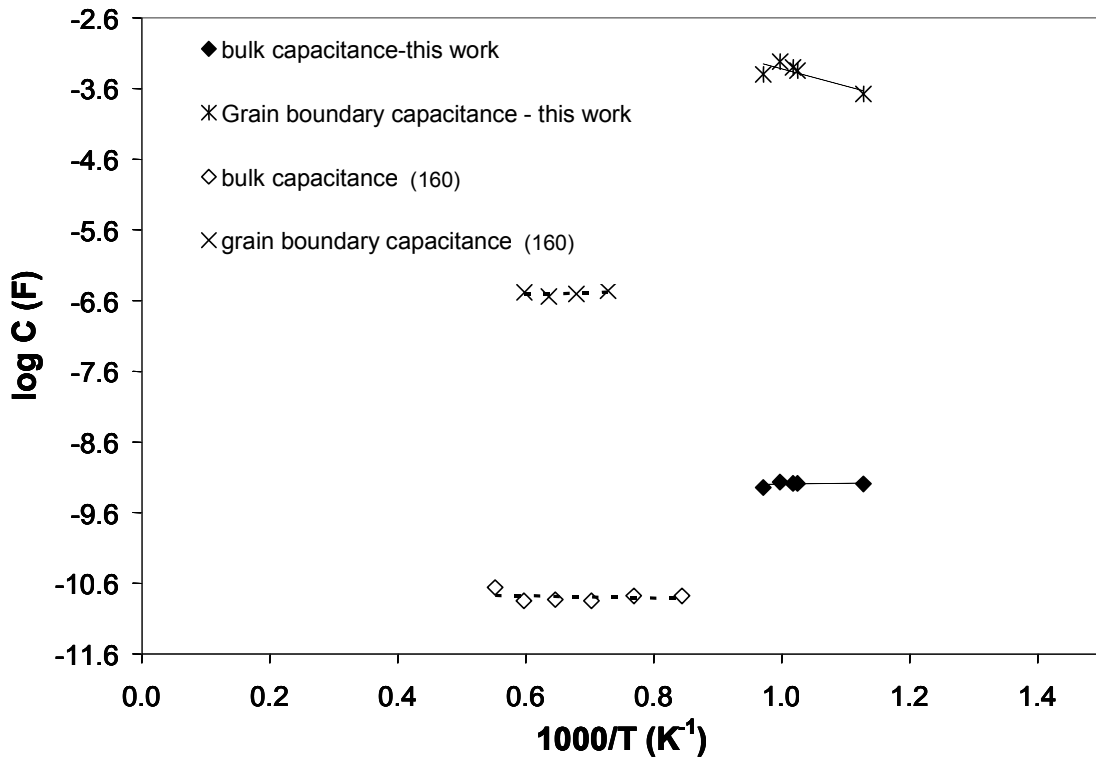


Figure 55 Variation of capacitances in In-doped  $\text{CaZrO}_3$  measured in air.

This trend is also seen in Figure 56 where values of the exponent  $n$  are plotted against temperature. The parameter is obtained from the data fit where the constant phase element is used to model the impedance data.<sup>164</sup> A value of 1 means the CPE acts as a

pure capacitor and indicates homogenous dispersion. As seen in Figure 56, bulk values of  $n$  remain close to 1 and are unchanged with temperature. Grain boundary  $n$  values are well below 1, which could be due to their high heterogeneity.

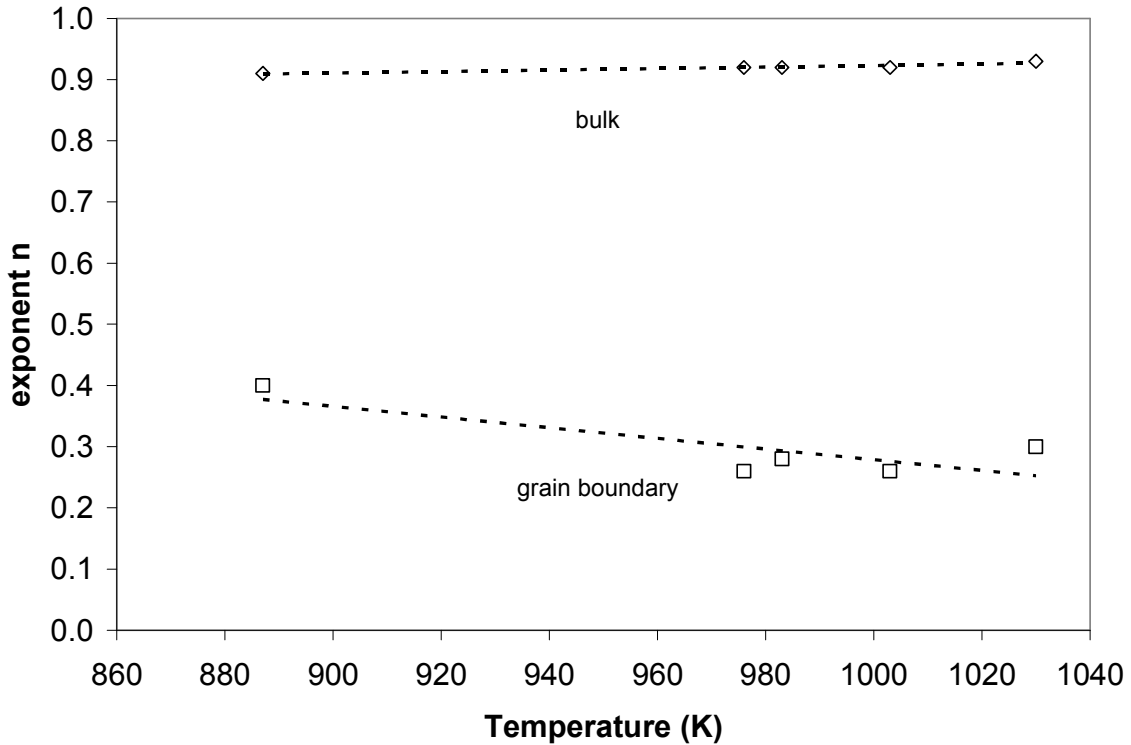


Figure 56 Variation of exponent  $n$  with temperature in In-doped  $\text{CaZrO}_3$ .

#### 5.2.4 Conductivity of In-doped $\text{CaZrO}_3$ in dry argon

In order to understand the electrical properties of  $\text{Ca}(\text{Zr},\text{In})\text{O}_3$  materials at a lower oxygen partial pressure ( $p\text{O}_2$ ) the sample pellet was tested in dry argon atmosphere. Impedance spectra similar to those shown in Figure 46 were measured. These typically consisted of two semicircles and the data was fit with a circuit model similar to that shown earlier in Table 3. Figure 57 shows the Arrhenius plot of conductivities obtained from the high and low frequency resistances measured in dry argon. The activation energy for the high frequency resistance in argon (0.9 eV) is higher than that measured in

air (0.6 eV). This suggests that the possible defect mechanism might be that of p-type conduction.

Other researchers have worked on measuring the individual electrical parameters involved in hole conduction. Yamaguchi and co-workers<sup>165</sup> carried out computations from diffusion experiments to calculate the formation energy and mobility of holes in In-CaZrO<sub>3</sub>, which are replotted in Figure 59 and Figure 60. From the slopes of the linear trend line drawn through the data points, activation energies for hole formation and migration were calculated as 0.77 eV and 0.19 eV, respectively. Since the total activation energy for the hole conduction process is the sum of two individual activation energies, an activation energy of  $E_a = 0.96$  eV was obtained for hole conduction.

The activation energy for the bulk contribution in dry argon (0.9 eV) matches well with that discussed earlier for hole conduction. This also compares well with the activation energy computed by Yamaguchi et al.<sup>165</sup> In-doped CaZrO<sub>3</sub> seems to be a high temperature proton conductor in air as discussed in Figure 53. However, the absence of moisture in argon might be responsible for the replacement of protons by holes as the dominant conduction mechanism. Figure 57 also shows the activation energy for grain boundary conduction is 1.2 eV. This is higher than that for bulk conduction (0.67 eV) and similar to results obtained for In-doped CaZrO<sub>3</sub> measured in air. Bulk capacitances obtained from the data fit are plotted in Figure 58. Two separate experimental runs showed these to decrease with an increase in temperature, a different trend from that observed in Figure 55. This behavior is however consistent with other perovskites like CaTiO<sub>3</sub> (isostructural with CaZrO<sub>3</sub>) and BaTiO<sub>3</sub> which show a decreasing dielectric constant with temperature and follow the Curie-Weiss law.<sup>166,167</sup> Since dielectric constant

is directly related to capacitance ( $C = kA\epsilon_0/d$ ), the capacitance in these materials must also decrease with temperature.

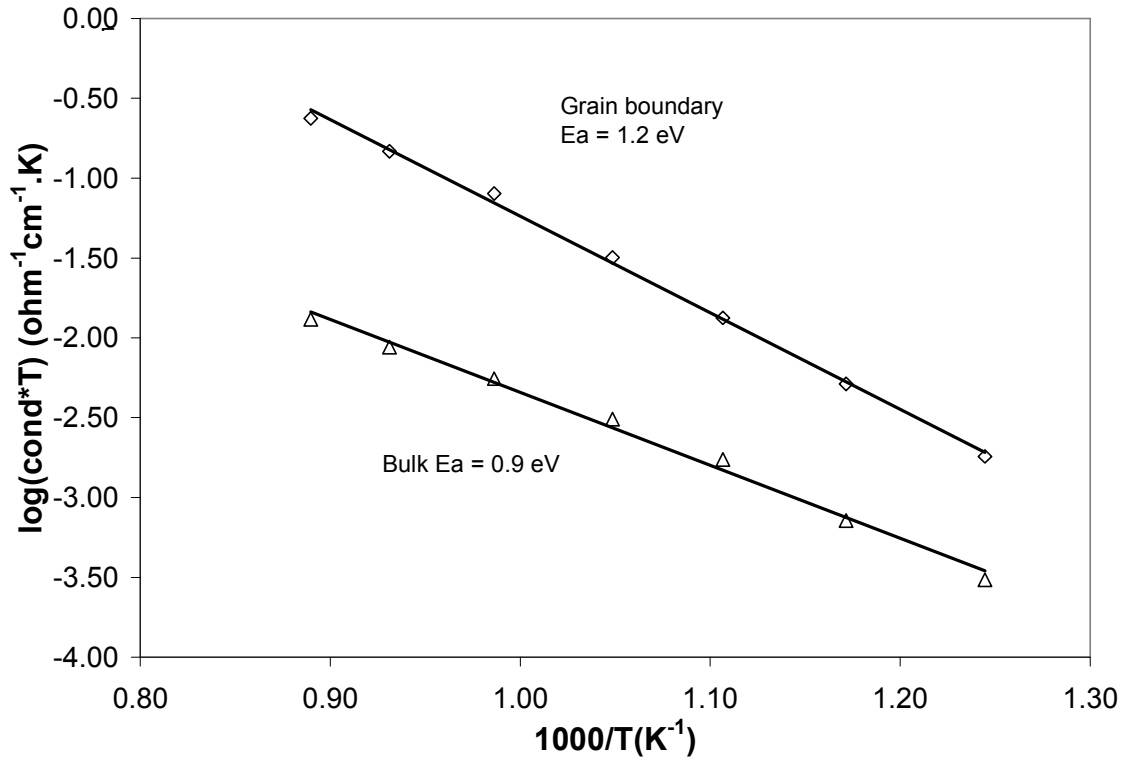


Figure 57 Bulk and grain boundary conductivity of In-doped CaZrO<sub>3</sub> in argon.

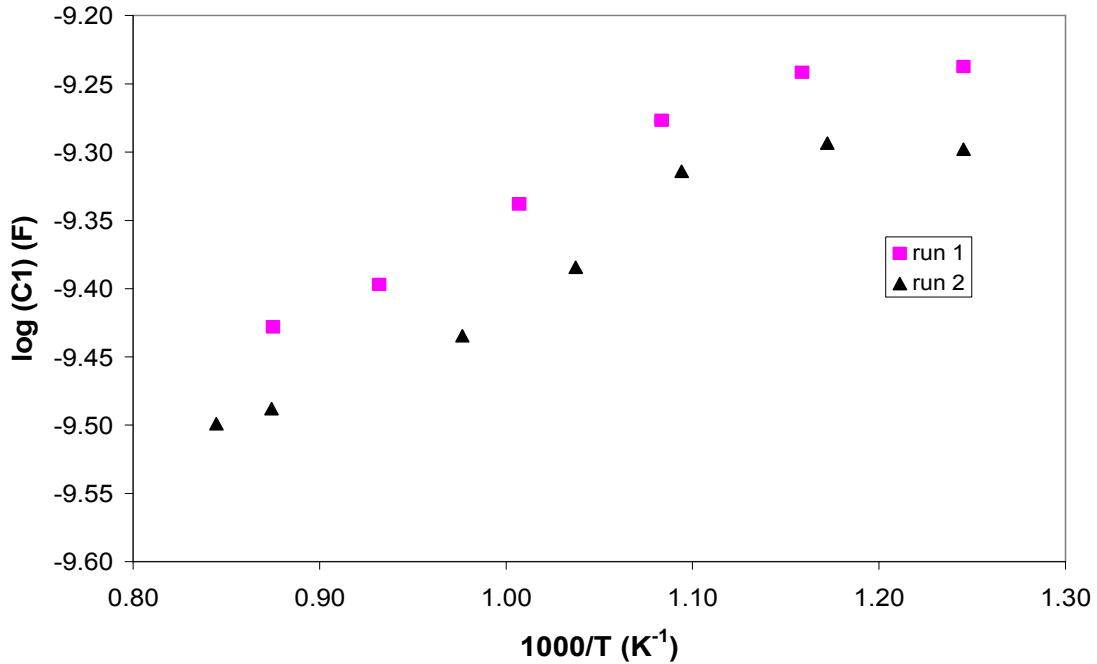


Figure 58 Variation of bulk capacitance in In-doped CaZrO<sub>3</sub> with temperature in argon.



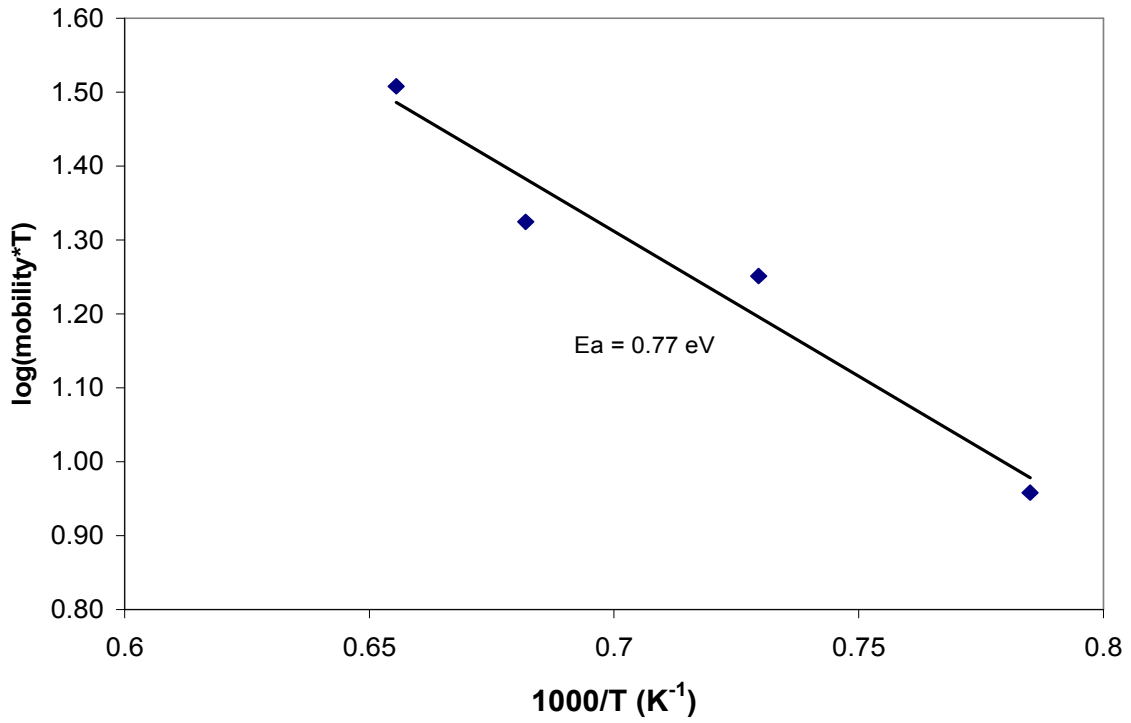


Figure 59 Arrhenius plot of hole mobilities in In-doped  $\text{CaZrO}_3$ .

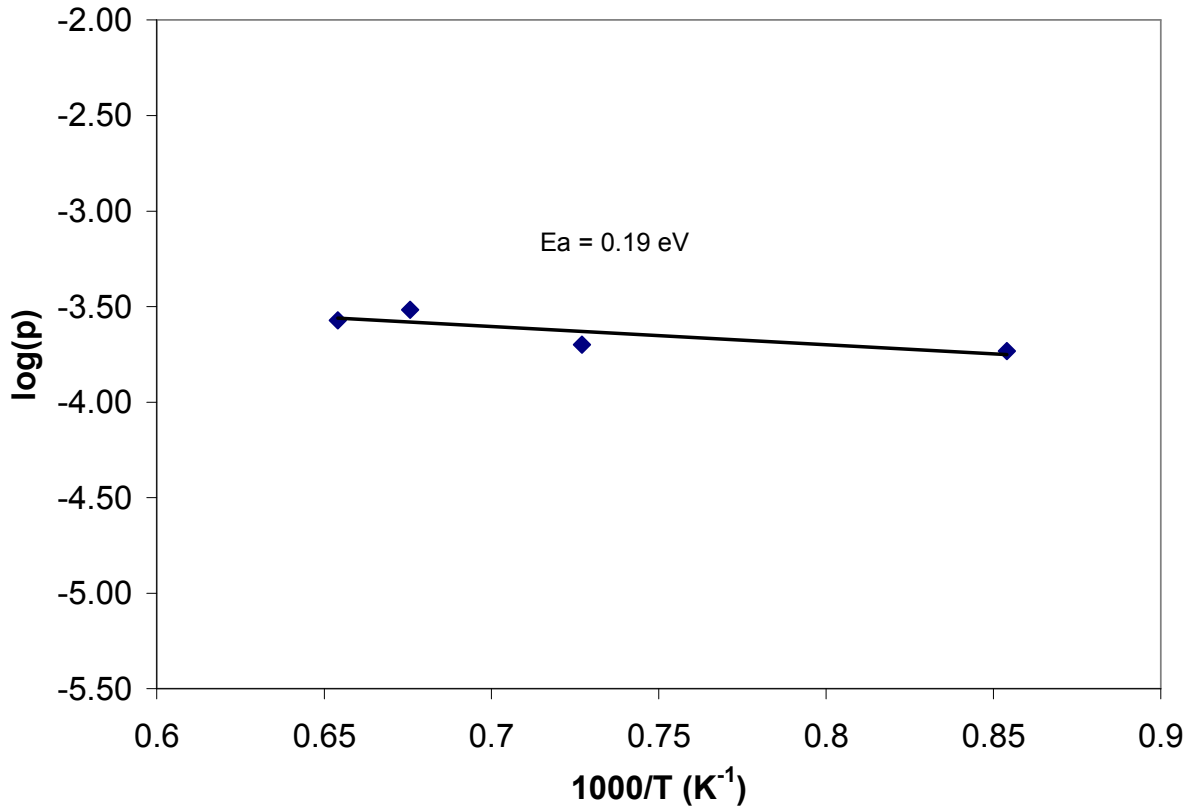


Figure 60 Activation energy for the creation of holes in In-doped  $\text{CaZrO}_3$ .

### 5.2.5 Conductivity of In-doped CaZrO<sub>3</sub> in Ar+H<sub>2</sub>O

It has been thus far been discussed that protonic conduction could be the dominant conduction mechanism in In-doped CaZrO<sub>3</sub> measured in air, whereas p-type (hole) conduction is prevalent in argon environments (low H<sub>2</sub>O, low pO<sub>2</sub>). Addition of water in dry argon helps test the doped material in a different condition (high pH<sub>2</sub>O, lower pO<sub>2</sub>). The introduction of water might cause protons to form and replace holes as the dominant species; a mechanistic change that can be identified by looking at the activation energy obtained from the Arrhenius plots of conductivity.

To test this hypothesis, D.C and A.C measurements were made across a 10-mol% In-doped CaZrO<sub>3</sub> pellet in an environment of (Ar+H<sub>2</sub>O). In the case of impedance measurements, a 2 layer BLM was used to model the data and extract resistance and capacitance values. The resistances obtained were used to calculate A.C. conductivities using sample dimensions.

D.C. and A.C. conductivities obtained from the pellet sample are shown in Figure 61 and Figure 62. The activation energies are 0.68 eV and 0.76 eV, respectively, which match well with the previously discussed results for protonic conduction. Thus, protons might replace holes as the major mechanism even at lower pO<sub>2</sub>'s as long as moisture is present.

### 5.2.6 Electrical properties of Mg-doped CaZrO<sub>3</sub>

Pellets formed from CaZr<sub>1-x</sub>Mg<sub>x</sub>O<sub>3-x</sub> (0 < x < 0.15) powders were characterized using conductivity measurements. An Arrhenius-type plot for pellets with varying amounts of the dopant is shown in Figure 63.

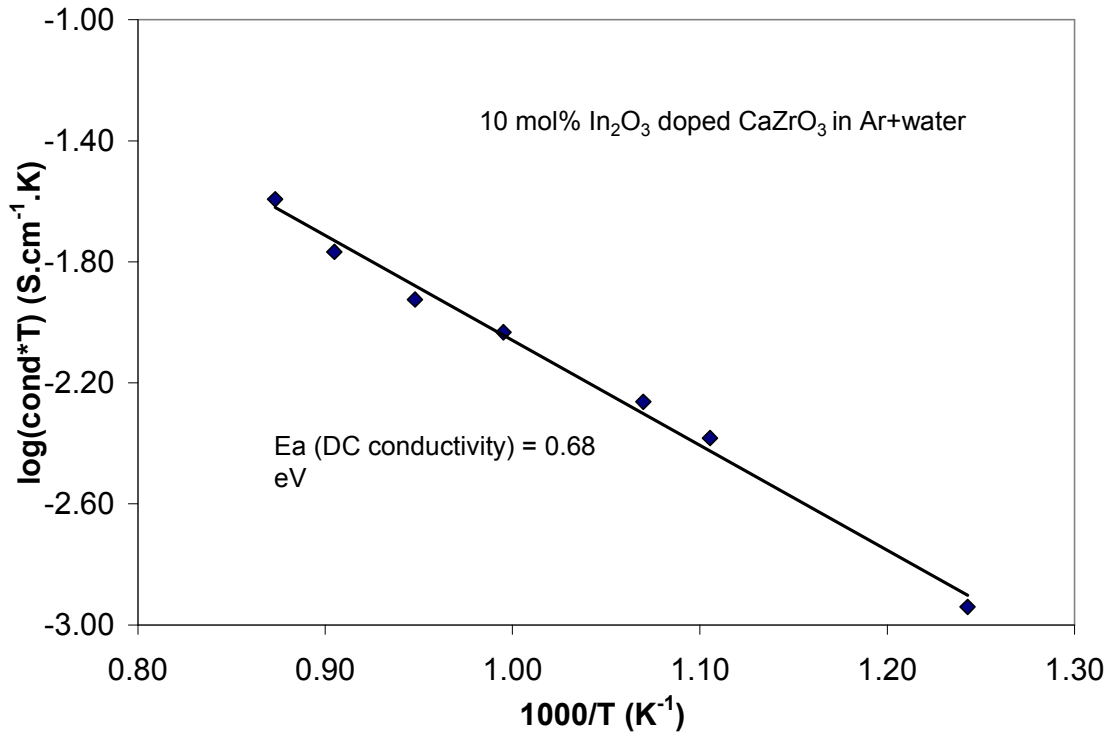


Figure 61 DC conductivity measured for CaZr<sub>0.9</sub>In<sub>0.1</sub>O<sub>3-x/2</sub> exposed to Ar+H<sub>2</sub>O.

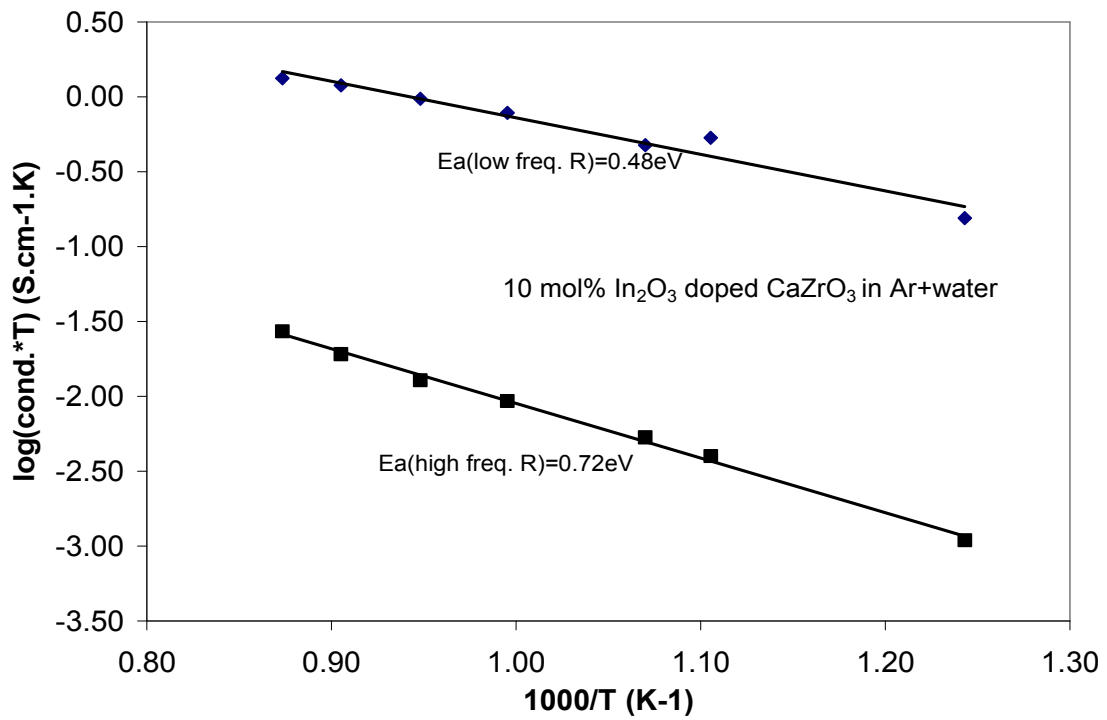


Figure 62 DC conductivity measured for CaZr<sub>0.9</sub>In<sub>0.1</sub>O<sub>3-x/2</sub> exposed to Ar+H<sub>2</sub>O.

Mg-doping was found to increase the total conductivity of  $\text{CaZrO}_3$ , although conductivities were typically lower than those measured for In-doped  $\text{CaZrO}_3$ . Samples with 5% Mg doping showed the highest conductivity, as pellets with higher Mg concentrations showed reduced values. A reduced grain boundary resistance for samples with low Mg content might explain the improvement in total conductivity. Since Mg solubility in  $\text{CaZrO}_3$  has been reported to be very low,<sup>168,169</sup> the formation of a secondary phase might occur at the grain boundaries for higher Mg concentrations (10% and 15%). This could result in a decrease in the total conductivity.

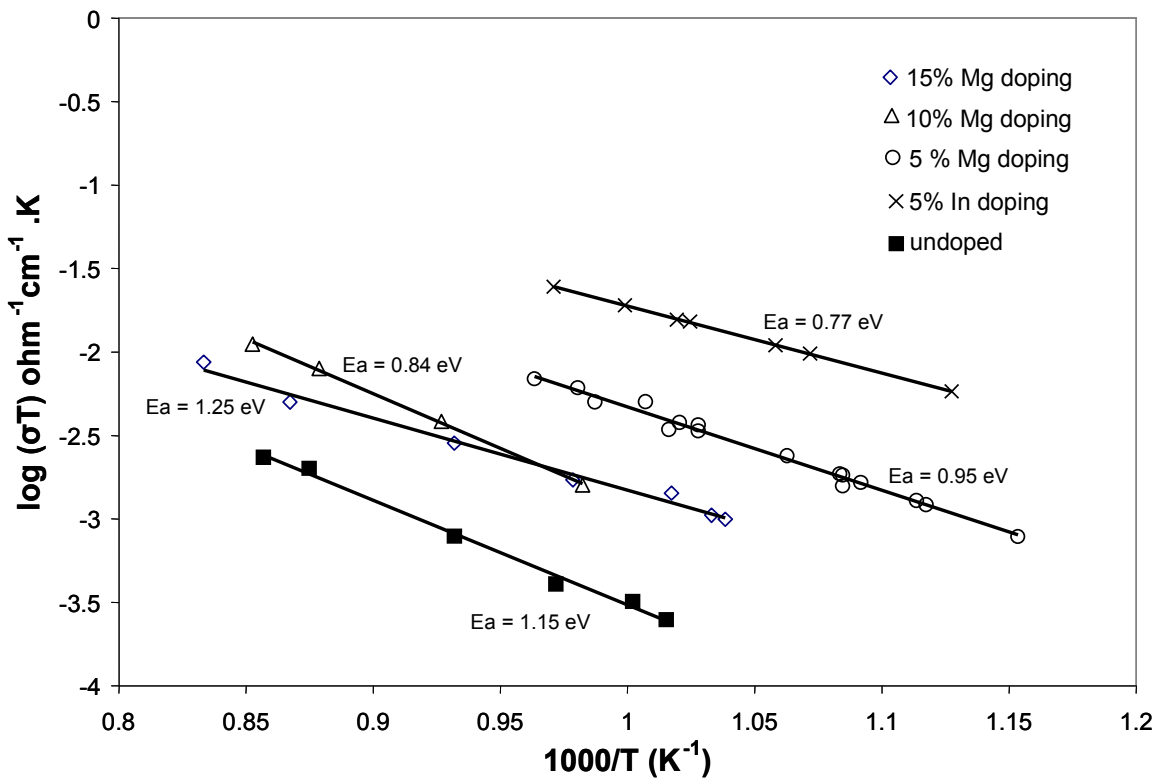


Figure 63 Total conductivities measured for  $\text{CaZr}_{1-x}\text{Mg}_x\text{O}_{3-x}$  pellets. Results compared with undoped and In-doped  $\text{CaZrO}_3$ .

### 5.2.7 Alternate equivalent circuit model

The impedance spectra discussed thus far were modeled using the 2 layer BLM circuit. Although this model represents the data well, the empirical nature of the constant phase element poses limitations. Since the presence of this element could be explained by various physical processes, it could be advantageous to reduce the number of CPE's used in the data fit.

Impedance data analyzed by the brick layer model indicates a heterogeneous grain boundary contribution. The grain boundaries may be sites for possible charge-trapping mechanisms. The trapping effect has been routinely modeled by various researchers using a RC series combination.<sup>170</sup> To model the entire spectrum using fewer CPE elements, a slightly different equivalent circuit was used. A simple version of this circuit has been used to fit data from the  $M^*$  and  $Y^*$  planes of the complex data (other immittance representations) as shown by Wang et al.<sup>160</sup> An admittance plot of the complex data at 870°C (1MHz-1Hz) is shown in Figure 64. The curve contains a small contribution at the low frequencies followed by a tail at the higher frequencies. Frequency analysis suggests that the demarcation point between the 2 features matches well with the onset of the second semicircle in the impedance plots, shown previously in Figure 46.

Figure 65 shows the circuit parameters obtained for the same temperature using the reduced CPE model. All the parameters seem to be estimated with reasonable errors. The magnitude of the high frequency resistance  $R_1$  (35,764 ohms) matches well with the sum of the 2 resistances ( $R_1$  and  $R_2$ ) extracted using the earlier model (Table 3). This could be taken to represent the D.C. resistance of the pellet. The capacitance term of the

constant phase element CPE1-T corresponds to high frequency capacitance and agrees well with the value obtained from the previous model. The RC terms in series represent the trapping process across a grain boundary. The time constant calculated for this process agrees well with that reported by Wang et al.<sup>162</sup> for pure CaZrO<sub>3</sub>. The new model thus offers an alternate approach to data fitting.

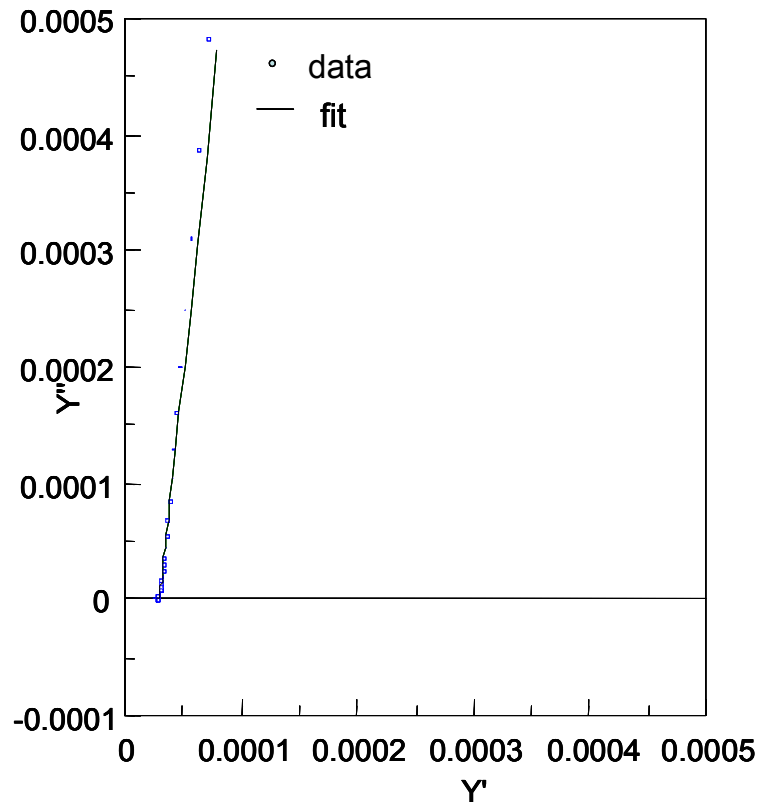
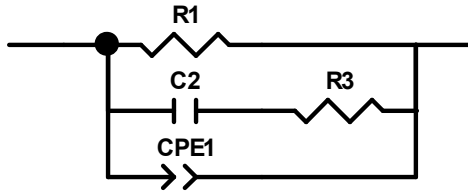


Figure 64 Admittance representation of impedance data measured from  $\text{CaZr}_{0.9}\text{In}_{0.1}\text{O}_{3-\alpha}$  pellet at 870°C.



Element	Value	Error (%)
R1 (ohms)	35764	0.3
C1 (F)	2.00E-09	14
R2 (ohms)	4.20E+05	5.6
CPE1-P	0.94	0.24
CPE1-T (F)	4.00E-10	3.2

Figure 65 Circuit parameters extracted from impedance data at 870°C using the reduced CPE model

### 5.2.8 Electrical characterization of In-doped CaZrO<sub>3</sub> at very low oxygen partial pressures

None of the electrical property investigations of CaZrO<sub>3</sub> based electrolytes have characterized the material at the very low oxygen pressures prevalent in the aluminum melt. Such low oxygen partial pressures could very well affect and change the defect mechanisms responsible for ionic conduction.<sup>171</sup> Kurita et al.<sup>162</sup> developed a conduction domain map for the material by making impedance spectroscopy measurements at a variety of oxygen and hydrogen partial pressures fixed using gas (argon and H<sub>2</sub>/H<sub>2</sub>O) mixtures. The prevalent hydrogen and oxygen partial pressures in molten aluminum are highlighted in Figure 67, which shows the domain diagram at 750°C.

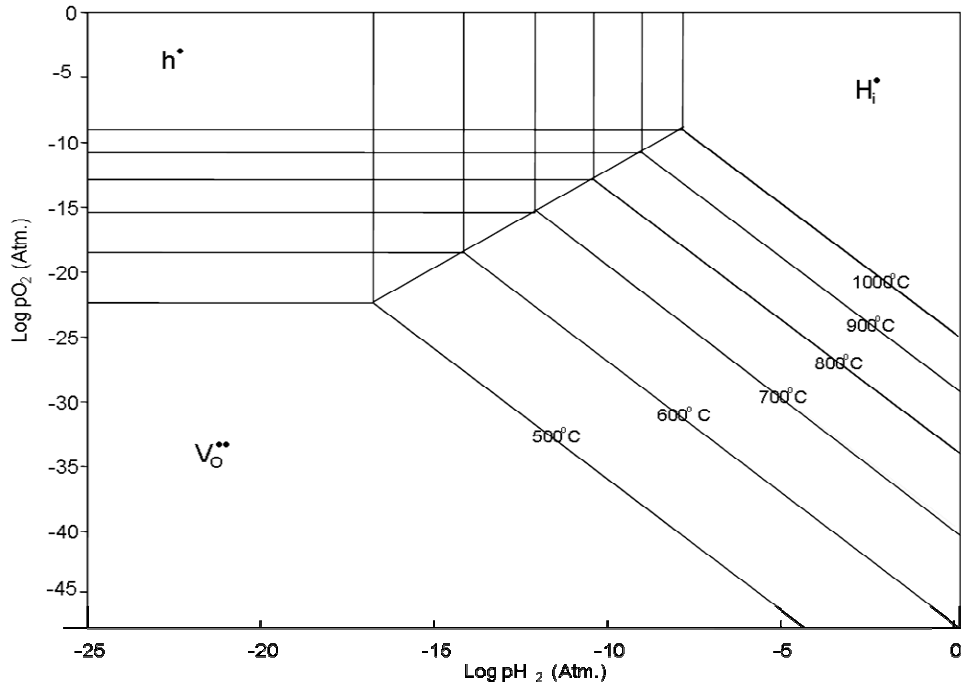


Figure 66 Conduction domain diagram developed by Kurita et al.<sup>162</sup> to describe the defect properties of  $\text{CaZr}_{0.9}\text{In}_{0.1}\text{O}_{3-x/2}$  materials.

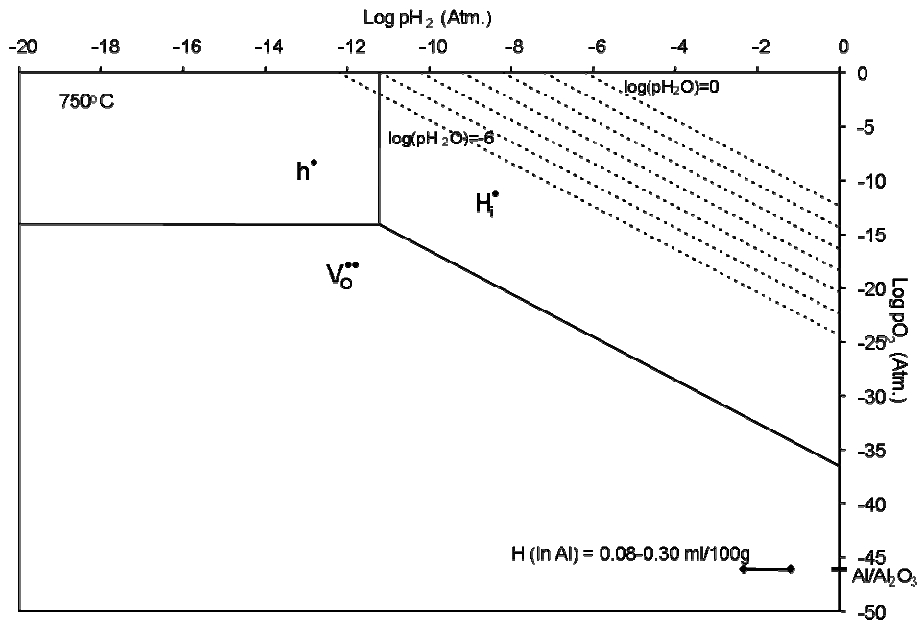


Figure 67 Domain diagram highlighting the oxygen and hydrogen partial pressures in molten aluminum at 750°C.



Impedance measurements at low oxygen partial pressures were made using the setup detailed in Figure 17. Figure 68 shows a typical spectrum obtained in molten aluminum at 840°C. A 2 layer brick layer model similar to the one shown in Table 3 was found to fit the obtained data well. An additional low frequency component was seen in the spectra obtained in solid aluminum, whose spectrum is shown in Figure 69. This element could be attributed to the formation of a surface layer on the electrolyte tube or a significant increase in interfacial resistance, and was modeled by adding another R-CPE element in series. Values of resistance obtained from the data fit were used to compute the conductivity by making estimates of tube thickness and area wetted by molten aluminum.

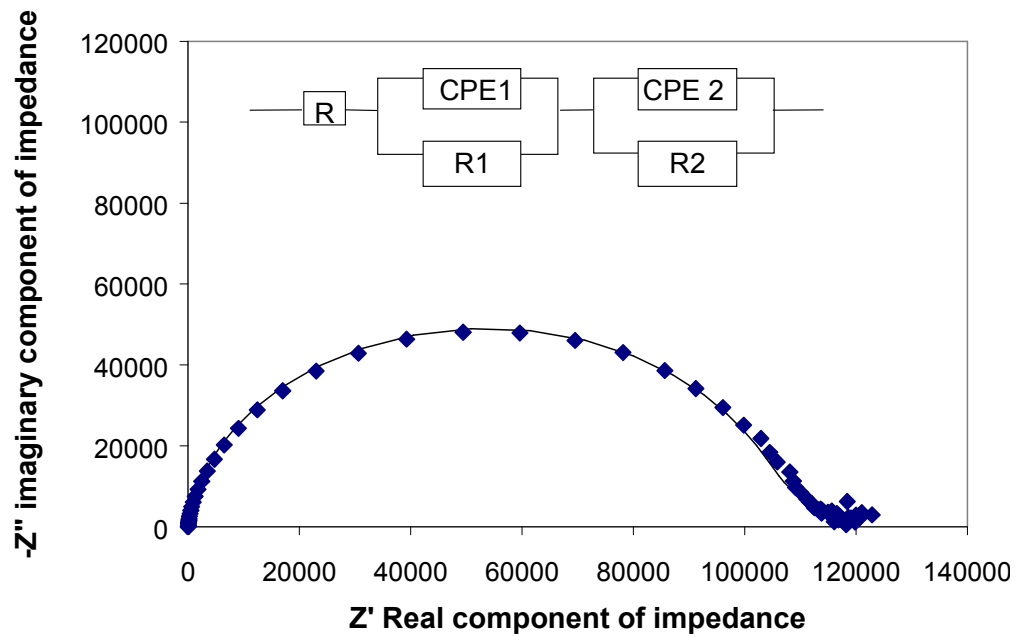


Figure 68 Typical impedance spectrum measured in liquid aluminum at 1000K.

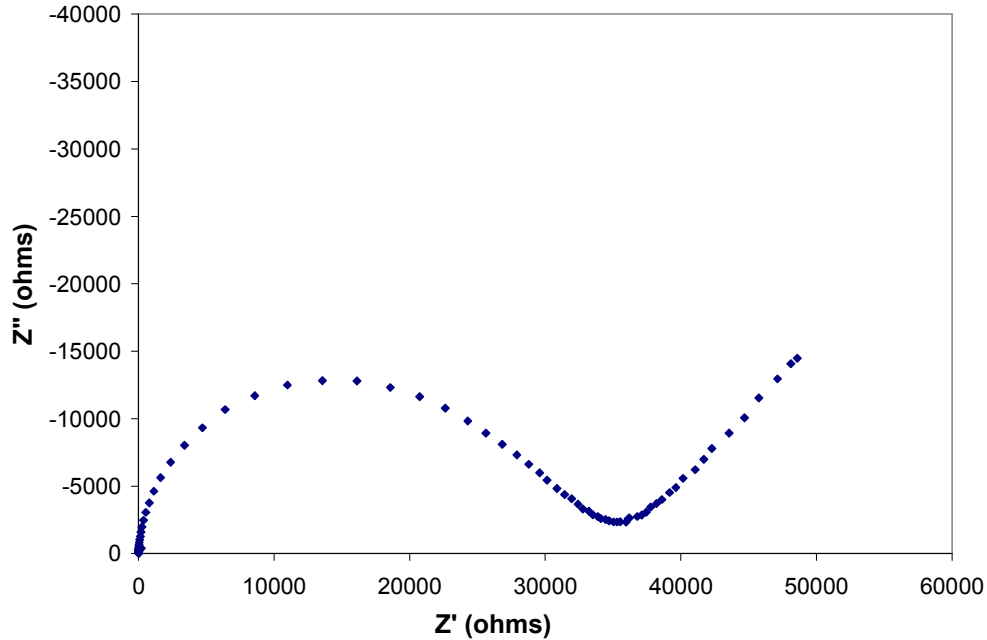


Figure 69 Typical impedance spectrum measured from a  $\text{Ca}(\text{Zr,In})\text{O}_3$  tube inserted in solid aluminum.

Conductivity computations using these measurements were more complex as the contact area in the case of tubular samples is limited by the liquid aluminum inside the tube. Any oxidation of the aluminum inside the tube would change the contact area, thus increasing the total resistance. Prolonged exposure to molten aluminum affected the sealant material used to separate the liquid aluminum on both sides of the electrolyte. A very low resistance (or a short) was observed between the lead wires during several experiments, as liquid aluminum from the graphite crucible entered inside the electrolyte tube due to a failure in the seal.

### 5.3 Sensor fabrication and testing

#### 5.3.1. Sensor design and measurements in argon

Concentration cells were fabricated using tubular shaped  $\text{Ca}(\text{Zr},\text{In})\text{O}_3$  solid electrolyte structures with Mg-MgO mixtures as the reference electrode. Figure 70 shows the voltage response from these types of devices measured in argon. An EMF of  $\sim 2.35$  V was measured across the cell across which can be represented by:

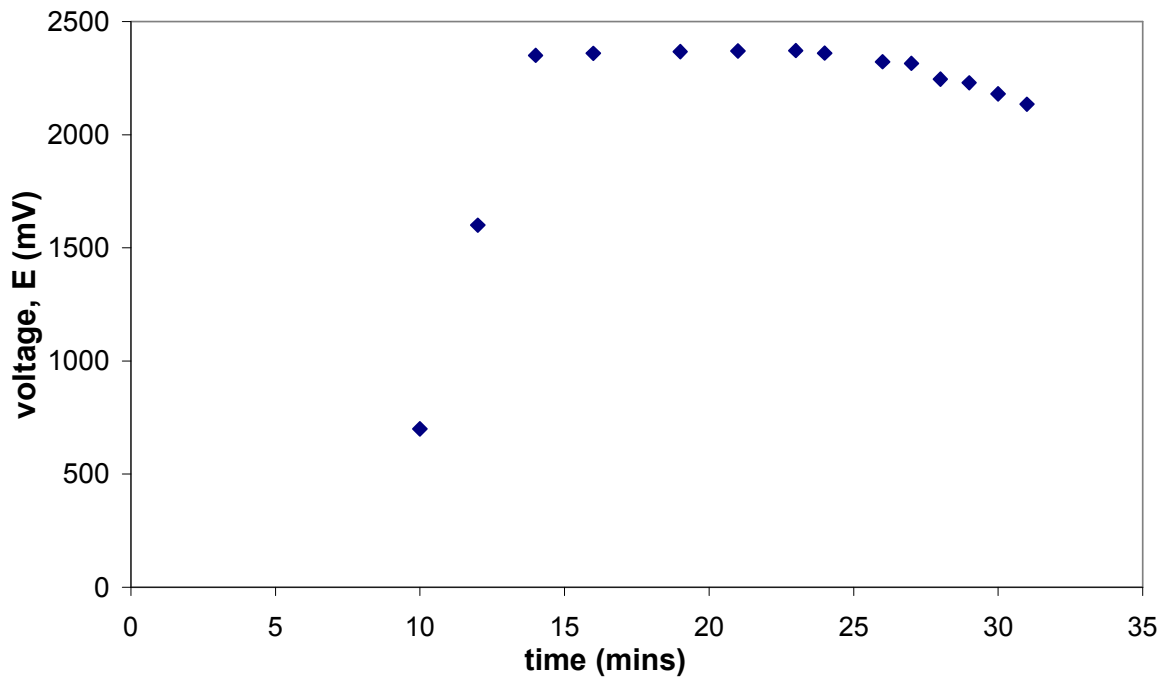
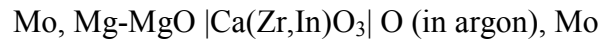


Figure 70 Voltage between argon and Mg-MgO measured using  $\text{CaZr}_{0.9}\text{In}_{0.1}\text{O}_{2.75}$  as the solid electrolyte.

To compare the measured voltages with the theoretical expected EMF, the oxygen partial pressures on both sides of the solid electrolyte were calculated. The oxygen partial

pressures in the reference side is fixed by the equilibrium between Mg and MgO according to the equation,



The equilibrium oxygen pressure ( $p_{\text{O}_2}$ ) established by this mixture at 730°C was calculated using the Gibbs formation energy of MgO ( $\Delta G_f$ ) according to the equation,

$$\Delta G_f(\text{MgO}) = RT \ln K = RT \ln [p_{\text{O}_2}]^{1/2} \quad (18)$$

By substituting the value of  $\Delta G_f(\text{MgO})$  from JANAF thermochemical tables,<sup>172</sup> an oxygen partial pressure of  $\sim 10^{-51}$  atm was calculated.

The specifications on the argon gas cylinder (AR 300) obtained from Airgas lists the oxygen content as < 5ppm and water content as < 10 ppm. A complete list of the various impurities present in argon is given in Table 5.

Impurity type	Levels
CO2	< 1 ppm
Nitrogen	< 20 ppm
Oxygen	< 5 ppm
Hydrocarbons	< 1 ppm
Water	< 10 ppm

Table 5 List of gas specifications obtained for AR 300 from Airgas.

Based on the values listed in the above table, an oxygen partial pressure of  $10^{-4}$ - $10^{-5}$  atm can be assumed to be the possible oxygen content present in argon. Figure 67 indicates that oxygen vacancies might be the predominant conduction defect at the low oxygen partial pressures ( $\sim 10^{-5}$  atm) established by the Mg-MgO mixture. Since the  $\text{Ca}(\text{Zr},\text{In})\text{O}_3$  tube is exposed to Mg-MgO and argon on opposite sides, the theoretical voltage expected across the solid electrolyte can be calculated from the Nernst equation. By substituting required parameters in equation (10), the value of E was calculated as  $\sim 2.3$  V. This matches well with the voltage measured in Figure 70, indicating that the sensor could measure the theoretical voltage even when exposed to low oxygen partial pressures.

EMF measurements were also made to compare the performance of pellet and tubular shaped devices with Mg-MgO reference electrodes. Figure 71 shows responses measured from these sensors tested in argon. The devices appeared to show similar responses as a potential difference of  $\sim 750$  mV was measured across both cells. There was however a significant difference in the response times shown by the two designs. The pellet based device showed a stable EMF after  $\sim 2.5$  hours, while the tubular device needed about 30 minutes to stabilize.

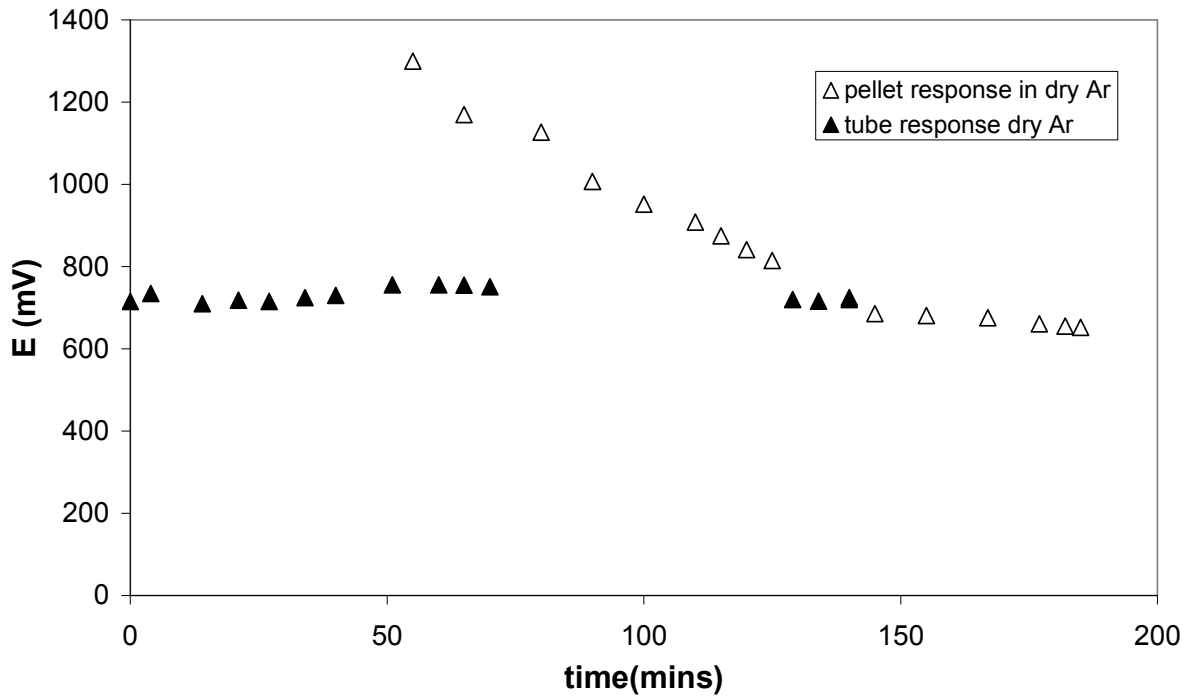


Figure 71 Comparison of voltage response at 720°C from tubular and pellet shaped electrolyte samples tested in Ar with Mg/MgO reference electrode. Cell construction used a porous support tube.

The trends observed in the above plot can be explained by considering the mechanisms involved in establishing the voltage. The measured EMF must depend on the oxygen partial pressure difference set up across the faces of the electrolyte and should not vary with cell geometry and dimensions. Response times, on the other hand, are strongly influenced by the migration of defects through the electrolyte material. These depend on the thickness of the electrolyte layer and should be longer in the pellet based device (thickness,  $t = 3\text{mm}$ ) compared to the tubular based cell design ( $t = 0.9\text{ mm}$ ). Devices based on solid electrolyte tubes were hence used for all further experiments.

The theoretical voltage ( $E = \sim 2.35 \text{ V}$ ) was found to be much higher than that measured experimentally ( $E = \sim 750 \text{ mV}$ ). The smaller experimental value could be due to a higher oxygen pressure in the reference section than that calculated from equilibrium. Both designs had the solid electrolyte element sealed to an alumina based porous support tube similar to that shown in Figure 18. This could have allowed oxygen to enter the reference section thus increasing the oxygen content. The result can also be explained by considering the exact location of the lead wire inside the reference section, as a higher oxygen partial pressure would be measured if the wire were placed locally in an area of high oxygen content. The cell tested in Figure 70 did not use the porous support tube, and had a direct seal between the ceramic sleeve containing the lead wire and the mouth of the electrolyte tube. The two different cell configurations are shown in Figure 72.

### 5.3.2 Reference electrode performance in aluminum

Since the sensor is suspended in molten aluminum during operation, it is useful to measure the theoretical EMF between Mg-MgO and Al-Al<sub>2</sub>O<sub>3</sub> mixtures. In order to calculate this potential, the equilibrium oxygen partial pressures were first computed for both Mg-MgO ( $p_{\text{O}_2 (1)}$ ) and Al-Al<sub>2</sub>O<sub>3</sub> ( $p_{\text{O}_2 (2)}$ ) as described earlier. These were found to be  $10^{-51} \text{ atm}$  and  $10^{-47} \text{ atm}$  respectively. The theoretical EMF ( $E$ ) between the two electrodes was calculated using equation (10). Variation of this voltage with temperature is shown in Figure 73.

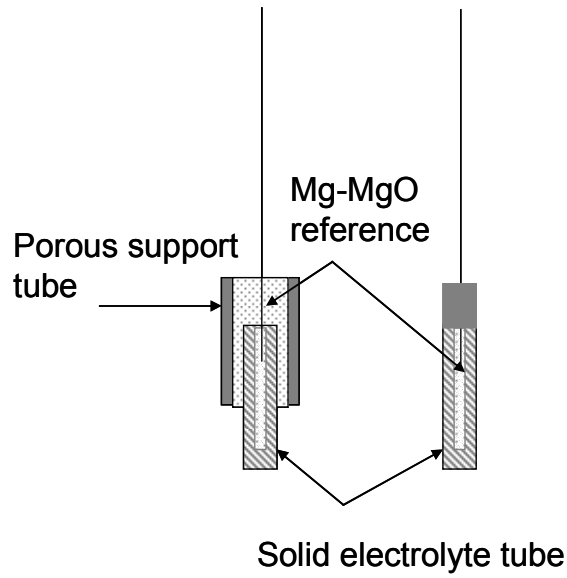


Figure 72 Schematic of cell configurations used to test sensors with Mg-MgO reference electrodes in argon.

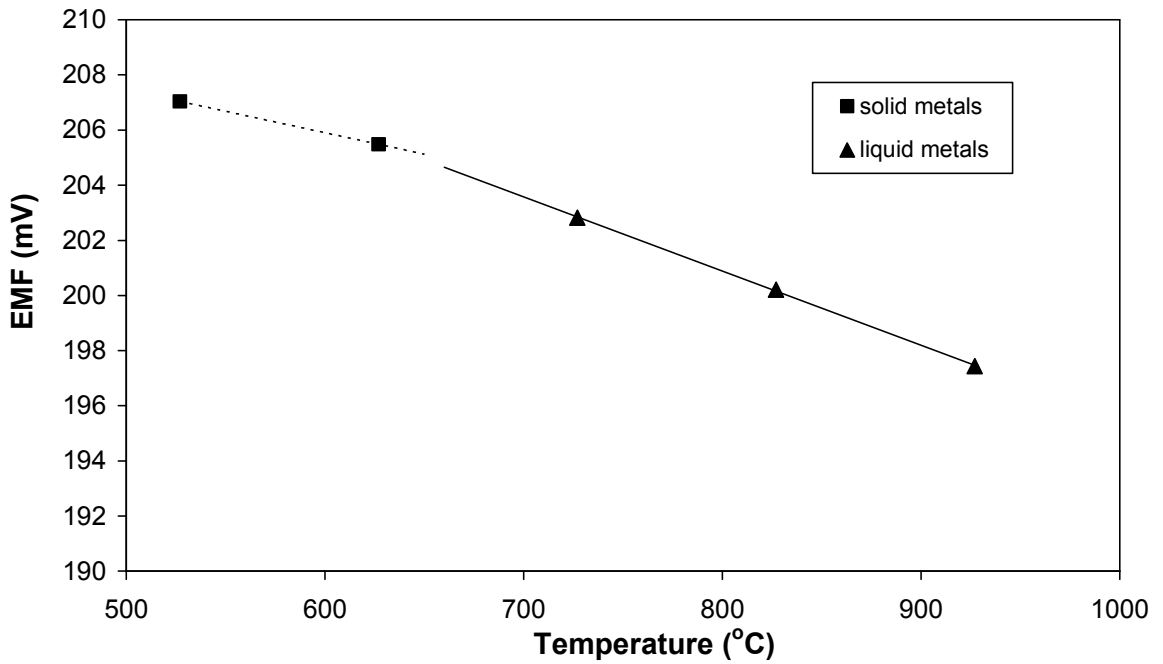


Figure 73 Theoretical voltage difference between Mg/MgO and Al/Al<sub>2</sub>O<sub>3</sub> reference electrodes calculated from thermochemical tables.



Experiments were conducted to estimate sensor performance in aluminum. The measured difference in EMF between a sensor containing Mg-MgO reference mixture, and another sensor containing Al-Al<sub>2</sub>O<sub>3</sub> reference mixture, both dipped in liquid aluminum, is shown in Figure 74. Although the data seems to have some scatter, an EMF measurement consistent with the theoretical calculation was observed. Since the working section of the sensor simply uses a lead wire inserted into the melt, the previous experiment was simplified by measuring the voltage between a sensor containing Mg-MgO reference mixture and aluminum. The measured EMF is shown in Figure 75. The data looks smoother and is observed to be ~300 mV. This matches well with the previous measurement indicating that the working potential can be measured using a wire dipped in aluminum without affecting sensor results.

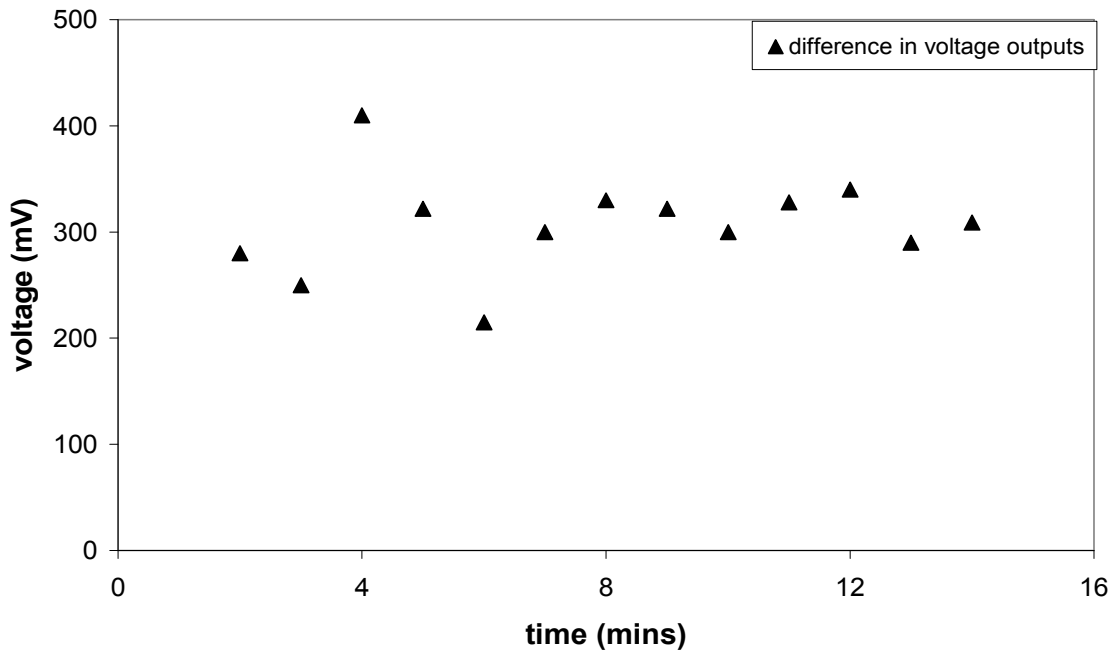


Figure 74 Difference in voltage output measured between sensors containing Mg/MgO and Al/Al<sub>2</sub>O<sub>3</sub> reference electrodes dipped in liquid aluminum.

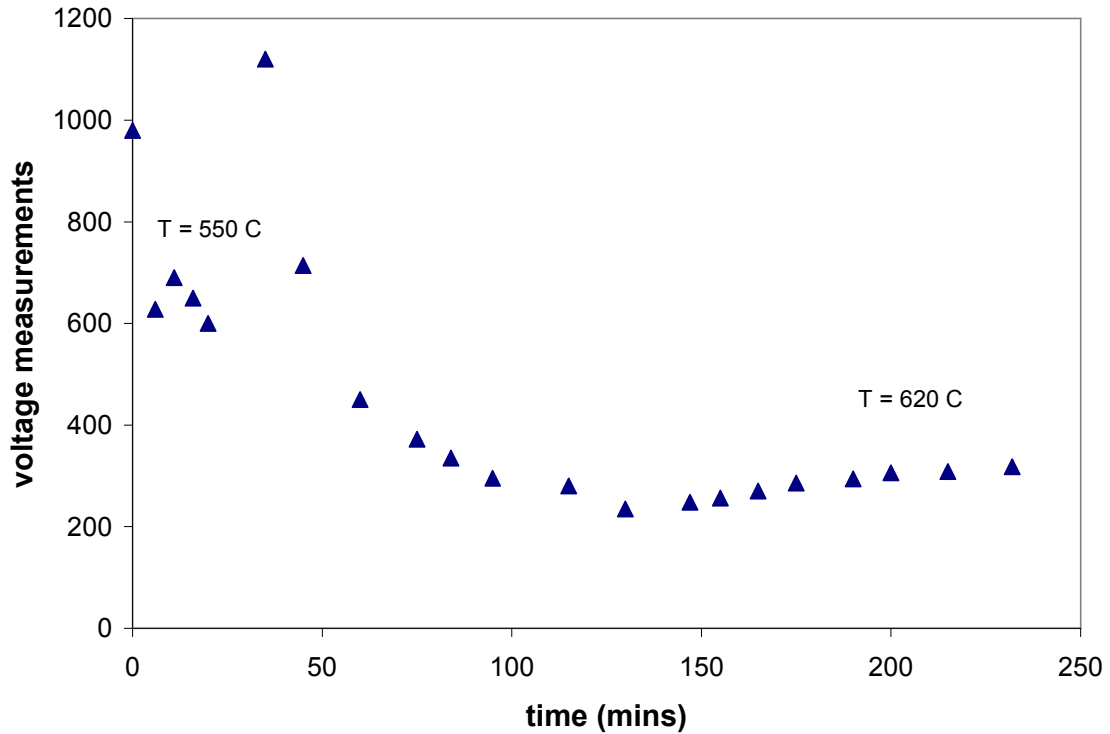
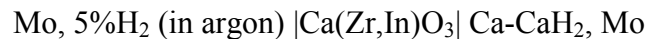


Figure 75 Voltage output from tubular sensor (Mg/MgO reference electrode) suspended in aluminum.

### 5.3.3. Hydrogen sensing using hydride based reference electrodes

Sensors with Ca-CaH<sub>2</sub> based reference electrodes were tested in Ar+5%H<sub>2</sub> environments.

The cell configuration for this system can be written as –



The conduction domain diagram shown in Figure 66 indicates that at high p<sub>H<sub>2</sub></sub> environments, Ca(Zr,In)O<sub>3</sub> materials act as proton conductors. A potential E, should then be setup because of the difference in hydrogen partial pressures on the opposite sides of the electrolyte. The hydrogen partial pressure established by the equilibrium between β-

Ca and  $\alpha$ -CaH<sub>2</sub> at 730°C was calculated as 0.0051 atm using data reported by Curtis et al.<sup>173</sup> The theoretical EMF expected across this cell was calculated as -98 mV by using equation (6).

The measured EMF from a device with Ca-CaH<sub>2</sub> reference electrodes tested in Ar+5%H<sub>2</sub> is shown in Figure 76. The voltage values appear to be stable around -100 mV, which corresponds well with the theoretical voltage calculated. This indicates that the sensor could measure the Nernstian potential for hydrogen species in hydrogen rich environments.

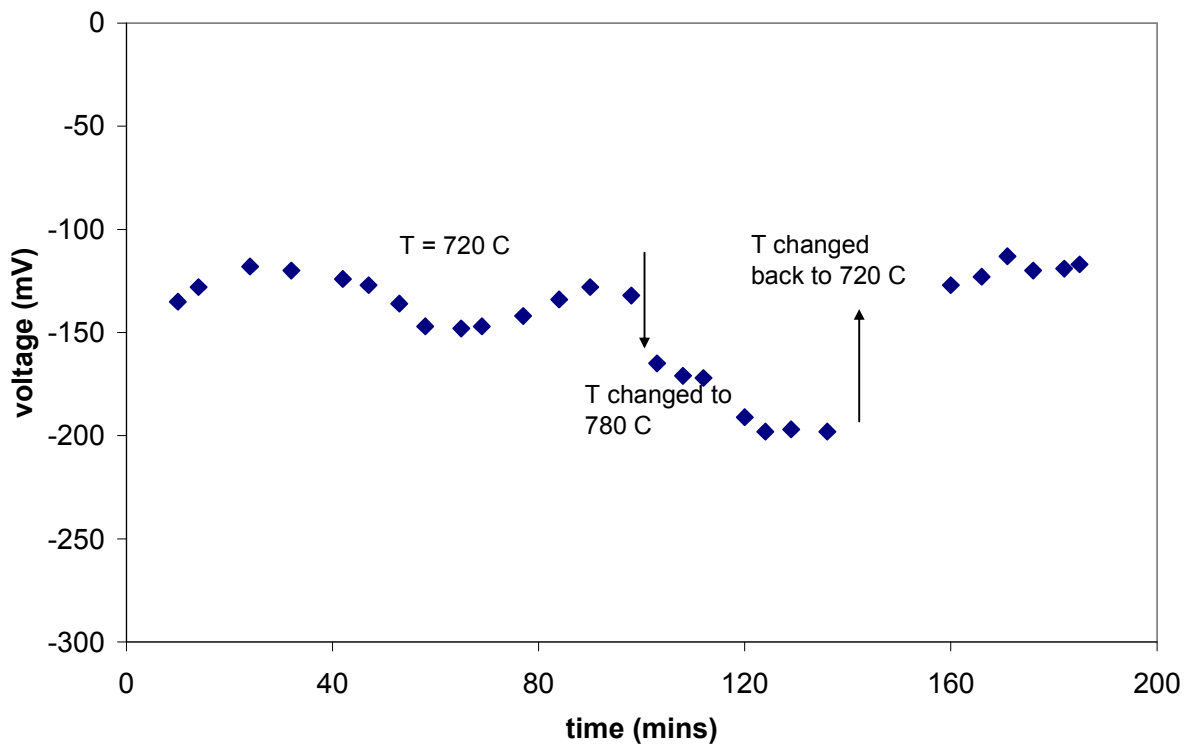


Figure 76 Voltage measured from a sensor using Ca-CaH<sub>2</sub> reference electrode tested in Ar+5%H<sub>2</sub> environment.

#### 5.3.4 Hydrogen sensing using oxide based reference electrodes

Past experiments have shown that the sensor is capable of acting as an oxygen concentration cell and a hydrogen concentration cell depending on the choice of reference electrode mixture and the species to be analyzed. If there is equilibrium between water, hydrogen and oxygen according to the reaction,



then the hydrogen partial pressures will be fixed for fixed water and oxygen partial pressures. A change in the hydrogen content could then be detected by measuring the voltage due to hydrogen partial pressure difference.

The oxygen and water partial pressures were fixed on both sides of the electrolyte by testing the sensor using Mg-MgO based reference electrodes in two different argon gas mixtures. Figure 77 shows the EMF measured from the sensor exposed to pure Ar and Ar+5%H<sub>2</sub> gas mixtures at 730°C. The sensor response after exposure to Ar+5%H<sub>2</sub> stabilizes at ~1.25 V. On switching the gas to pure argon, the EMF increases and stabilizes at ~1.57 V. This jump of ~320 mV was again reproduced when the gas was switched back to Ar+5%H<sub>2</sub>.

Since oxygen ion vacancies and/or protons may be responsible for conduction in these conditions it is difficult to calculate the theoretical EMF for this system without knowing the exact reactions at the electrode. The change in EMF, however, should be due to the change in hydrogen partial pressures as there should be no major change in

oxygen levels while switching between Ar and Ar+5% H<sub>2</sub>. The theoretical change in EMF was calculated as ~370 mV from equation (6) where p<sub>H<sub>2</sub></sub> in argon was taken as 10<sup>-5</sup> atm from the specifications listed in Table 5. The calculated value for the change in EMF corresponds well with that measured experimentally. This suggests that Mg-MgO based reference electrodes could be used to measure hydrogen concentrations using Ca(Zr,In)O<sub>3</sub> type materials as solid electrolytes.

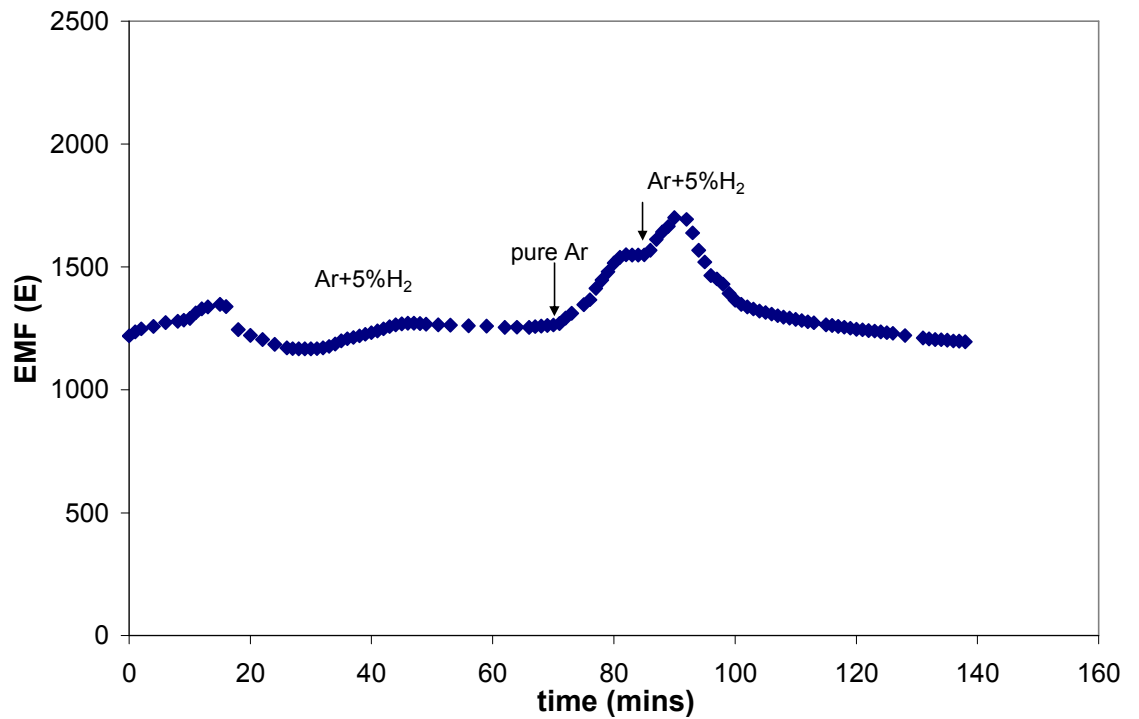


Figure 77 EMF measured from a Ca(Zr,In)O<sub>3</sub> based sensor with Mg-Mgo reference electrode exposed to Ar and Ar+5%H<sub>2</sub>. Sensor shows a change in response with hydrogen content that is both stable and reproducible.

### 5.3.5 Sensor tests in pilot plant conditions

To further investigate the use of hydrogen sensors based on oxide phase reference electrodes (Al/Al<sub>2</sub>O<sub>3</sub> and Mg/MgO), devices were tested in pilot plant conditions by inserting them in various aluminum alloy melts at CANMET. In three out of the four tests, similar voltage outputs were observed from both the Al/Al<sub>2</sub>O<sub>3</sub> and the Mg/MgO probes indicating that one of the probes may have failed. Post-test analysis of the failed probes showed cracks in the alumina support tube through which liquid aluminum had entered the probe and probably caused failure. This may have been due to the high thermal shock during insertion. All four tests, however, showed an almost immediate response to degassing.

The sensor output in Alloy 356 is shown in Figure 78 along with the results from the periodic AlScan™ measurements. RPT samples taken from the melt before and after degassing (shown in Figure 79) show a significant reduction in porosity after degassing. As the precise auxiliary reactions relating the oxygen partial pressure fixed by the reference mixture to the hydrogen partial pressures are not known, the reference hydrogen pressures established by these electrodes could not be calculated. However, the change in sensor output in response to degassing can be used to evaluate the sensor response.

Table 6 summarizes the sensor outputs and AlScan™ measurements before and after degassing for each of the four melts. The hydrogen partial pressure,  $p_{H_2}$ , measured by the electrochemical sensor can be related to the hydrogen solubility,  $S$ , measured by the AlScan™ analyzer using equation (4), where the standard solubility between 700°C and 850°C is given by,

$$\log S_o = \frac{-2980}{T} + 3.07 \quad (21)$$

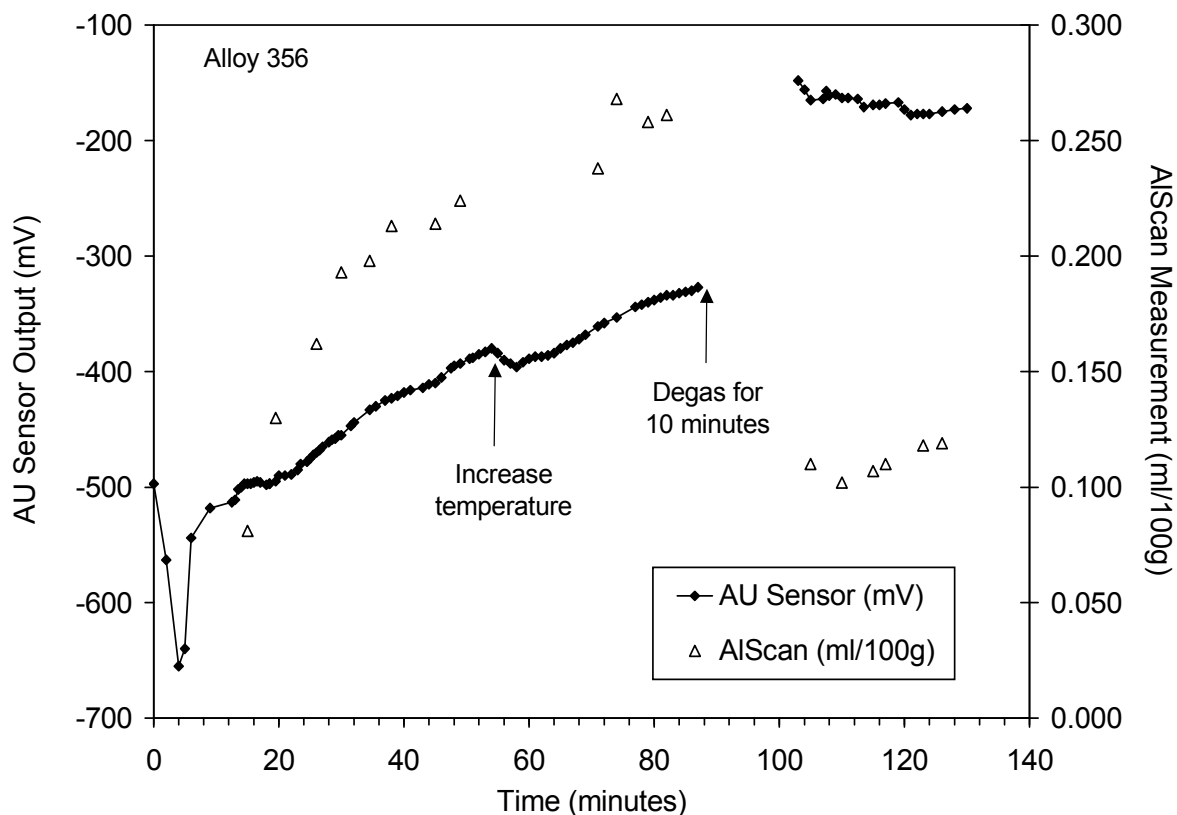


Figure 78 Simultaneous measurements made by sensor and AlScan in Aluminum 356 melt at CANMET.

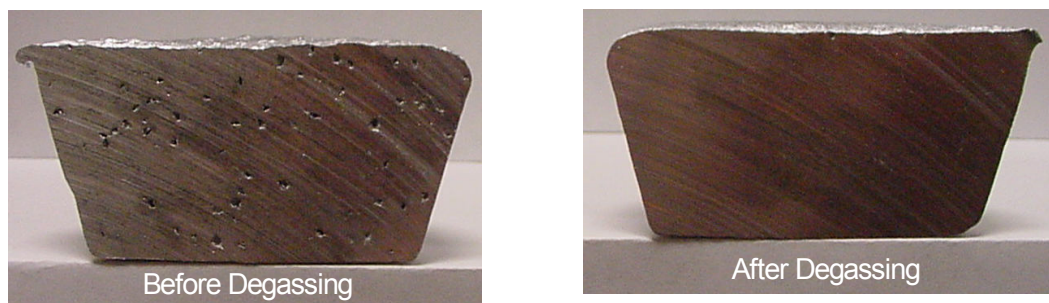


Figure 79 Cross-section of reduced pressure test samples taken before and after degassing showing change in porosity.

The values of alloy correction factors (CF(A)) for the different melts are also listed in Table 6. These numbers represent the activities of hydrogen in the respective aluminum alloys. Equations 10, 11 and the results from Table 6 were used to calculate the hydrogen partial pressures corresponding to the change in gas content determined by AlScan™ measurements.

Alloy		Sensor Output (mV)		AlScan (ml/100mg)	
Designation	CF(A)	Before	After	Before	After
356	0.82	-327	-161	0.261	0.11
535	1.3	114	25	0.407	0.173
319	0.69	-166	-13	0.179	0.082
Pure aluminum	1	-229	-195	0.233	0.152

Table 6 Sensor and AlScan outputs observed in 4 different Al alloy melts at CANMET.

The voltage output corresponding to the change in hydrogen content measured by AlScan™ was then calculated using the Nernst equation according to -

$$\Delta E_{\text{degas}} = E_{\text{before}} - E_{\text{after}} \quad (22)$$

$$= \left\{ \frac{RT}{2F} \ln pH_{2_{\text{before}}} - \frac{RT}{2F} \ln pH_{2_{\text{ref}}} \right\} - \left\{ \frac{RT}{2F} \ln pH_{2_{\text{after}}} - \frac{RT}{2F} \ln pH_{2_{\text{ref}}} \right\} \quad (23)$$

or,

$$\Delta E_{\text{degas}} = \frac{RT}{2F} \ln \frac{pH_{2_{\text{before}}}}{pH_{2_{\text{after}}}} \quad (24)$$



The actual output of the electrochemical sensor is compared with these calculations in Figure 80. The two results scale together indicating that the sensor output is proportional to the change in hydrogen content. In experiments involving aluminum alloys, the magnitude of the change in voltage from the electrochemical sensor calculated using the value of  $n$  as 2 (equation 14) is higher than that predicted from the AlScan™ measurements. The measured change in voltage however matches reasonably well with the Alscan measurements in the case of pure aluminum melts.

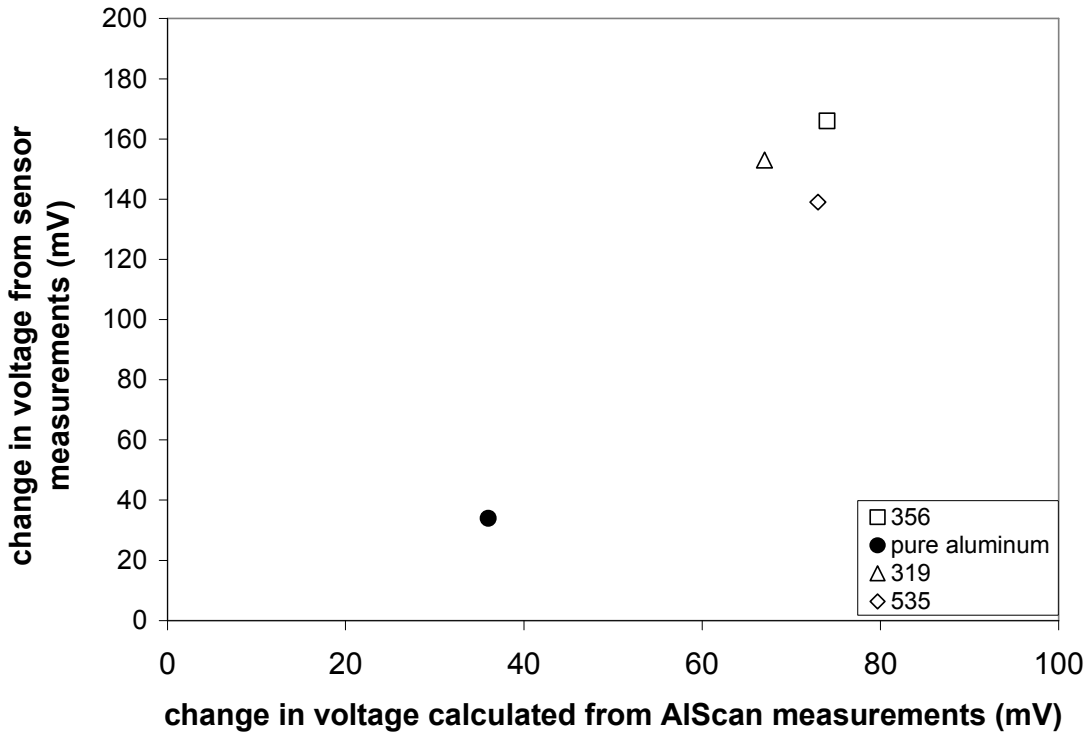


Figure 80 Comparison of voltage change caused due to degassing calculated from AlScan measurements and sensor outputs from 4 the different alloy melts.

Sensor responses from tests at CANMET showed that the sensor responded considerably well to degassing with voltage outputs in the expected ranges. However, several problems with mechanical and reference electrode stability were encountered. Four out of a total of eight probes failed the initial insertion into the melt. Investigation of the probe elements showed cracks in the alumina support tube presumably due to the high thermal shock. To overcome this problem, samples of porous ceramic tubes were obtained from Fairey Industrial Ceramics, UK. Laboratory tests conducted with sensors using the porous tubes indicated improvement in device stability as the support tubes were not found to crack during insertion. The alumina tubes that were used for insulating the lead wires were replaced with insulative ceramic fibers to help in easier handling of the device.

Problems with reference electrode stability were also observed with the sensor response drifting with time. This could be due to inadequate sealing of the reference mixture from the environment. The sensors tested in CANMET used a water based ceramic seal (Ceramabond, Aremco Ceramics) that is not gas tight. This could have allowed oxygen and water vapor to enter the reference continuously which would disturb the equilibrium established. The observed drift in measured potential can be possibly attributed to this occurrence.

## 6. CONCLUSIONS

### 6.1. Ca(Zr,In)O<sub>3</sub> powder synthesis

Ca(Zr,In)O<sub>3</sub> powders were synthesized using both solid oxide mixing and oxalate co-precipitation techniques. Powders prepared using the solid oxide method were found to contain CaIn<sub>2</sub>O<sub>4</sub> as a secondary phase after calcination at 1400°C. Single-phase CaZr<sub>0.9</sub>In<sub>0.1</sub>O<sub>2.975</sub> powders were primarily obtained from the decomposition of oxalate precursors at the same temperature. Indium solubility in these Ca(Zr,In)O<sub>3</sub> samples was found to be between 0-5 %. Smaller, better-dispersed precursor particles were produced by using PEG during the co-precipitation process. PEG addition or precursor ball-milling, both helped lower reaction times and temperatures needed for complete CaZrO<sub>3</sub> formation.

### 6.2. Electrical characterization of Ca(Zr,In)O<sub>3</sub> materials

Sample resistance and capacitance values were obtained from impedance spectroscopy and conductivity measurements. Bulk conduction in Ca(Zr,In)O<sub>3</sub> was found to be homogenous with a Debye-type relaxation, while grain boundaries showed heterogeneity. Bulk capacitances measured in air remained invariant with temperature. Undoped CaZrO<sub>3</sub> was found to be a p-type conductor ( $E_a = 1.2$  eV) in air with conductivity  $\sim 10^{-5}$  Scm<sup>-1</sup> at 900°C. Doping with indium increased sample conductivity

by 2-3 orders of magnitude. In-doped  $\text{CaZrO}_3$  was found to be a proton conductor ( $E_a = 0.74$  eV) in air, argon+ $\text{H}_2\text{O}$  and a p-type conductor ( $E_a = 0.91$ eV) in argon. Mg-doping was found to increase conductivity in  $\text{CaZrO}_3$  by 1 order of magnitude.

### 6.3. Hydrogen sensor testing

$\text{Ca}(\text{Zr},\text{In})\text{O}_3$  based potentiometric sensors with Mg-MgO and Ca- $\text{CaH}_2$  reference electrodes were fabricated successfully for application in molten aluminum. Laboratory scale testing of devices with Mg-MgO reference electrodes showed reliable voltage measurements in argon and aluminum environments. These sensors also measured a reproducible voltage change when switched between Ar and Ar+5%  $\text{H}_2$ . Ca- $\text{CaH}_2$  reference electrodes, when exposed to 5%  $\text{H}_2$ , generated a voltage matching the Nernst equation. Sensors with tubular and pellet shaped solid electrolyte elements generated a similar EMF in argon. Faster response times were measured in the case of tubular designs.

Pilot plant tests showed the sensor to respond to hydrogen content changes in various aluminum alloy melts. The voltage changes measured were of the same order as that shown by the commercial AlScan hydrogen sensor. Poor thermal shock resistance of the dense support tube used in these tests, affected sensor performance in some cases. This was improved on by using porous support tubes. Seals were found to be a problem as consistent reference electrode drift was measured during some experiments.

## 7. FUTURE WORK

### **Sensor development and commercialization**

The hydrogen sensor proposed is suitable for further development and commercialization. A series of further pilot plant tests involving simultaneous measurements along with Alscan systems could confirm the sensor's applicability in industry type settings. Several foundries have a long feed line through which molten aluminum is flowed prior to casting. Sensors could be placed at strategic locations to estimate the hydrogen content along the feed line. This information could then be sent to an online degassing system that would degas until the sensor measures hydrogen levels below the permissible limit. By coupling hydrogen sensors with the degassing system, an automatic feedback controlled degassing system can thus be developed. This would enable continuous monitoring and control of the melt quality at all junctures during the casting process. Such a system would have huge commercialization value. A simple block diagram for such a feedback control system is shown in Figure 81.

Further advances in sensor sealant are necessary to ensure device success. Since the reference electrode section of the sensor must be kept isolated from the outside, gas tight sealing is important. Common gas tight high temperature sealants are usually based on glass or glass ceramics. These materials usually contain silica which decomposes at the low oxygen partial pressures prevalent in the melt. These also must be cured at high temperatures before the actual use, which might affect the performance of the reference

material. Ceramic based adhesives are convenient in that they can be cured at low temperatures (~200F). Ceramic based adhesives are sometimes porous and not gas-tight. A hermetic seal can be achieved with these materials by first making the bond using an alumina based adhesive (Aremco 569) and then applying a uniform coating of the binder over the entire bond line to seal the pores.<sup>174</sup>

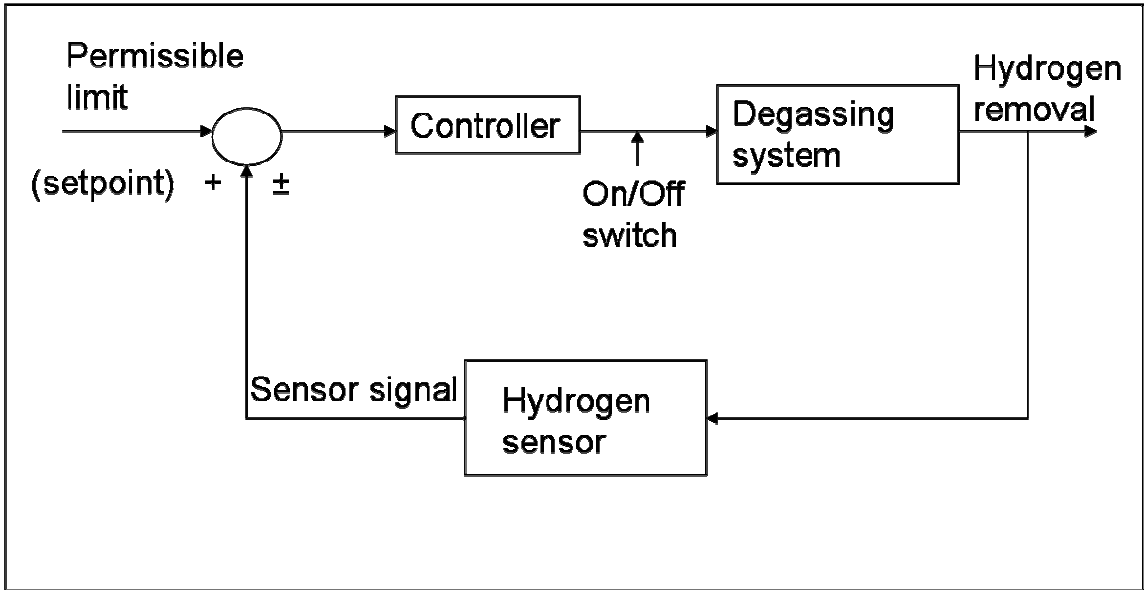


Figure 81 A simple block diagram for a feedback control system that can be designed to optimize hydrogen content in molten aluminum. The control system couples the proposed hydrogen sensor with a commercial degassing system.

**Electrical characterization**

Using metal-metal oxide mixtures to fix oxygen partial pressures can help characterize electrical ceramics at hitherto unexplored conditions. Figure 82 shows a plot of the oxygen partial pressures fixed by various metal-metal oxide combinations and gas ratios. By appropriate selection, the same  $pO_2$  can be established using both methods. The defect properties of a material should remain the same at a certain  $pO_2$  irrespective of

whether the partial pressure is fixed using a metal-metal oxide or a gas mixture. Therefore, electrical characterization using the two treatments could help prove the technique's validity.

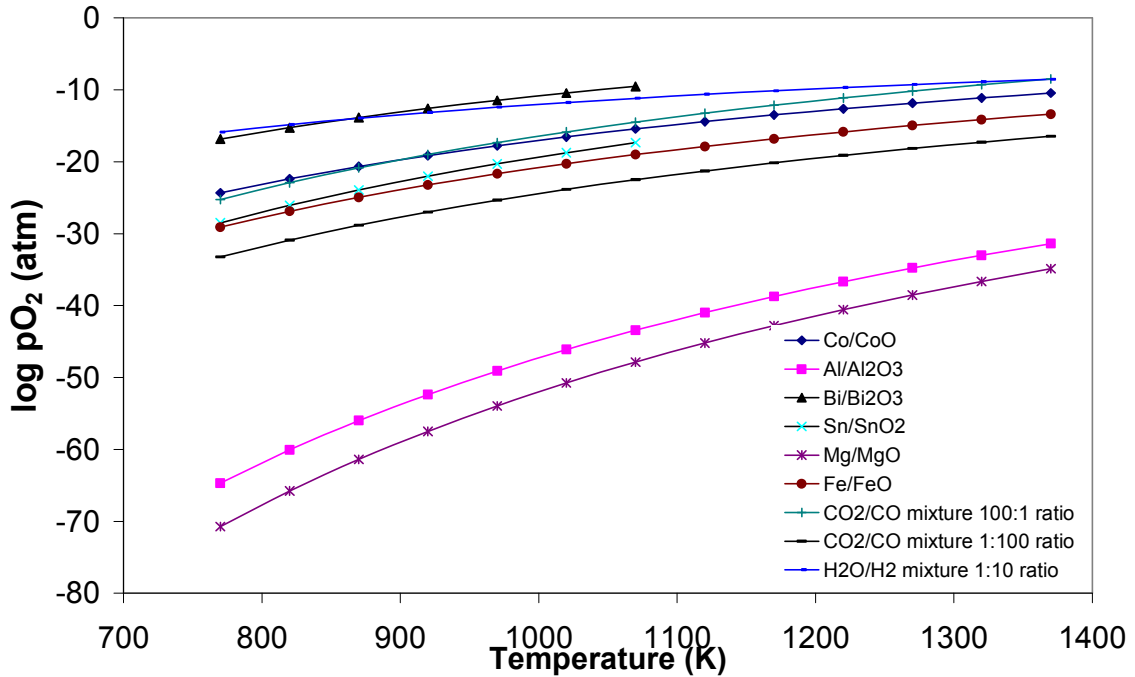


Figure 82 Equilibrium oxygen partial pressures established by using metal-metal oxide mixtures and H<sub>2</sub>O-H<sub>2</sub>, CO-CO<sub>2</sub> gas mixtures as a function of temperature.

Since metals like aluminum and magnesium have a high affinity for oxygen, the ability to fully retain the two-phase mixture for the entire experiment could be a challenge. In the present investigation, metallic powders were melted to form the metal-metal oxide mixture. Since there is always trapped oxygen between the powders, these were found to react to form the oxide. This problem could be considerably reduced by melting small metal ingots of the respective metal at the opposite sides of the electrolyte.

Upon verification, the technique could prove useful in characterizing the defect properties of various systems. For example, the formation of Magnelli phases from rutile

(TiO<sub>2</sub>) can be characterized by exposing samples to molten aluminum. This could be useful for estimating the defect transport mechanisms responsible for oxidation in titanium aluminide alloys.

### **Structural characterization**

Investigation of indium solubility in CaZrO<sub>3</sub> – Although In-doped CaZrO<sub>3</sub> has been the material of choice for various high temperature electrochemical applications, a phase diagram for this system is not yet available. The present work suggests dopant solubility between 0 - 5% based on x-ray diffraction results from the prepared samples. Further investigation of this system could be carried out by preparing samples with dopant levels between 0 - 5 %. Precise lattice parameter measurements using x-ray diffraction could then be used to arrive at a closer estimate of the dopant solubility.

Structural investigation of the proton site using neutron diffraction – There is not much literature on the investigation of the structural properties of Ca(Zr,In)O<sub>3</sub> materials using neutron powder diffraction. This technique has excellent sensitivity towards light elements and is ideal to detect features like protonation and oxygen vacancy ordering in perovskite materials. According to Knight,<sup>175</sup> high temperature measurements made in samples with different indium concentrations could help separate atomic displacement parameters from the static displacements induced on doping an aliovalent ion onto the octahedral site. Knight also suggests that since indium is a significant neutron absorber, high data collection times should be expected and the data should be corrected for absorption effects.



## **Development of Mg-doped CaZrO<sub>3</sub> materials as solid electrolytes**

The presence of In-rich secondary phases like CaIn<sub>2</sub>O<sub>4</sub> might affect the electrical properties of In-doped CaZrO<sub>3</sub> samples. Mg-doped CaZrO<sub>3</sub> materials could be investigated as an attractive alternate. This type of sensor design could simply utilize commercially available undoped CaZrO<sub>3</sub> as the solid electrolyte. Since the sensor device uses Mg based reference electrodes, CaZrO<sub>3</sub> could then interact with the Mg at high temperatures to form the doped material. A small amount of the dopant should be sufficient to improve the conductivity of CaZrO<sub>3</sub> for use in various high temperature applications. It should, however, be noted that at the operation temperature of the sensor (~700°C), long times may be necessary for the dopant (Mg<sup>2+</sup>) to diffuse completely throughout the solid electrolyte material (CaZrO<sub>3</sub>).

## **Ceramic synthesis and processing**

Mixed hydroxide precursors for perovskite formations – Since the oxalate precipitation process used does not yield mixed oxalates, other alternate routes of synthesis could be investigated. A simple solution would be to study the precipitation of mixed (Ca, Zr, In) hydroxides from the aqueous solution. Hydroxide based precursors would decompose to form perovskite through fewer reaction steps when compared to oxalate precursors. This might improve process yields. Hydrothermal synthesis might also be an attractive option that could be studied in this regard.

Optimization of powder calcinations conditions – The formation of solid electrolyte tubes and pellets involves oxalate decomposition by calcination followed by sintering of the powder compacts. While high sintering temperatures are usually required to produce dense samples, the reaction conditions for precursor calcination vary according to the

material. High calcination temperatures may produce powders with large particles that may not sinter to high density. Precursor powders heated at lower calcination temperatures on the other hand may not decompose well enough so that reactions continue to occur during the sintering stage. This again reduces the density of the sintered product. It could therefore be useful to estimate the precise calcination conditions (temperature, time) so as to produce the best results.

## REFERENCES

- 
- <sup>1</sup> K.J. Anderson. "Against the Elements: Sir Humphry Davy," *MRS Bull.* **14** [1] 74 (Jan 1989)
- <sup>2</sup> <http://www.world-aluminum.org/iai/stats/index.asp>, as obtained on 08/30/06
- <sup>3</sup> J.E. Hatch, *Aluminum: Properties and Physical Metallurgy*, American Society for Metals, Metals Park OH (1984)
- <sup>4</sup> L.F. Mondolfo, *Aluminum Alloys: Structure and Properties*, Butterworths, London and Boston (1976)
- <sup>5</sup> P. Rohatgi, "Cast Aluminum-Matrix Composites for Automotive Applications", *JOM* **43** [4] 10-15 (1991)
- <sup>6</sup> J. Han, K. Yamazaki and S. Nishiyama, "Optimization of Crushing Characteristics of Triangulated Aluminum Beverage Cans", *Struct. Multidisc. Optim.* **28**, 47-54 (2004)
- <sup>7</sup> F.M. Mazzolani, *Aluminum Alloy Structures*, Pub. E and FN Spon Publishers pp. 34 (1995)
- <sup>8</sup> J.R. Kissell and R. L. Ferry, *Aluminum Structures*, John Wiley and Sons pp. 5 (2002)
- <sup>9</sup> A.J. Pansini, *Power Transmission and Distribution*, 2<sup>nd</sup> ed. Fairmont Press Lilburn, GA pp.198 (2005)
- <sup>10</sup> W. M. Rasmussen, "The Dilemma of Assessing your Aluminum Melt's Cleanliness" Ed-M.J. Lessiter, *Mod. Cast.* 45-48 (1996)

- 
- <sup>11</sup> P.N. Crepeau, “Molten Aluminum Contamination: Gas, Inclusions and Dross”, *Mod. Cast.* **87** [7] 39-41 (July 1997)
- <sup>12</sup> S. K. Das, W.J. Long III, H.W. Hayden, J.A.S. Green and W. Hunt Jr., “Energy Implications of the Changing World of Aluminum Metal Supply”, *JOM* **56** [1] 14-17 (2004)
- <sup>13</sup> R. Monroe, “Porosity in Castings”, *Mod. Cast.*, 1-28, (September 2005)
- <sup>14</sup> X.G. Chen and S. Engler, “Formation of Gas Porosity in Aluminum Alloys”, 98<sup>th</sup> Annual Meeting of the American Foundrymen’s Society; Hamilton; CA, 673-682 (1994)
- <sup>15</sup> S.T. McClain, “A Study of Porosity Quantification Techniques and Pore Morphology in Aluminum Castings”, M.S. Thesis, Mississippi State University (1997)
- <sup>16</sup> J.G. Kauffman and E.L. Rooy, *Aluminum Alloy Castings: Properties, Processes and Applications*, ASM International, Metals Park OH (2004)
- <sup>17</sup> Q. G. Wang, D. Apelian and D.A. Lados, “Fatigue Behavior of A356-T6 Aluminum Cast Alloys. Part I. Effect of Casting Defects”, *J. Light Metals* **1** [1] 73-84 (2001)
- <sup>18</sup> A.M. Samuel and F.H. Samuel, “Various Aspects Involved in the Production of Low-Hydrogen Aluminum Castings”, *J. Mat. Sci.* **27** [24] 6533-63 (1992)
- <sup>19</sup> C. Meric, “Physical and Mechanical Properties of Cast Under Vacuum Aluminum Alloy 2024 Containing Lithium Additions”, *MRS Bull.* **35** [9] 1479-94 (2000)
- <sup>20</sup> D. P. Kanicki and W.M. Rasmussen, “Processing Molten Aluminum. II. Cleaning Up Your Metal”, *Mod. Cast.* **80** [2] 55-58 (1990)
- <sup>21</sup> R. A. Rapp, “The Closed-Circuit Degassing of Liquid Aluminum by Argon”, *JOM* **49** [5] 16-19 (1997)

- 
- <sup>22</sup> Qian Fu, Dong Xu, and James W. Evans, "Chlorine Fluxing for Removal of Magnesium from Molten Aluminum: Part I. Laboratory-Scale Measurements of Reaction Rates and Bubble Behavior," *Met. Trans. B* **29B** [5] 971-978 (1998)
- <sup>23</sup> J. Botor, "Kinetics of Hydrogen Degassing of Molten Aluminum by Purge Gases," *Aluminum* **56** [8] 519-522 (1980)
- <sup>24</sup> P. Waite and R. Thiffault, "The Alcan Compact Degasser: A Trough-Based Aluminum Treatment Process. Part I: Metallurgical Principles and Performance," *Light Metals 1996 Conference Proceedings at the 125<sup>th</sup> TMS/AIME Annual Meeting*, Anaheim, CA, 1001-1005 (1996)
- <sup>25</sup> J. W. Fergus, "Sensors for Monitoring the Quality of Molten Aluminum During Casting," *J. Mater. Engg. Perf.* **14** [2] 267-275 (2005)
- <sup>26</sup> M.M. Makhlof, L. Wang, and D. Apelian, *Measurement and Removal of Hydrogen in Aluminum Alloys*, Des Plaines, IL, AFS, 1998, 29-38.
- <sup>27</sup> P.D. Hess, "Measuring Hydrogen in Aluminum Alloys," *J. Met.* **25** [10] 46-50 (1973)
- <sup>28</sup> X.G. Chen, F.J. Klinkenberg, S. Engler, L. Heusler, "Comparing Hydrogen Testing Methods for Wrought Aluminum" *JOM* **46** [8] 34-38 (1994)
- <sup>29</sup> D.A. Anderson, D.A. Granger and R.R. Avery, "The Alcoa Telegas IITM Instrument", *Light Metals* (Warrendale, PA) 769-773 (1990)
- <sup>30</sup> H. Liu, M. Bouchard and L. Zhang, "An Experimental Study of Hydrogen Solubility in Liquid Aluminum," *J. Mat. Sci.*, **30** [17] 4309-15 (1995)
- <sup>31</sup> J.W. Fergus, "Using Chemical Sensors to Control Molten Metal Processing," *JOM-e*, **52** [10] (2000)

- 
- <sup>32</sup> *Solid Electrolytes: General Principles, Characterization, Materials, and Applications*, P. Hagenmuller and W. Van Gool (Ed), Academic, NY (1978)
- <sup>33</sup> R. Gee and D.J. Fray, "Instantaneous Determination of Hydrogen Content in Molten Aluminium and Its Alloys," *Met. Trans.* **9B** 427-430 (1978)
- <sup>34</sup> H. Iwahara, H. Uchida, K. Ogaki, H. Nagato, "Nernstian hydrogen sensor using BaCeO<sub>3</sub>-based, proton-conducting ceramics operative at 200 degrees -900 degrees C," *J. Electrochem. Soc.* **138** [1] 295-299 (1991)
- <sup>35</sup> S. Zhuiykov, "Hydrogen Sensor Based on a New Type of Proton Conductive," *Ceramic. Int. J. Hydrogen Energy*, **21** [9] 749-759. (1996),
- <sup>36</sup> T. Yajima, K. Koide, H. Takai, N. Fukatsu, H. Iwahara, "Application Of Hydrogen Sensor Using Proton Conductive Ceramics as a Solid Electrolyte to Aluminum Casting Industries," *Solid State Ionics* **79** 333-337 (1995)
- <sup>37</sup> M. Zheng and X. Zhen, "Hydrogen Probe Equipped with SrCeO<sub>3</sub>-Based Proton Conductor and Ca/CaH<sub>2</sub> Reference Electrode," *Metall. Mater. Trans. B*, **24B** 789-794 (1993)
- <sup>38</sup> V. Krishnan, J.W. Fergus, F. Fasoyinu, "Solid electrolyte based hydrogen sensor for molten aluminum," in *Advances in Aluminum Casting Technology II, Proceedings from Materials Solutions Conference 2002*, International Aluminum Casting Technology Symposium, 2nd, Columbus, OH, United States, Oct. 7-9, 2002 (2002), 155-158.
- <sup>39</sup> *The CRC Handbook of Solid State Electrochemistry*, edited by P.J. Gellings, H.J.M. Bouwmeester, CRC Press, Boca Raton FL (1997)

- 
- <sup>40</sup> T.H. Etsell and S.N. Flengas, "The Electrical Properties of Solid Oxide Electrolytes," *Chem. Rev.* **70** [3] 339-76 (1970)
- <sup>41</sup> P.G. Bruce, *Solid State Electrochemistry*, Cambridge University Press, August 1997
- <sup>42</sup> D.J. Fray, "Potentiometric gas sensors for use at high temperatures," *Mater. Sci. Tech.* **16** 237-242 (2000)
- <sup>43</sup> S. Akbar, P. Dutta and C. Lee, "High-Temperature Ceramic Gas Sensors: A Review," *Int. J. Appl. Ceram. Technol.*, **3** [4] 302-311 (2006)
- <sup>44</sup> R. Ramamoorthy, P.K. Dutta and S.A. Akbar, "Oxygen Sensors: Materials, Methods, Designs and Applications," *J. Mat. Sci.*, **38**, 4271-4282 (2003)
- <sup>45</sup> J-H. Lee, "Review on Zirconia Air-Fuel Ratio Sensors for Automotive Applications," *J. Mat. Sci.*, **38**, 4247-4257 (2003)
- <sup>46</sup> W. Weppner, "Advanced Principles of Sensors Based on Solid State Ionics," *Mater. Sci. Engg B*, **15**, (1992) 48.
- <sup>47</sup> G. Alberti, A. Carbone, R. Palombari, "Oxygen potentiometric sensors based on thermally stable solid state proton conductors: a preliminary investigation in the temperature range 150-200 °C," *Sensors and Actuators B*, **86**, 150-54 (2002)
- <sup>48</sup> G. M. Kale, R. Kurchania, *Ceramic Transactions (1999)*, **92** (*Electrochemistry of Glass and Ceramics*), 195-220
- <sup>49</sup> E.D. Bartolomeo, E. Traversa, M. Baroncini, V. Kotzeva and R. V. Kumar, "Solid State Ceramic Gas Sensors Based on Interfacing Ionic Conductors with Semiconducting Oxides," *J. Eu. Ceram. Soc.*, **20** [16] 2691-99 (2000)

- 
- <sup>50</sup> N. Miura, G. Lu and N. Yamazoe, "Progress in Mixed-Potential Type Devices Based on Solid Electrolyte for Sensing Redox Gases," *Solid State Ionics* **136-137**, 533-542 (2000)
- <sup>51</sup> W.L. Worrell, Q. Liu, "Development of an Extended-Life Oxygen Sensor for Iron and Steel Melts," *Solid State Ionics* **40-41**, 761-763 (1990)
- <sup>52</sup> Q. Lin, "The development of high temperature electrochemical sensors for metallurgical processes," *Solid State Ionics* **86-88**, 1037-1043 (1996)
- <sup>53</sup> A.R. Romero, J. Harkki, and D. Janke "Oxygen and carbon sensing in iron- oxygen - carbon and Fe-O-C-Xn melts at elevated carbon contents," *Steel Research* **57** [12] 636-44 (1986)
- <sup>54</sup> E.T. Turkdogan, R.J. Fruehan "Review Of Oxygen Sensors For Use In Steelmaking And Of Deoxidation Equilibriums," *Canadian Metallurgical Quarterly* **11** [2] 371-84 (1972)
- <sup>55</sup> M. Iwase and Y. Waseda, "Recent Developments in Electrochemical Oxygen Sensors Used for Iron and Steelmaking," *High Temp. Mater. Proc.* **7** [2-3] 123-131 (1986)
- <sup>56</sup> K.T. Jacob and S.K. Ramasesha, "Design of Temperature-Compensated Reference Electrodes for Non-Isothermal Galvanic Sensors," *Solid State Ionics* **34**, 161-166 (1989)
- <sup>57</sup> Y.Du, Z.P. Jin and P.Y. Huang, "Thermodynamic Calculation of the Zirconia–Calcium System," *J.Am. Ceram. Soc.*, **75** [11] 3040-3048 (1992)
- <sup>58</sup> P. Duran, P. Recio and J.M. Rodriguez, "Comment on "The Calcium–Zirconia Phase Diagram Revisited: Stability of the Ordered Phases  $\delta_1$  and  $\delta_2$ ," *J. Am. Ceram. Soc.* **75** [3] 731-732 (1992)



- 
- <sup>59</sup> R. M. Dickerson and A. H. Heuer, "Reply to "Comment on 'The Calcia–Zirconia Phase Diagram Revisited: Stability of the Ordered Phases  $\phi_1$  and  $\phi_2$ ,"" *J. Am. Ceram. Soc.* **75**, 733 (1992)
- <sup>60</sup> Fig Zr-061 in "Phase Diagrams for zirconium and zirconia systems", edited by H.M. Ondik and H.F. McMurdie (American Ceramics Society, Westerville, OH, 1998).
- <sup>61</sup> Fig Zr-065 in "Phase Diagrams for zirconium and zirconia systems", edited by H.M. Ondik and H.F. McMurdie (American Ceramics Society, Westerville, OH, 1998).
- <sup>62</sup> V.P. Dravid, C.M. Sung, M.R. Notis and C.E. Lyman, "Crystal Symmetry and Coherent Twin Structure of Calcium Zirconate," *Acta Crystallogr.* **B45**, 218 (1989)
- <sup>63</sup> H.J.A Koopmans, G.M.H van de Velde, P.J. Gellings, "Powder Neutron Diffraction Study of the Perovskites  $\text{CaTiO}_3$  and  $\text{CaZrO}_3$ ," *Acta Crystallogr.* **C39**, 323 (1983)
- <sup>64</sup> C. Shi, M. Yoshino and M. Morinaga, "First-principles Study of Protonic Conduction in In-doped  $\text{AZrO}_3$  (A=Ca, Ba, Sr)," *Solid State Ionics* **176**, 1091-1096 (2005)
- <sup>65</sup> M.S. Islam, R.A. Davies and J.D. Gale, "Proton Migration and Defect Interactions in the  $\text{CaZrO}_3$  Orthorhombic Perovskite : Quantum Mechanical Study," *Chem. Mater.* **13** 2049-55 (2000)
- <sup>66</sup> V.M. Orera, C. Peccharoman, J.I. Pena, R.I. Merino and C.J. Serna, "Vibrational Spectroscopy of  $\text{CaZrO}_3$  Single Crystals," *J. Phys.: Condens. Matter* **10** 7501-7510 (1998)
- <sup>67</sup> H. Zheng, I.M. Reaney, G.D.C. Gyorgyfalva, R. Ubic, J. Yarwood, M.P. Seabra and V.M. Ferreira, "Raman Spectroscopy of  $\text{CaTiO}_3$ -based Solid Solutions," *J. Mater. Res.*, **19** [2] 488-95 (2004)

- 
- <sup>68</sup> V.M. Orera, J.I. Pena, R.I. Merino, J.A. Lazaro, J.A. Valles and M.A. Rebolledo, "Prospects of New Planar Optical Waveguides Based on Eutectic Microcomposites of Insulating Crystals: The  $ZrO_2(c)$ - $CaZrO_3$  Erbium Doped System," *Appl. Phys. Lett.* **71** [19] 2746-48 (1997)
- <sup>69</sup> R.I. Merino, R.A. Pardo, J. I. Pena, G.F. De la Fuente, A. Larrea and V.M. Orera, "Luminescence Properties of  $ZrO_2$ - $CaO$  Eutectic Crystals With Ordered Lamellar Microstructure Activated with  $Er^{3+}$  Ions," *Phys. Rev. B* **56** [17] 10907-915 (1997)
- <sup>70</sup> Y. Suzuki, H.J. Hwang, N. Kondo and T. Ohji, "In Situ Processing of a Porous Calcium Zirconate/Magnesia Composite with Platinum Nanodispersion and Its Influence on Nitric Oxide Decomposition," *J. Am. Ceram. Soc.*, **84** [11] 2713-15 (2001)
- <sup>71</sup> Y. Suzuki, N. Kondo and T. Ohji, "Reactive Synthesis of a Porous Calcium Zirconate/ Spinel Composite with Idiomorphic Spinel Grains," *J. Am. Ceram. Soc.*, **86** [7] 1128-31 (2003)
- <sup>72</sup> C.H. Perry, D. J. McCarthy and G. Ruprecht, "Dielectric Dispersion of Some Perovskite Zirconates," *Phys. Rev.* **13B** [5A] A1537-38 (1965)
- <sup>73</sup> M. Pollet, M. Daturi and S. Marinell, "Vibrational Spectroscopy Study of Doped- $CaZrO_3$  Ceramics," *Mat. Sci. Eng B* **104**, 169-75 (2003)
- <sup>74</sup> K.M. Rabe, "Computational Materials Science: Think Locally Act Globally," *Nature Materials* **1**, 147-148 (2002)
- <sup>75</sup> X.Y. Qiu, H.W. Liu, F. Fang, M.J. Ha, X.H. Zhou and J. M. Liu, "Thermal Stability and Dielectric Properties of Ultrathin  $CaZrO_x$  Films Prepared by Pulsed Laser Deposition," *Appl. Phys. A* **81** 1431-34 (2005)

- 
- <sup>76</sup> T. Yu, C.H. Chen, X.F. Chen, W. Zhu and R.G. Krishnan, "Fabrication and Characterization of Perovskite CaZrO<sub>3</sub> Oxide Thin Films," *Ceram. Int.* **30** 1279-82 (2004)
- <sup>77</sup> P.R. Krishnamoorthy, P. Ramaswamy and B.H. Narayana, "CaZrO<sub>3</sub> additives to Enhance Capacitance Properties in BaTiO<sub>3</sub> Ceramic Capacitors," *J. Mater. Sci: Materials in Electronics* **3** 176-80 (1992)
- <sup>78</sup> S. Zhang, S. Wang, X. Zhou, B. Li and Z. Chen, "Influence of 3d-Elements on Dielectric Properties of BaTiO<sub>3</sub> Ceramics," *J. Mater. Sci: Materials in Electronics* **16** 669-72 (2005)
- <sup>79</sup> R. Bagul, "Preparation of Dense Barium Cerate Film On a Planar Porous Support for Hydrogen Separation Membranes," M.S. Thesis, University of Florida (1997)
- <sup>80</sup> W. Engelen, A. Buekenhoudt, J. Luyten and F. De Shutter, "Humidity sensitivity of Electrochemical Hydrogen Cells Using Calcium Zirconate Ceramics," *Solid State Ionics* **96** 55-59 (1997)
- <sup>81</sup> M. P. Hills, C. Schwandt and R.V. Kumar, "Oxide Ion Conduction of Indium-Oxide-Substituted Calcium Zirconate," *J. Electrochem. Soc.*, **153** [10] H189-H194 (2006)
- <sup>82</sup> N. Kurita, N. Fukatsu, K. Ito, T. Ohashi, "Protonic Conduction Domain of Indium-Doped Calcium Zirconate," *J. Electrochem. Soc.*, **142**, (1995) 1552.
- <sup>83</sup> C. Wang, X.Xu, H. Yu, Y. Wen and K. Zhao, "A Study of the Solid Electrolyte Y<sub>2</sub>O<sub>3</sub>-Doped CaZrO<sub>3</sub>," *Solid State Ionics* **28-30**, 542-545 (1988)

- 
- <sup>84</sup> H. Iwahara, T. Esaka, H. Uchida and N. Maeda, "Proton conduction in sintered oxides and its application to steam electrolysis for hydrogen production," *Solid State Ionics* **3-4** 359 (1981)
- <sup>85</sup> H. Iwahara, T. Yajima, H. Kazeoka, T. Hibino, K. Ozaki and H. Suzuki, " Protonic Conduction in Calcium, Strontium and Barium Zirconates," *Solid State Ionics* **61** 65 (1993)
- <sup>86</sup> K.D. Kreur, "On the Development of Proton Conducting Materials for Technological Applications," *Solid State Ionics* **97** 1-15 (1997)
- <sup>87</sup> T. Schober, F. Krug and W. Shilling, "Criteria for the Application of High Temperature Proton Conductors in SOFC Applications," *Solid State Ionics* **97** 369-373 (1997)
- <sup>88</sup> W. Munch, K.D. Kreur, G. Seifert and J. Maier, "Proton Diffusion in Perovskites: Comparison between BaCeO<sub>3</sub>, BaZrO<sub>3</sub>, SrTiO<sub>3</sub> and CaTiO<sub>3</sub> using Quantum Molecular Dynamics," *Solid State Ionics* **136-137** 183-189 (2000)
- <sup>89</sup> H. Iwahara, Y. Asakura, K. Katahira and M. Tanaka, "Prospect of Hydrogen Technology Using Proton-Conducting Ceramics," *Solid State Ionics* **168** 299-310 (2004)
- <sup>90</sup> T. Norby, "Solid-State Protonic Conductors: Principles, Properties, Progress and Prospects," *Solid State Ionics* **125** 1-11 (1999)
- <sup>91</sup> T. Schober, "Applications of Oxidic High-Temperature Proton Conductors," *Solid State Ionics* **162-163** 277-81 (2003)
- <sup>92</sup> T. Yajima, K. Koide, N. Fukatsu, T. Ohashi and H. Iwahara, " A New Hydrogen Sensor for Molten Aluminum," *Sens. Actuators B* **13-14** 697 (1993)

- 
- <sup>93</sup> H. Iwahara, "Proton Conducting Ceramics and Their Applications," *Solid State Ionics* **86-88** 9-15 (1995)
- <sup>94</sup> Y. Suzuki, M. Awano, N. Kondo and T. Ohji, "Effect of In-doping on the Microstructure and CH<sub>4</sub>-Sensing Ability of CaZrO<sub>3</sub>/MgO Composites," *J. Eu. Ceram. Soc.*, **22** 1177-82 (2002)
- <sup>95</sup> H. Matsumoto, H. Hayashi, T. Shimura, H. Iwahara and T. Yogo, "Electrochemical Hydrogen Isotope Sensing Via the Proton Conductor CaZr<sub>0.9</sub>In<sub>0.1</sub>O<sub>3- $\alpha$</sub> ," *Solid State Ionics* **161** 93-103 (2003)
- <sup>96</sup> K.D. Kreur, "On the Complexity of Proton Conduction Phenomena," *Solid State Ionics* **136-137** 149-60 (2000)
- <sup>97</sup> A.S. Nowick, A.V. Vaysleyb, "Isotope Effects and Proton Hopping in High-Temperature Protonic Conductors," *Solid State Ionics* **97** 17-26 (1997)
- <sup>98</sup> M.S. Islam, R.A. Davies and J.D. Gale, "Hop, Skip or Jump? Proton Transport in the CaZrO<sub>3</sub> Oxide," *Chem. Commun.*, 661-62 (2001)
- <sup>99</sup> R.A. Davies, M.S. Islam and J.D. Gale, "Dopant and Proton Incorporation in Perovskite-Type Zirconates," *Solid State Ionics* **126** 323-335 (1999)
- <sup>100</sup> M.S. Islam, P.S. Slater, J.R. Tolchard and T. Dinges, "Doping and Defect Association in AZrO<sub>3</sub> (A= Ca, Ba) and LaMO<sub>3</sub> (M=Sc, Ga) Perovskite type Ionic Conductors," *Dalton Trans.* 3061-3066 (2004)
- <sup>101</sup> T. Yajima, H. Kazeoka, T. Yogo and H. Iwahara, "Proton Conduction in Sintered Oxides Based on CaZrO<sub>3</sub>," *Solid State Ionics* **47** 271-75 (1991)

- 
- <sup>102</sup> R. Hempelmann, M. Soetratmo, O. Hartmann and R. Wappling, "Muon Diffusion and Trapping in Proton Conducting Oxides," *Solid State Ionics* **107** 269-280 (1998)
- <sup>103</sup> K.S. Knight, "Structural Phase Transitions, Oxygen Vacancy Ordering and Protonation in Doped BaCeO<sub>3</sub>: Results from Time-of-Flight Neutron Powder Diffraction Investigations," *Solid State Ionics* **145** 275-294 (2001)
- <sup>104</sup> K.S. Knight, "Powder Neutron Diffraction Studies of BaCe<sub>0.9</sub>Y<sub>0.1</sub>O<sub>2.95</sub> and BaCeO<sub>3</sub> at 4.2 K: A Possible Structural Site for the Proton," *Solid State Ionics* **127** 43-48 (2000)
- <sup>105</sup> T. Omata, M. Takagi, S. Matsuo, "O-H Stretching Vibrations of Proton Conducting Alkaline-Earth Zirconates," *Solid State Ionics* **168** 99-109 (2004)
- <sup>106</sup> T. Higuchi, S. Yamaguchi, K. Kobayashi, S. Shin and T. Tsukamoto, "Electronic structures in the bulk and surface states of protonic conductor CaZrO<sub>3</sub> by soft-X-ray spectroscopy," *Solid State Ionics* **162–163** 121–125 (2003)
- <sup>107</sup> T. Hibino, K. Mizutani, T. Yajima and H. Iwahara, "Evaluation of Proton Conductivity in SrCeO<sub>3</sub>, BaCeO<sub>3</sub>, CaZrO<sub>3</sub> and SrZrO<sub>3</sub> by Temperature Programmed Desorption Method," *Solid State Ionics* **57** 303-306 (1992)
- <sup>108</sup> M. R. Nadler, E.S. Fitzsimmons, "Preparation and Properties of Calcium Zirconate," *J. Amer.Ceram.Soc.* **38** 214-217 (1955)
- <sup>109</sup> R. Angers, R. Tremblay and A.C.D. Chaklader, "Formation of CaZrO<sub>3</sub> by Solid- State Reaction Between CaO and ZrO<sub>2</sub>," *J.Amer.Ceram.Soc.*, **55** 425-426 (1972)
- <sup>110</sup> R. Angers, R. Tremblay and A.C.D. Chaklader, "Effect of Pressure on formation of CaZrO<sub>3</sub> by Solid- State Reaction Between CaO and ZrO<sub>2</sub>," *J.Amer.Ceram.Soc.*, **57** 231-232 (1974)

- 
- <sup>111</sup> T. Yu, W.G. Zhu, C.H. Chen, X.F. Chen and R. Gopal Krishnan, "Preparation and Characterization of Sol-Gel Derived CaZrO<sub>3</sub> Dielectric Thin Films for High-k Applications," *Physica B* 440-45 (2004)
- <sup>112</sup> J. Xu, A.P. Wilkinson and S. Pattanaik, "Solution Processing of Calcium Zirconium Titanates Ca(Zr<sub>x</sub>Ti<sub>1-x</sub>)O<sub>3</sub>: An X-ray Absorption Spectroscopy and Powder Diffraction Study," *Chem. Mater.* **12** 3321-30 (2000)
- <sup>113</sup> M. Pechini, US Patent 3330697 July 11 1967
- <sup>114</sup> W. Zheng, W. Pang, G. Meng, "Hydrothermal Synthesis of SrZrO<sub>3-x</sub> (M=Al, Ga, In, x < 0.20) Series Oxides", *Solid State Ionics* **108** 37-41 (1998)
- <sup>115</sup> G. Dell'Agli and G. Mascolo, "Low Temperature Hydrothermal Synthesis of ZrO<sub>2</sub>-CaO Solid Solutions", *J. Mat. Sci.* **35** 661-65 (2000)
- <sup>116</sup> A. Bhargava, T. Yamashita and I. D. R. Mackinnon, "Manufacture of specific BSCCO powder compositions by co-precipitation," *Physica C*, **247** 385 (1995)
- <sup>117</sup> Chuanbin Mao, Lian Zhou, Fuzai Cuia and Hengde Lia, "Optimization of a new modified wet-chemistry process for the synthesis of BPSCCO superconductor precursor powders with specific stoichiometry" *J. Mater. Chem.*, **7** [8] 1451-1456 (1997)
- <sup>118</sup> Naofumi Uekawa, Michio Endo, Kazuyuki Kakegawa and Yoshinori Sasaki, "Homogenous precipitation of Cr<sup>3+</sup>-M<sup>2+</sup> (M=Ni, Zn, Co, Cu) Oxalate by Oxidation of the Polyethylene Glycol-Cation Complex," *Phys. Chem. Chem. Phys.*, **2** 5485-5490 (2000)
- <sup>119</sup> V.B. Reddy and P.N. Mehrotra, "Preparation, Characterization and Thermal Decomposition of Barium Zirconyl Oxalate," *Thermochim. Acta* **31** 31-37 (1979)

- 
- <sup>120</sup> M. Toprak, Y. Zhang and M. Muhammed, "Chemical Alloying and Characterization of Nanocrystalline Bismuth Telluride," *Materials Letters* **57** 3976-82 (2003)
- <sup>121</sup> C. Drouet, P. Alphonse and A. Rousset, "Synthesis And Characterization Of Non-Stoichiometric Nickel-Copper Manganites" *Solid State Ionics* **123** 25-37 (1999)
- <sup>122</sup> Y. Wei, L. Guangqiang and S. Zhitong, "Coprecipitating Synthesis and impedance study of CaZrInO<sub>x</sub>." *J. Mat. Sci. Lett.* **17** 241-43 (1998)
- <sup>123</sup> J. Le, N. van Rij, R.C. van Landschoot and J.Schoonman, "A Wet-Chemical Method for the Synthesis of In-doped CaZrO<sub>3</sub> Ceramic Powders", *J. Eur. Ceram. Soc.* **19** 2589-2591 (1999)
- <sup>124</sup> N. Van Rij, L. Winnubst, J. Le and J. Schoonman, "Analysis of the preparation of In-doped CaZrO<sub>3</sub> by the peroxo-oxalate complexation method" *J. Mater. Chem.* **10** 2515-21 (2000)
- <sup>125</sup> M.J. Saavedra, C. Parada, M.O. Figueiredo and A. Correa Dos Santos "Ca-Zr-O system: synthesis and characterization of compounds using several routes of preparation", *Solid State Ionics* **63-65** 213-217 (1993)
- <sup>126</sup> T. Gangadevi, K. Muraleedaran and M.P. Kannan, "A Comparitive Study of the Thermal Decomposition Kinetics of Zirconyl Oxalates of Calcium and Strontium", *Thermochim. Acta*, **146** 225-232 (1989)
- <sup>127</sup> V.B. Mehrotra and P.N. Reddy, "IR and Thermal Studies of Calcium Zirconyl Oxalate", *J. Inorg. Nucl. Chem.* **43** 1078-1079 (1981)



- 
- <sup>128</sup> B. Chapelet-Arab, G. Nowogrocki, F. Abraham and S. Grandjean, "New alkaline earth-zirconium oxalates  $M_2Zr(C_2O_4)_4 \cdot nH_2O$  (M = Ba, Sr, Ca) synthesis, crystal structure and thermal behavior" *J. Solid State Chem.* **177** [11] 4269-4281 (2004),.
- <sup>129</sup> N. Audebrand, E. Jeanneau, T. Bataille, S. Raite and D. Louer, "A Family of Microporous Mixed Oxalates with Isotypic-Framework Structures based on Eight-Coordinate Metals," *Solid State Sciences* **6** 579-591 (2004)
- <sup>130</sup> C. F. Baes Jr. and R.E. Mesmer in "The Hydrolysis of Cations" (John Wiley and Sons, 1976) p.152.
- <sup>131</sup> E. Curtis and C. Degueldre, "Solubility and Hydrolysis of Zr Oxides: a Review and Supplemental Data," *Radiochim. Acta* **90** 801-804 (2002)
- <sup>132</sup> S.V. Elinson and K.I. Petrov in "Analytical Chemistry of Zirconium and Hafnium," (Daniel Davey and Co, 1965) p. 7
- <sup>133</sup> T. Sato, "The Thermal Decomposition of Zirconium Oxyhydroxide," *J. Therm. Anal. Calorimetry* **69** 256-265 (2002)
- <sup>134</sup> W.O.S. Doherty, "Effect of Calcium and Magnesium Ions on Calcium Oxalate Formation in Sugar Solutions", *Ind. Eng. Chem. Res.*, **45** 642-647 (2006)
- <sup>135</sup> T. Moeller, "Contributions to the Chemistry of Indium III. An Electrometric Study of the Precipitation of Hydrous Indium Hydroxide," *J. Am. Chem. Soc.* **63** 2625-2628 (1941)
- <sup>136</sup> N. Uekawa, M. Endo, K. Kakegawa and Y. Sasaki, "Homogenous precipitation of  $Cr^{3+}$ - $M^{2+}$  (M=Ni, Zn, Co, Cu) oxalate by oxidation of the polyethylene glycol-cation complex," *Phys. Chem. Chem. Phys.* **2** 5485-5490 (2000)

- 
- <sup>137</sup> N.M. Kirby, A. Van Riesen, C.E. Buckley and V.W. Wittorff, "Oxalate-precursor processing for high quality BaZrO<sub>3</sub>," *J. Mater. Sci.* **40** 97-106 (2005)
- <sup>138</sup> A. Cavalheiro, M.A. Zaghete And J. Varela, "Influence Of Ammonium Oxalate In The Formation Of The Columbite Precursor Obtained By Pechini's Method," *Cerâmica* **45** 56 (1999)
- <sup>139</sup> E. K. Girija, S.C. Latha, S. N. Kalkura, C. Subramaniam And P. Ramasamy, "Crystallization and Microhardness of Calcium Oxalate Monohydrate," *Materials Chemistry and Physics* **52** 253-257 (1998)
- <sup>140</sup> J-M Ouyang and S-P Deng, "Controlled and Uncontrolled Crystallization of Calcium Oxalate Monohydrate in the Presence of Citric Acid," *Dalton Transactions* 2846-2851 (2003)
- <sup>141</sup> H. El-Shall, J-H Jeon, E.A. Abdel-Aal, S. Khan, L. Gower and Y. Rabinowich, "A Study of Primary Nucleation of Calcium Oxalate Monohydrate I – Effect of Supersaturation," *Crystal Research Technology* **39** [3] 214-221 (2004)
- <sup>142</sup> L. Maurice-Estépa, P. Levillain, B. Lacour and M. Daudon, "Advantage of Zero-Crossing-Point First-Derivative Spectrophotometry for the Quantification of Calcium Oxalate Crystalline Phases by Infrared Spectrophotometry," *Clinica Chimica Acta* **298** 1-11 (2000)
- <sup>143</sup> O. Vasylykiv, Y. Sakka, "Synthesis and Colloidal Processing of Zirconia Nanopowder," *J. Am. Ceram. Soc.*, **84** [11] 2489-94 (2001)
- <sup>144</sup> K. Kobayashi, Y. Yamaguchi, Y. Iguchi, "Electrical Transport Properties of Calcium Zirconate at High Temperatures", *Solid State Ionics* **108** 355-62 (1998)

- 
- <sup>145</sup> Q. Liu, L. Gao, D.S. Yan, H. Mandal and Thompson D.P., “The Effect of Heat-Treatment on the Performance of sub-micron SiC<sub>p</sub>-Reinforced Sialon Composites – I. Preparation of Agglomerate-Free Starting Powders,” *J. Eu. Ceram. Soc.*, **17** 581-585 (1997)
- <sup>146</sup> O.I. Ece, A. Alemdar, N. Gungor And S. Hayashi, “Influences of Nonionic Poly(ethylene glycol) Polymer PEG on Electrokinetic and Rheological Properties of Bentonite Suspensions,” *J. App. Polym. Sci.* **86** (2002) 341.
- <sup>147</sup> S.A. Uhland, M.J. Cima and E.M. Sachs, “Additive-Enhanced Redispersion of Ceramic Aggregates,” *J. Am. Ceram. Soc.* **86** (9) 1487-1492 (2003)
- <sup>148</sup> N. Uekawa, H. Ichikawa, A. Itsuki, S. Ishii, K. Kakegawa and Y. Sasaki, “Preparation of Oxalate by Precipitation Method with Polyethylene Glycol and Formation Process of the Precipitate,” *J. Chem. Soc. Jap.*, 3 (2000) 187.
- <sup>149</sup> M.S. Kaliszewski and A.H. Heuer, “Alcohol Interaction with Zirconia Powders,” *J. Am. Ceram. Soc.*, **73** [6] 1504-1509 (1990)
- <sup>150</sup> J. Fleig, “The Grain Boundary Impedance of Random Microstructures: Numerical Simulations and Implications for the Analysis of Experimental Data,” *Solid State Ionics* **150** 181-193 (2002)
- <sup>151</sup> J. Fleig, J. Jamnik and J. Maier, “On the Validity and Limits of the Brick Layer Model in Impedance Spectroscopy”, *J. Electrochem. Soc.*, **145** 2081 (1998)
- <sup>152</sup> C.C. Wang, S.A. Akbar, W. Chen and J.R. Schorr, “High-temperature Thermistors Based on Yttria and Calcium Zirconate,” *Sens. Actu. A* **58** 237-243 (1997)

- 
- <sup>153</sup> G. Rog, M. Dudek, A. Kosłowska-Rog and M. Bucko, "Calcium Zirconate: Preparation, Properties and Application to the Solid Oxide Galvanic Cells," *Electrochimica Acta* **47** 4325-4329 (2002)
- <sup>154</sup> M. Dudek, M.M. Bucko, "Electrical Properties of Stoichiometric and Non-stoichiometric Calcium Zirconate," *Solid State Ionics*, **157** 183-187 (2003)
- <sup>155</sup> A.R. West "Crystalline Solid Electrolytes I: General Considerations and Major Materials", in *Solid State Electrochemistry*, ed. P.G. Bruce page 18, Cambridge University Press, 1995
- <sup>156</sup> S.C. Hwang, G.M. Choi, "The Effect of Cation Nonstoichiometry on the Electrical Conductivity of CaZrO<sub>3</sub>," *J. Eur. Ceram. Soc.*, **25** 2609-2612 (2005)
- <sup>157</sup> D. Janke, "Oxygen Probes Based on Calcia-Doped Hafnia or Calcium Zirconate for Use in Metallic Melts," *Metall. Trans. B* **13B** 227-235 (1982)
- <sup>158</sup> A. Pretis, V. Longo, F. Ricciardiello and O. Sbraizero, "Considerations on the Electrical Properties of Ceramics based on Perovskite-type Compounds," *Silicates Industriels* **139** 7-8 (1984)
- <sup>159</sup> C.C. Wang, S.A. Akbar, W. Chen and V.D. Patton, "Review: Electrical Properties of High-Temperature Oxides, Borides, Carbides and Nitrides," *J. Mat. Sci.*, **30** 1627-1641 (1995)
- <sup>160</sup> C.C. Wang, W.H. Chen, S.A. Akbar and M.A. Alim, "High-temperature A.C. Electrical Behavior of Polycrystalline Calcium Zirconate," *J. Mat. Sci.*, **32** 2305-2312 (1997)
- <sup>161</sup> R.D. Shannon, "Revised Effective Ionic Radii and Systematic Studies of Interatomic Distances in Halides and Chalcogenides," *Acta Cryst. A* **32** 751- 767 (1976)

- 
- <sup>162</sup> N. Kurita, N. Fukatsu, H. Ito and T. Ohashi, "Protonic Conduction Domain of Indium-Doped Calcium Zirconate," *J. Electrochem. Soc.*, **142** [5] 1552-1559 (1995)
- <sup>163</sup> M.S. Islam, R.A. Davies and J.D. Gale, "Proton Migration and Defect Interactions in the CaZrO<sub>3</sub> Orthorhombic Perovskite: A Quantum Mechanical Study," *Chem. Mater.* **13** 2049-2055 (2001)
- <sup>164</sup> *Impedance Spectroscopy: Emphasizing Solid Materials and Systems*, Ed. Ross Macdonald, Wiley-Interscience, London (1987)
- <sup>165</sup> S. Yamaguchi, K. Kobayashi, T. Higuchi, S. Shin and Y. Iguchi, "Electronic Transport Properties and Electronic Structure of InO<sub>1.5</sub>-doped CaZrO<sub>3</sub>," *Solid State Ionics* **136-137** 305-311 (2000)
- <sup>166</sup> G. Rupprecht and R.O. Bell, "Dielectric Constant in Paraelectric Perovskites," *Phy. Rev.* **135** [3A] A748-A752 (1964)
- <sup>167</sup> S. Zafar, R.E. Jones, P. Chu, B. White, B. Jiang, D. Taylor, P. Zurcher and S. Gillespie, "Investigation of Bulk and Interfacial Properties of Ba<sub>0.5</sub>Sr<sub>0.5</sub>TiO<sub>3</sub> Thin Film Capacitors," *App. Phy. Lett.* **72** [22] 2820-2822 (1998)
- <sup>168</sup> S. Serena, M.A. Sainz and A. Caballero, "Experimental Determination and Thermodynamic Calculation of the Zirconia-Calcia-Magnesia System at 1600°, 1700°, and 1750°C," *J. Amer. Ceram. Soc.* **87** [12] 2268-2274 (2004)
- <sup>169</sup> S. Serena, A. Caballero, M. Sainz, C. Antonia, P. Convert, J. Campo and X. Turrillas, "Neutron Thermodiffraction Study of Calcium Zirconate/Magnesium Oxide Formation in the ZrO<sub>2</sub>-CaO-MgO system," *J. Amer. Ceram. Soc.* **87** [9] 1706-1713 (2004)

- 
- <sup>170</sup> J.R. McDonald, "Frequency response of unified dielectric and conductive systems involving an exponential distribution of activation energies," *J. Appl. Phys.* **58** 1955 (1985)
- <sup>171</sup> V. Krishnan and J.W. Fergus, "Characterization of indium-doped calcium zirconate at low oxygen partial pressures using impedance spectroscopy," *Proceedings - Electrochemical Society, 2002-26(Solid-State Ionic Devices III)* 471-477 (2003)
- <sup>172</sup> M.W. Chase, NIST-JANAF Thermochemical Tables, 4<sup>th</sup> Edition, Journal of Physical and Chemical Reference Data, Monograph No. 9 (1998)
- <sup>173</sup> R. W. Curtis and P. Chiotti, "Thermodynamic Properties of Calcium Hydride," *J. Phy. Chem.* **67** 1061-1065 (1963)
- <sup>174</sup> A.K.M.S. Chowdhury, S.A. Akbar, S. Kapileshwar and J.R. Schorr, "A Rugged Oxygen Gas Sensor with Solid Reference for High Temperature Applications," *J. Electrochem. Soc.*, **14B** [2] G91-G94 (2001)
- <sup>175</sup> K.S. Knight, Personal Communication